

Properties of Ir₄ Clusters in the Gas Phase and on Oxide Substrates

THÈSE N° 4502 (2009)

PRÉSENTÉE LE 14 SEPTEMBRE 2009

À LA FACULTE SCIENCES DE BASE

CHAIRE DE PHYSIQUE NUMÉRIQUE DE LA MATIÈRE CONDENSÉE

PROGRAMME DOCTORAL EN PHYSIQUE

ÉCOLE POLYTECHNIQUE FÉDÉRALE DE LAUSANNE

POUR L'OBTENTION DU GRADE DE DOCTEUR ÈS SCIENCES

PAR

Vladan STEVANOVIC

acceptée sur proposition du jury:

Prof. G. Meylan, président du jury
Prof. A. Baldereschi, directeur de thèse
Prof. W. Andreoni, rapporteur
Prof. A. De Vita, rapporteur
Dr Z. Sljivancanin, rapporteur



ÉCOLE POLYTECHNIQUE
FÉDÉRALE DE LAUSANNE

Suisse
2009

Résumé

Les résultats d'une étude théorique des propriétés de cluster d'Ir₄ dans la phase gazeuse et sur des surfaces d'oxyde sont présentés. Ce travail est basé sur la méthode de la théorie de la fonctionnelle de la densité (DFT) dans l'approximation du gradient généralisé (GGA) et des pseudo-potentiels "ultrasoft".

Les propriétés d'une petite particule telle que le cluster d'Ir₄ sont entièrement déterminés par sa géométrie. Le fait déjà connu que la forme la plus stable de l'Ir₄ dans la phase gazeuse est la structure carrée, qui est significativement plus stable que les structures en "papillon" (butterfly) ou en tétraèdre, est confirmé. Ce résultat est en contradiction avec des expériences qui indiquent que l'Ir₄ déposé sur l'oxyde adopte une configuration en tétraèdre. Il est montré, dans cette thèse, que l'environnement chimique exerce une forte influence sur la stabilité relative des clusters d'Ir₄.

Sur la surfaces MgO(110) l'isomère carré demeure la structure d'Ir₄ la plus stable, bien séparée en terme d'énergie des deux autres. De plus, le tétraèdre est fortement déformé de part l'interaction avec l'oxygène de la surface. La présence de défauts ponctuels (neutres et lacunes chargées O) affecte l'ordre énergétique, rendant tétraèdre et carré très proche en énergie, les déformations structurelles du tétraèdre étant même plus importantes, prédictions en désaccord avec les expériences.

Sur la surface TiO₂(110) les structures en tétraèdre et carré deviennent dégénérées et celle en papillon est l'isomère le moins stable. De plus, les déformations structurelles sont très petites, en bon accord avec les expériences. Il est montré que la surface de TiO₂ influence la stabilité relative des trois isomères par un champ électrostatique particulièrement fort.

Les interactions de l'Ir₄ avec les atomes H, C and O ainsi qu'avec des molécules de CO ont été étudiées. L'adsorption d'un unique atome C influence fortement la stabilité relative des trois isomères. Avec l'adsorption de C, la structure papillon devient le plus stable isomère de la phase gazeuse alors que sur les deux surfaces l'Ir₄ tétraèdre est la structure la plus probable. L'adsorption d'un seul atome C ou O ne produit pas le même effet.

L'interaction avec les molécules de CO est aussi important étant donné la procédure expérimentale pour produire les cluster d'Ir₄ déposés. Il est montré que sur la MgO(100) la dissociation du CO est autant probable que le processus concurrent de désorption du CO, justifiant la présence d'atomes de carbone sur les clusters d'Ir₄ et rapprochant ainsi les prédictions théoriques des données expérimentales.

Mots-clés: clusters, iridium, théorie de la fonctionnelle de la densité, surfaces, adsorption

Abstract

Results of a theoretical study on the properties of Ir_4 clusters in the gas-phase and on oxide surfaces are presented. The work is based on density functional theory (DFT) within the generalized gradient approximation (GGA) and ultrasoft pseudopotentials.

Properties of a small particle such as Ir_4 cluster are entirely determined by its geometry. The already known result that the most stable form of Ir_4 in the gas-phase is the square structure which is significantly more stable than the butterfly and tetrahedron is confirmed. This result is in contradiction with experiments which indicate that the oxide supported Ir_4 adopts a tetrahedral configuration. It is shown in this thesis that the chemical environment has a strong influence on the relative stability of Ir_4 clusters.

On $\text{MgO}(100)$ surface, the square isomer remains the most stable Ir_4 structure, well separated in energy from the other two. Moreover, the tetrahedron is heavily distorted by the interaction with the surface oxygen. Presence of point defects (neutral and charged O vacancies) affects the energy ordering making tetrahedron and square very close in energy, but the structural distortion of the tetrahedron is even bigger and the predicted data do not correspond to experiments.

On $\text{TiO}_2(110)$ the tetrahedron and square structures become degenerate and the butterfly becomes the least stable isomer. Moreover, structural distortions are very small, in agreement with experimental data. It is shown that the TiO_2 surface influences the relative stability of the three isomers through a particularly strong electrostatic field.

Interactions of Ir_4 with H, C and O atoms as well as with CO molecules have been studied. Adsorption of a single C atom strongly influences the relative stability of the three isomers. Upon C adsorption, the butterfly becomes the most stable gas-phase isomer while on both surfaces the tetrahedron is the most probable structure. Adsorption of a single H or O atom does not produce the same effect.

The interaction with CO molecules is also important given the experimental procedure used for producing supported Ir_4 clusters. It is shown that on $\text{MgO}(100)$, CO dissociation is as probable as the competing process CO desorption justifying the presence of carbon adatoms on Ir_4 clusters which brings theoretical predictions in better agreement with experimental data.

Keywords: clusters, iridium, density functional theory, surfaces, adsorption

Contents

1	Introduction	13
2	Density Functional Theory and Methods	17
2.1	Density Functional Theory	17
2.1.1	The LDA and GGA Approximations and Beyond	18
2.2	Methods	19
2.2.1	Pseudopotentials	19
2.2.2	The Supercell Approximation and Plane Wave Expansions	21
2.2.3	Dipole Correction Method	23
2.2.4	Ionic Forces and Vibrational Analysis	24
2.2.5	Transition-state Theory and The Nudged Elastic Band (NEB) Method	26
3	Gas-phase Iridium Clusters	29
3.1	Iridium Atom	29
3.2	Ir Dimer	30
3.3	Ir_n ($n = 3, \dots, 8$) Clusters	33
3.4	The Case of Ir_4	38
3.4.1	Stability of X_4 isomers ($\text{X}=\text{H}, \text{Au}, \text{Pt}, \text{Ir}, \text{Rh}, \text{Co}, \text{Ru}$)	45
4	Influence of Adsorbates on the Stability of Ir_4 clusters	51
4.1	Adsorption of H, C or O atoms	51
4.2	Adsorption of a single CO molecule	55
4.3	CO Dissociation on Ir_4	59
5	Ir_4 Clusters Supported by $\text{MgO}(100)$ and $\text{TiO}_2(110)$ Substrates	61
5.1	Bulk Oxides and Their Surfaces	61
5.1.1	Bulk MgO and the $\text{MgO}(100)$ Surface	61
5.1.2	Bulk TiO_2 and the $\text{TiO}_2(110)$ Surface	63
5.2	Adsorption of Atomic Iridium on $\text{MgO}(100)$	65
5.3	Adsorption of Ir_4 Clusters on $\text{MgO}(100)$	68
5.4	Diffusion of Ir_4 Clusters on $\text{MgO}(100)$ Surface	73
5.5	Adsorption of Ir_4 Clusters on $\text{MgO}(100)$ Surface With a Neutral and Positively Charged Oxygen Vacancy	75
5.6	Adsorption of Ir_4 on $\text{TiO}_2(110)$	80

6	Influence of Adsorbates on the Relative Stability of Oxide Supported Ir₄ Clusters	89
6.1	Interaction of MgO(100) Supported Ir ₄ Clusters With H, C or O atoms	89
6.2	Interaction of MgO(100) Supported Ir ₄ Clusters With CO Molecules	94
6.2.1	CO Dissociation	98
6.2.2	Multiple CO adsorption	99
6.3	Interaction of TiO ₂ (100) Supported Ir ₄ Clusters With a C Atom or a Single CO molecule	103
6.4	Influence of the Environment on the Properties of Ir ₄ Clusters	107
7	Conclusions	109
A	Extended X-Ray Absorption Fine Structure (EXAFS) Spectroscopy	113
B	Character Tables of D_{∞h}, C_{2v}, D_{4h} and T_d Point Groups	115
	Bibliography	120

List of Figures

2.1	Dipole correction method	24
3.1	Electronic spectrum of Ir atom	30
3.2	Spectrum of Ir ₂	32
3.3	Properties of the gas-phase Ir _n ($n \leq 8$) clusters	37
3.4	Properties of the gas-phase Ir ₄ clusters	39
3.5	Electronic spectra of the gas-phase Ir ₄	41
3.6	Modification of the Ir pseudopotential	43
3.7	Dependence of the results for Ir ₄ on the pseudopotential used in calculations	44
3.8	Electronic spectra of the H ₄ clusters	46
3.9	Transition metals whose tetramers are being investigated	47
3.10	Projected DOS of the tetramers from the iridium group (Co, Rh and Ir)	48
4.1	Configurations of the gas-phase Ir ₄ clusters interacting with atomic H, C and O	52
4.2	Ir ₄ -C interaction mechanism	54
4.3	Relative position of the KS levels of H, C, O and Ir ₄	55
4.4	Configurations of the gas-phase Ir ₄ clusters interacting with a single CO molecule	56
4.5	Relative position of the KS levels of the CO molecule and Ir ₄	57
4.6	Projected DOS on the CO states when interacting with the gas-phase Ir ₄	58
4.7	The CO dissociation on the gas-phase Ir ₄	59
5.1	Clean MgO(100) surface	62
5.2	Clean TiO ₂ (110) surface	64
5.3	Adsorption of atomic Ir on MgO(100) surface	67
5.4	Ir-MgO(100) interaction mechanism	68
5.5	Adsorption Ir ₄ on defect-free MgO(100) surface	69
5.6	Relaxations of defect-free MgO(100) upon Ir ₄ adsorption	71
5.7	Ir ₄ -MgO(100) interaction mechanism	72
5.8	Ir ₄ diffusion on defect-free MgO(100)	74
5.9	Adsorption geometries for Ir ₄ on MgO(100) with the oxygen vacancies	76
5.10	Relaxations of MgO(100) with the oxygen vacancies upon Ir ₄ adsorption	78
5.11	Ir ₄ -F(F ⁺) centers interaction mechanism	79
5.12	Adsorption configurations for Ir ₄ on TiO ₂ (110) surface	81
5.13	Ir ₄ -TiO ₂ (110) interaction mechanism	83
5.14	Induced charge for adsorption of Ir ₄ on TiO ₂ (110) surface	84
5.15	Dependence of the relative stability of Ir ₄ clusters on electric field	85
5.16	Electrostatic potential of TiO ₂ (110) surface	86

6.1	Configurations of the MgO supported Ir ₄ clusters interacting with atomic H, C and O	90
6.2	Ir ₄ /MgO(100)–C interaction mechanism	92
6.3	The C adatom vibrations of Ir ₄ C/MgO(100) in T configuration	93
6.4	Configurations of the MgO supported Ir ₄ clusters interacting with one and two CO molecules	95
6.5	The CO vibrations of Ir ₄ CO/MgO(100) in T configuration	97
6.6	The CO dissociation on Ir ₄ /MgO(100) in T configuration	99
6.7	Configurations of Ir ₄ /MgO(100) in T geometry interacting three to five CO molecules	100
6.8	Adsorption properties of up to five CO molecules on Ir ₄ /MgO(100) in T configuration	102
6.9	Configurations of Ir ₄ /TiO ₂ (100) interacting a C adatom and a single CO molecule	104
6.10	Properties of Ir ₄ clusters on the environment	107
A.1	Basics of EXAFS	113

List of Tables

3.1	Properties of the gas-phase Ir_n ($n \leq 8$) clusters	34
3.2	Properties of the X_4 ($\text{X} = \text{H}, \text{Au}, \text{Pt}, \text{Ir}, \text{Pd}, \text{Rh}, \text{Ru}$ and Co) clusters	47
4.1	Properties of the gas-phase Ir_4 clusters interacting with atomic H , C and O .	52
4.2	Properties of the gas-phase Ir_4 clusters interacting with a single CO molecule	56
5.1	Results of tests performed on $\text{Ir}/\text{MgO}(100)$ system	66
5.2	Properties of Ir_4 clusters adsorbed on defect-free $\text{MgO}(100)$ surface	70
5.3	Deformation energies for the Ir_4 adsorption on defect-free $\text{MgO}(100)$	71
5.4	Properties of Ir_4 adsorbed on $\text{MgO}(100)$ with the oxygen vacancies	77
5.5	Deformation energies for adsorption of Ir_4 on $\text{MgO}(100)$ with the oxygen vacancies	78
5.6	Properties of Ir_4 adsorbed on $\text{TiO}_2(110)$ surface	82
5.7	Deformation energies for adsorption of Ir_4 on $\text{TiO}_2(110)$ surface	82
6.1	Properties of the MgO supported Ir_4 clusters interacting with atomic H , C and O	91
6.2	Properties of the MgO supported Ir_4 clusters interacting with a single CO molecule	96
6.3	Properties of $\text{Ir}_4/\text{MgO}(100)$ clusters interacting two to five CO molecules . .	101
6.4	Properties of $\text{Ir}_4/\text{TiO}_2(100)$ interacting a C adatom and a single CO molecule	105

Chapter 1

Introduction

In atomic and molecular physics and in chemistry the term "cluster" refers to a group of bound atoms ranging from a few atoms up to several hundred or even thousand atoms. The term was introduced in early 1960s to describe compounds containing metal-metal bonds [1]. The definition has evolved and nowadays "cluster" refers to any group of atoms that contains element-element bonds.

Clusters can be both mononuclear or polynuclear. They are intermediate between atomic and bulk systems and as such, they are the true representatives of the "nanoworld", reduced both in size and dimensionality. Quantum confinement effects together with the lack of symmetry constraints make them extremely interesting since their properties may be completely different from the properties of their atomic and bulk counterparts (*i.e.* enhanced catalytic activity, magnetism in otherwise nonmagnetic systems, ...). It has been found that the properties of clusters strongly depend on their size [2]. They may display abrupt changes with the cluster size, especially for small species (up to approximately several tens of atoms) while for bigger clusters the properties typically converge to those of the bulk.

These effects make clusters promising candidates for several technological applications such as catalysis, sensors, magnetic storage devices, solar cells, controlled drug delivery, etc. Potentially, clusters could also be used as the building blocks of composite materials whose properties can be tuned through selection of their size and composition [3].

As catalysts clusters are used both in solutions (homogeneous catalysis) or dispersed over an "inert" oxide support (for heterogeneous catalysis). The enhanced catalytic activity of clusters is usually associated with the large fraction of undercoordinated atoms due to their high surface to volume ratio [4]. For applications in catalysis an important family of elements used for cluster fabrication is comprised of the group 8–10 transition metals or the "platinum group" (Ru, Rh, Pd, Os, Ir and Pt).

Iridium is one of the "platinum group" transition metals with atomic number $Z = 77$, laying below rhodium and in-between osmium and platinum in the periodic table. It is very hard and brittle, and due to its very high melting temperature (2739K [5]) it is very hard to machine, form, or work. Iridium is the most corrosion resistant metal known, and was used in making the standard metre bar of Paris, which is a 90% platinum–10% iridium alloy¹. However, its powder, if fine enough, is much more reactive and can even be flammable. Iridium is one of the least abundant elements in the Earth's crust, but on the other hand, it is one of the cheapest precious metals, third after silver and palladium and three to four

¹This metre bar has since been replaced as a fundamental unit of length.

times less expensive than platinum and rhodium [6].

Iridium, as other group 8–10 transition metals, is also used as a catalyst. The surfaces of iridium have been shown to be a very effective catalysts for the C–H bond activation in alkanes and alkenes. Mechanisms of the dissociative chemisorption of both methane [7] and ethene [8] on iridium surfaces have been studied experimentally. Several reactions of industrial importance such as conversion of saturated hydrocarbons to aromatic compounds, steam reforming of methane and the conversion of methane to higher hydrocarbons or methanol involve the C–H bond activation. Furthermore, iridium complexes, mostly in the form of carbonyls, are also widely employed as catalysts in the chemical industry. The carbonyls are extensively used in homogeneous catalysis as promoters in the Cativa process for carbonylation of methanol to produce acetic acid [9]. Almost 60 % of the production of acetic acid is done through the carbonylation of methanol and the Ir based catalysts offer significant improvements over conventional rhodium technology.

However, the need for more efficient heterogeneous catalysts, stimulated interest in studying small iridium clusters deposited on oxide surfaces. Several techniques for preparation of the supported species, such as size and energy-selected deposition of Ir_n^+ ($n = 1, 2, 5, 10, 15$) clusters [10] or the vapor-deposition of Ir nanoparticles [11] have been used. Moreover, a method for producing nearly monodispersed Ir_4 particles over common oxide substrates, such as MgO, Al_2O_3 , or TiO_2 was developed in the last 15 years [12]. The production procedure of supported Ir_4 clusters involves $\text{Ir}_4(\text{CO})_{12}$ carbonyls that are used as a source of iridium. They are deposited on an oxide surface, and decarbonylated in the flowing He at elevated temperatures. A combination of infrared (IR) and extended X-ray absorption fine structure (EXAFS) spectroscopies is then used for the characterization of the as-prepared species and for the study of their catalytic properties. A tenfold increase in the catalytic activity has been observed by replacing the MgO substrate with a $\gamma\text{-Al}_2\text{O}_3$ revealing a strong influence of the substrate on the properties of the adsorbed species. The EXAFS results also showed that upon full decarbonylation the Ir–Ir coordination number remains three as in the precursor, suggesting that the carbonyl tetrahedral Ir_4 frame remains intact. This is an important result since the properties of such a small system like Ir_4 depend strongly also on the atomic configuration².

On the other hand, only a few theoretical studies on Ir clusters exist in the literature [64, 66, 71, 73] mostly treating isolated (gas-phase) clusters³. In most of these studies [64, 71, 73] the results are obtained using *state-of-the-art* numerical implementations of density functional theory (DFT) which proved itself as a reliable theoretical tool for studying transition metal clusters both freestanding and on an oxide substrate [4, 13]. All authors agree that the most stable configuration of the gas-phase Ir_4 is the square (**S**) geometry. This configuration is significantly more stable than the tetrahedron (**T**) and the butterfly (**B**) structures. This result is in contradiction with the experimental findings for the geometry of supported Ir_4 clusters.

Results of an extensive theoretical study on the properties of different isomers of the gas-phase as well as oxide supported Ir_4 clusters are presented in this thesis. The influence of the chemical environment on the properties of the three most relevant Ir_4 isomers (**T**, **B** and **S**) is investigated. Special accent is put on the relative stability of the three isomers motivated by the already mentioned discrepancy between the theoretical predictions for the geometry

²As it will be shown in this thesis.

³Excluding the publications presenting the results obtained during this work [69, 70]

of the gas-phase Ir_4 and experimental findings for the supported species. As substrates the rocksalt $\text{MgO}(100)$ and rutile $\text{TiO}_2(110)$ oxide surfaces are chosen. Both of them are widely used in experiments and exhibit important differences in the structure and reactivity. Interaction of the three isomers, both free and supported, with H, C and O atoms and CO molecules is also studied. This choice of reactants is considered as the most relevant given the experimental procedure used to prepare Ir_4 . Namely, hydrogen could come from the surface hydroxyl groups, while C and O atoms could be present as fragments left on the surface after decarbonylation of the $\text{Ir}_4(\text{CO})_{12}$ precursor. In the case of partial decarbonylation also the CO molecules would be attached to the Ir_4 cluster.

In this work it is shown that chemical environment may cause drastic changes in both relative stability and reactivity of Ir_4 clusters [69, 70]. It is confirmed here that the **S** isomer is the most stable form of Ir_4 in the gas-phase. Moreover, deposition on $\text{MgO}(100)$ surface does not alter the relative stability predicted for the gas-phase species. However, one adsorbed carbon atom is sufficient to do so in both environments [69]. While in the gas-phase the most stable structure upon C adsorption becomes **B**, on $\text{MgO}(100)$ surface C adsorption changes the relative stability in favor of the **T** structure as observed in experiments [118, 119]. At variance to the adsorption of a single carbon atom, it is found that one H or O adatom does not modify the Ir_4 isomer stability observed for the pristine clusters [70]. Qualitatively, the same picture is accounted when H and O atoms are chemisorbed on Ir_4 clusters supported by $\text{MgO}(100)$. The TiO_2 substrate also affects the relative stability of the three isomers. Upon adsorption of the pristine clusters **T** structure becomes almost degenerate with **S**, bringing theoretical predictions closer to the experimental results [12, 126]. Moreover, the reactivities of the clusters towards C adsorption as well as CO adsorption and dissociation are also strongly affected.

The thesis is organized as follows. In the first part the methods used in this study are briefly described. Foundations of density functional theory are presented and the main approximations are overviewed (Chap.2). Afterwards, properties of the gas-phase Ir_n ($n = 1, \dots, 8$) clusters are presented (Chap.3). Relative stability between different isomers given for a fixed cluster size is discussed as well as the differences in their properties. Special attention is on the Ir_4 isomers. Bonding in Ir_4 is analyzed together with the differences in the electronic structures of the three isomers that lead to a given energy ordering. The relative stability of the three Ir_4 isomers is then compared with other transition metal tetramers. The details of the interaction of the gas-phase Ir_4 clusters with H, C and O atoms as well as with a single CO molecule are presented in the following chapter (Chap.4). The pathways for the CO dissociation are also studied.

The thesis also covers properties of supported Ir_4 clusters (Chapter 5). Interaction mechanisms with two oxide surfaces $\text{MgO}(100)$ and $\text{TiO}_2(110)$ are discussed as well as their influence on the relative stability of Ir_4 . Moreover, diffusion of Ir_4 on the $\text{MgO}(100)$ surface is studied together with their interaction with neutral and charged oxygen vacancies. The influence of adsorbates on the relative stability of supported Ir_4 is the subject of the last chapter and it is followed by the conclusions and the list of references.

Chapter 2

Density Functional Theory and Methods

2.1 Density Functional Theory

Probably the most important and most used methods of all *ab initio* electronic structure methods are based on Density Functional Theory (DFT). DFT is the theory of an interacting electron gas whose foundations lay in one theorem, the Hohenberg and Kohn (HK) theorem [17]. This theorem states that "*the ground state density of bound system of interacting electrons in some external potential determines this potential uniquely*" [18], where *uniquely* means up to an additive constant.

The HK theorem has two important implications: (i) by determining the external potential ground state density determines the system completely together with all its properties; and (ii) there is a universal functional for the energy $E[n]$ in terms of the density $n(\mathbf{r})$ whose global minimum, for a given external potential, is the exact ground state density $n_0(\mathbf{r})$ [19]. However, the theorem does not provide a way to construct the energy functional.

Kohn and Sham showed [20] that it is possible to replace the problem of interacting many-electron system by an auxiliary system of non-interacting fermions. Therefore, minimization of the (unknown) energy functional with respect to the electron density can be recast into a set of self-consistent one-electron equations. The Kohn-Sham (KS) energy functional can be written as

$$F[n(\mathbf{r})] = T_s[n(\mathbf{r})] + \int V_{ext}(\mathbf{r})n(\mathbf{r})d\mathbf{r} + E_H[n(\mathbf{r})] + E_{xc}[n(\mathbf{r})], \quad (2.1)$$

where $T_s[n]$ is the kinetic energy functional for the non-interacting many-electron system, $V_{ext}(\mathbf{r})$ is the external potential, $E_H[n]$ is the Hartree energy and $E_{xc}[n]$ is the exchange-correlation (XC) functional which is defined by Eq.2.1. The following set of one-particle, KS equations can then be derived by minimizing $F[n(\mathbf{r})]$ under the orthonormality condition for the wave functions

$$\left[-\frac{1}{2}\nabla^2 + V_{ext}(\mathbf{r}) + \int \frac{n(\mathbf{r}')}{|\mathbf{r} - \mathbf{r}'|}d\mathbf{r}' + V_{xc}(n(\mathbf{r})) \right] \psi_i(\mathbf{r}) = \epsilon_i^{KS} \psi_i(\mathbf{r}). \quad (2.2)$$

The quantity in brackets is the Kohn-Sham Hamiltonian consisting of the kinetic energy operator, external potential followed by the Hartree and XC potentials. The XC potential is derived as the functional derivative $\delta E_{xc}/\delta n$ of the XC energy functional with respect to

the density. The eigenvalues ϵ_i^{KS} enter into the formalism as the Lagrange multipliers for the orthonormality condition.

The XC energy functional is not known and needs to be approximated. Once, an appropriate approximation for E_{xc} is made, the KS equations are solved self-consistently starting from a certain $n(\mathbf{r})$ and constructing all terms in Eq.2.2. After the equations 2.2 are solved, the KS orbitals are filled according to the Pauli principle and the new density is constructed. For the set of doubly occupied KS orbitals $\{\psi_i\}$ (spin is neglected for simplicity) the total energy for the system of interacting electrons in the field of fixed nuclei can be calculated (in Hartree atomic units) as follows

$$E[\{\psi_i\}] = 2 \sum_i^{occ} \int \psi_i^* (-\frac{1}{2} \nabla^2) \psi_i d\mathbf{r} + \int V_{ion}(\mathbf{r}) n(\mathbf{r}) d\mathbf{r} + \frac{1}{2} \int \frac{n(\mathbf{r}) n(\mathbf{r}')}{|\mathbf{r} - \mathbf{r}'|} d\mathbf{r} d\mathbf{r}' + E_{XC}[n(\mathbf{r})] + E_{ion}[\{\mathbf{R}_I\}], \quad (2.3)$$

where all the terms are already known from Eq.2.1 except $E_{ion}[\{\mathbf{R}_I\}]$ which represents the electrostatic interaction between nuclei (ions).

2.1.1 The LDA and GGA Approximations and Beyond

The simplest and the most used approximation to DFT for $E_{xc}[n(\mathbf{r})]$ is the Local Density Approximation (LDA). The XC energy functional is written within the LDA in the form

$$E_{xc}^{LDA} = \int \epsilon_{xc}^{hom.}(n(\mathbf{r})) n(\mathbf{r}) d\mathbf{r} \Rightarrow V_{xc} = \frac{\delta E_{xc}}{\delta n} = \frac{d}{dn} [n \epsilon_{xc}^{hom.}(n)], \quad (2.4)$$

where $\epsilon_{xc}^{hom.}(n(\mathbf{r}))$ is the exchange–correlation energy per particle of a uniform electron gas of density n . This approximation, expected to produce accurate results only for systems with slowly varying densities, works remarkably well also for inhomogeneous systems (*i.e.* isolated atoms). The usefulness of the LDA is not only in its accuracy, but also in its simplicity. Namely, the KS equations in the LDA approximation are only slightly more complicated than Hartree equations¹ and are much more accurate. They are also much simpler than Hartree–Fock equations [67]. The success of LDA for the interacting electron systems (even inhomogeneous) can be, to a large extent, attributed to the fact that LDA satisfies the sum–rule for the exchange–correlation hole² [18, 19].

Early attempts to improve LDA by including the terms dependent on the density gradients in Eq.2.4 have not shown improvements compared to simple LDA. One of the reasons for the failure of these ”improvements” is the fact that simple gradient expansions do not obey the sum–rule for the exchange–correlation hole. Considerable efforts to construct the correct functionals have lead to Generalized Gradient Approximation (GGA). The GGA functionals can be written in the (general) form

$$E_{xc}^{GGA} = \int f(n(\mathbf{r}), |\nabla n(\mathbf{r})|) n(\mathbf{r}) d\mathbf{r}. \quad (2.5)$$

Many forms for $f(n, |\nabla n|)$ have been proposed up to now. Probably, the most used GGA functionals are those constructed by Perdew and Wang (PW91) [21], Perdew, Burke and

¹Which can be derived from the KS equations 2.2 by putting $V_{xc} = 0$.

²Depletion of the two particle density $n(\mathbf{r}, \mathbf{r}')$ around \mathbf{r} , with respect to the average density $n(\mathbf{r}')$, which integrates to 1.

Enzerhof (PBE) [22], and Becke, Lee, Yang and Parr (BLYP) [23, 24]. Use of GGA instead of LDA has reduced errors of atomization energies of molecules, energy barriers and structural energy differences (for details check reference [22] and the references therein). Improved accuracy as well as the development of numerical algorithms which enabled investigations of the properties of relatively large systems have made GGA an important component of today’s theoretical solid-state physics and quantum chemistry.

However, both LDA and GGA functionals contain a fraction of the self interaction error that is comprised in the Hartree term and cancelled completely only by the "exact", Fock exchange operator. Therefore, the so called hybrid XC functionals have been developed which include a portion of the Fock exchange added to the standard LDA/GGA functionals. They are typically constructed in the following way

$$E_{xc}^{hybrid} = E_c^{GGA} + (1 - \alpha)E_x^{GGA} + \alpha E_x^{Fock}, \quad (2.6)$$

where parameter α determines what portion of the exchange will be "exact". If the hybridization is done with the PBE (GGA) functional than it has been justified that for molecular systems it is appropriate to put $\alpha = 0.25$ leading to the widely used PBE0 hybrid functional [25]. Although hybrid functionals do improve DFT results when applied to semiconductors/insulators or small molecules consisting of light atoms, their description of the electronic structure of metallic systems is rather poor (wrong bulk cohesive energies, gap opening, unphysical broadening of the transition metal d bands,...) [26]. This is not surprising since it is known that the self-interaction error is almost negligible in metals. Moreover, it is also shown that, when applied to transition metal dimers, hybrid functionals do not yield results in better agreement with experiments than those obtained with GGA methods [59, 60, 61]. Therefore, the most appropriate approximation to DFT for studying transition metal clusters and their interactions with surfaces and/or other molecules is still GGA which was used in the PW91 functional form throughout this work³.

2.2 Methods

2.2.1 Pseudopotentials

Widely used approximation, where the Coulomb potential of nuclei is replaced by the pseudopotential, is based on the fact that the inner shell (core) electrons, in majority of cases, do not play a role in chemical bonding and are weakly affected by the environment surrounding the atom. It is a useful simplification to treat those electrons as "frozen" and incorporate their contribution in the potential that acts on valence electrons. The gain when using this approximation is not only in reducing the number of electrons that are treated explicitly, but also in reducing the number of plane-waves that are needed for accurate representation of the valence wavefunctions. A huge number of plane waves is needed mainly due to the orthogonality constraints of the valence wave functions to the core orbitals. Price for using pseudopotential approximation is their nonlocality and the arbitrariness in dividing electrons into core and valence.

When constructing pseudopotentials one starts from the all-electron calculation for a given atom solving the KS equation (Eq.2.2). Approximation of spherical screening is usually

³Dependence on the XC functionals used in simulations was verified by comparing GGA results with those obtained within LDA.

assumed⁴ leading to the radial equation

$$\left[-\frac{1}{2} \frac{d^2}{dr^2} + \frac{l(l+1)}{2r^2} + V_{eff}[\rho; r] \right] r R_{nl}(r) = \varepsilon_{nl} r R_{nl}(r), \quad (2.7)$$

where $V_{eff}[\rho; r]$ is the self-consistent one-electron potential (for example in the LDA approximation)

$$V_{eff}[\rho; r] = \frac{-Z}{r} + V_H[\rho; r] + V_{xc}^{LDA}[\rho]. \quad (2.8)$$

A following set of requirements is then imposed on the properties of pseudopotentials⁵:

1. all-electron and pseudo-valence eigenvalues agree for chosen atomic configuration,
2. all-electron and pseudo-valence wavefunctions agree beyond a chosen core radius R_{cl} ,
3. the logarithmic derivatives of the all-electron and pseudo-wavefunctions agree at R_{cl} ,
4. the integrated charge inside R_{cl} for each wavefunction agrees (norm-conservation),
5. the first energy derivative of the logarithmic derivatives of the all-electron and pseudo-wavefunctions agrees at R_{cl} (transferability).

Pseudopotentials that fulfill these conditions are referred as *norm-conserving*. The above set of conditions does not determine them uniquely and in practice, firstly the pseudo-wavefunctions with the desired properties are constructed and then the screened pseudopotentials, containing the influence of other valence electrons, are obtained by inverting Eq.(2.7). Since the screening properties of valence electrons depend strongly on the environment it is necessary to "unscreen" the pseudopotentials to ensure their transferability. One way to do this is to divide the electronic density into contributions of core and valence electrons $\rho = \rho_c + \rho_v$ and to subtract from the screened pseudopotential contribution to the electron-electron interaction coming from ρ_v

$$V_{ion,l}^{PP}(r) = V_{scr,l}^{PP}(r) - V_H[\rho_v; r] - V_{xc}[\rho_v]. \quad (2.9)$$

This is also an approximation since the $V_{xc}[\rho]$ is not linear in ρ . It is a fairly good approximation for systems whose ρ_c and ρ_v are spatially well separated, but for systems whose valence electrons penetrate considerably into the core region the nonlinearity of V_{xc} can produce serious errors. This problem is solved by modeling part of the core density that overlaps strongly with the valence and "unscreening" the pseudopotential by subtracting $V_H[\rho_v; r] + V_{xc}[\rho_c^{mod} + \rho_v]$ in Eq.(2.9). This, so called, non-linear core correction [42] improves significantly both accuracy and transferability of pseudopotentials.

In this way the norm-conserving pseudopotentials in the semi-local form (local in radial and non-local in angular variable) are obtained. This form is not suitable for practical applications and they are usually transformed into a fully non-local form using a procedure proposed by Kleinman and Bylander [43].

⁴This approximation is very useful, it simplifies considerably the equations and allows description of the electron dynamics in terms of hydrogen-like atomic orbitals since they can be labeled using the angular momentum quantum numbers. For open shell systems it relies on the assumption that the atomic core is spherical and that the effects of the reduced symmetry are significant only for the valence electrons.

⁵Formulation of these requirements from Reference [19] is adopted in this work.

On the other hand the norm-conservation condition imposes a lower limit to the number of basis functions because of the difficulty in representing the pseudo-wavefunctions in a plane-wave basis set for systems containing highly localized atomic orbitals (*i.e.* first row elements and transition metals). It has been shown that this condition can be omitted [44], recasting the original eigenvalue problem into the generalized one (involving the overlap operator). These pseudopotentials, often refferred as the "ultrasoft", can also be written in a fully non-local form (with the help of the bracket notation)

$$V = V_{loc} + \sum_{i,j} B_{ij} |\beta_i\rangle \langle \beta_j|, \quad (2.10)$$

where the β_i functions are angular momentum eigenfunctions in the angular variables, times a radial function which vanishes outside the core. Indices i and j go over total number of these functions. The β_i functions as well as B_{ij} coefficients characterize the pseudopotential and differ for different atomic species. As a consequence of abandoning the norm-conserving condition the pseudo-wavefunctions can be much smoother in the core region thus requiring much less plane waves to be accurately represented.

The pseudo-wavefunctions are no longer normalized and the electronic density is expressed in a more complex form

$$n(\mathbf{r}) = \sum_i \left[|\phi_i(\mathbf{r})|^2 + \sum_{n,m} Q_{nm}(\mathbf{r}) \langle \phi_i | \beta_n \rangle \langle \beta_m | \phi_i \rangle \right], \quad (2.11)$$

where ϕ_i are pseudo-wavefunctions and Q_{nm} are augmentation functions that are localized in the core region and are also provided by the pseudopotential. These augmentation functions serve to reproduce correctly the electronic density inside the core and can also vary rapidly in space. Therefore the problem of rapidly varying pseudo-wavefunctions is transferred to Q_{nm} functions also requiring large number of basis functions. Solution for this problem is to pseudize the "hardest" part of the augmentation functions. In practice it is done in such a way to preserve all of the charge moments inside the core [45]. This is one more advantage of the ultrasoft compared to the norm-conserving pseudopotentials that reproduce correctly only the total charge inside the core while the information about the core charge distribution is completely lost. This may lead to differences between those two types of pseudopotentials also outside the core⁶.

In this work the ultrasoft pseudopotentials are used. They are taken from the pseudopotential library of the DACAPO code [34]. These pseudopotentials are constructed using the code developed in the group of David Vanderbilt [48] and tested by a broader community of users. Of course, the tests have also been performed by the author of this thesis on a number of systems before any serious simulation required by the planning of this project took place. The test systems that were used are bulk fcc iridium and Ir(111) surface, bulk MgO and TiO₂ as well as their surfaces (100) and (110), respectively. Molecular O₂, CO and Ir₄(CO)₁₂ have also been used for testing purposes. Good agreement with experimental results is achieved which confirmed applicability of these pseudopotentials.

2.2.2 The Supercell Approximation and Plane Wave Expansions

This thesis is a result of a theoretical study on the properties of the gas-phase Ir clusters as well as Ir clusters adsorbed on an oxide surface. The studied systems are not periodic in

⁶Especially for open-shell atoms due to non-zero higher order charge moments.

space. However, it is convenient to make the system artificially periodic by constructing an array of periodically repeated images (supercells) of the original system. This approximation allows one to use theoretical tools developed for the periodic systems such as the plane wave expansions. The plane wave basis set has the advantage of being easily controllable in the sense that the size of basis set can always be increased until the convergence of the desired physical property is reached. The second advantage is a relatively simple and computationally not too expensive algorithms for molecular dynamics (see Sec.2.2.4). Moreover, one could also take the advantage of the highly optimized and parallelized routines for the fast Fourier transformation. However, the disadvantage of the supercell approximation is undesired interaction between the periodic images. If the system is charge neutral and does not carry a dipole moment, these interactions can be suppressed by increasing the supercell size. However, charged or polarized systems suffer from the long range character of the electrostatic interactions regardless of the supercell size. This issue is further elaborated in Sec.2.2.3 and ways to overcome this problem especially for polarized systems are discussed.

The supercell approach is used throughout this work for simulations of small iridium clusters both isolated (in the gas-phase) and adsorbed on an oxide surface. Two existing computer codes DACAPO [34] and QUANTUM-ESPRESSO [35] with the *state-of-the-art* numerical implementation of the DFT using plane wave basis set are used for calculations.

When studying properties of crystalline (periodic) systems the problem of dealing with an infinite system with infinitely many electrons is simplified by using the Bloch theorem [27] which states that one-electron wave function for an electron in an infinite periodic potential must be of the form

$$\psi_{\mathbf{k}}(\mathbf{r}) = C e^{i\mathbf{k}\cdot\mathbf{r}} u_{\mathbf{k}}(\mathbf{r}), \quad (2.12)$$

where C is the normalization constant and $u_{\mathbf{k}}(\mathbf{r})$ is a periodic function with the periodicity of the lattice. There are two main consequences of Bloch theorem which enable very efficient calculations of the properties of bulk systems. First, the periodic part of $\psi(\mathbf{r})$ can be expanded into the plane-waves with the same periodicity

$$u_{\mathbf{k}}(\mathbf{r}) = \sum_{\{\mathbf{G}\}} c_{\mathbf{k}+\mathbf{G}} e^{i\mathbf{G}\cdot\mathbf{r}} ; \quad c_{\mathbf{k}+\mathbf{G}} = \frac{1}{\Omega} \int_{\Omega} u_{\mathbf{k}}(\mathbf{r}) e^{-i\mathbf{G}\cdot\mathbf{r}} d\mathbf{r}, \quad (2.13)$$

where $\{\mathbf{G}\}$ are the reciprocal lattice vectors and Ω is the unit cell volume. Analysis show that the plane-waves with relatively small kinetic energies $(\hbar^2/2m)|\mathbf{k} + \mathbf{G}|^2$ typically contribute more to the wave functions than those with large kinetic energies (see reference [19], p. 93). Therefore, the plane wave basis set can be truncated to include only those plane waves with kinetic energies below a certain cutoff energy. The truncation of the basis set produces errors in the computed properties of the system. However, these errors can be controlled by increasing the cutoff energy until the convergence of the desired property is reached.

Second, and not less important consequence of the Bloch theorem is that solving of the one-electron Schrödinger equation can be simplified by reducing it only to the volume of one unit cell of the crystal. However, it is still necessary to diagonalize one-electron Hamiltonian at infinitely many \mathbf{k} points in the first Brillouin zone of the reciprocal lattice. The fact that the wave functions do not differ much for the two \mathbf{k} points which are sufficiently close, allows a discrete sampling of the Brillouin zone. Moreover, it is possible to define a single \mathbf{k} point (Baldereschi point or the mean value point [28]) at which the value of any function of \mathbf{k} can be used as a good approximation to the integral of the same function over the whole Brillouin zone. Generalization of this idea lead to the special sets or grids of \mathbf{k} points in the

Brillouin zone, two of which are still in use in today's computer codes (Chadi–Cohen [29] and Monkhorst–Pack [30]).

When a plane wave basis set is used equations 2.2 take very simple form [31]

$$\sum_{\{\mathbf{G}'\}} \left[\frac{1}{2} |\mathbf{k} + \mathbf{G}|^2 \delta_{\mathbf{G}\mathbf{G}'} + V_{ion}(\mathbf{G} - \mathbf{G}') + V_H(\mathbf{G} - \mathbf{G}') + V_{XC}(\mathbf{G} - \mathbf{G}') \right] c_{i,\mathbf{k}+\mathbf{G}'} = \quad (2.14)$$

$$= \epsilon_i^{KS}(\mathbf{k}) c_{i,\mathbf{k}+\mathbf{G}}.$$

When expanded into a plane wave basis set the kinetic energy is a diagonal matrix and all potentials are expressed in terms of their Fourier components⁷. Equations 2.14 are then solved by diagonalizing Hamiltonian matrix $H_{\mathbf{k}+\mathbf{G},\mathbf{k}+\mathbf{G}'}$ given in the brackets above. Although the form of equations 2.14 is simple, matrix diagonalization is not an easy task. Especially for systems that contain localized electronic orbitals (*i.e.* core electrons of heavy atoms, valence d electrons) the number of plane waves needed to make the basis set sufficiently complete grows immensely and those calculations are not tractable even using today's computers. This problem can be overcome by use of the pseudopotential approximation as discussed in Sec.2.2.1.

The last term $E_{ion}[\{\mathbf{R}_I\}]$ in Eq.2.3 is also not easy to compute. It is very difficult to deal with it by using direct real-space summation due to the long range nature of the Coulomb interaction. Transferring the problem into the reciprocal space also does not help since the Coulomb interaction is long ranged in the reciprocal space, too. The problem was solved by Ewald [32] who divided the Coulomb energy of a periodic array of point charges in two parts, one short and one long ranged. The first part converges fast in the real space while the second converges fast in the reciprocal space. Each of them is then computed in the corresponding fast-converging space as follows⁸

$$E_{ion} = \frac{1}{2} \sum_{I,J} Z_I Z_J \times$$

$$\times \left[\sum_l \frac{\text{erfc}(\eta|\mathbf{R}_I + l - \mathbf{R}_J|)}{|\mathbf{R}_I + l - \mathbf{R}_J|} - \frac{2\eta}{\sqrt{\pi}} \delta_{IJ} + \frac{4\pi}{\Omega} \sum_{\mathbf{G} \neq 0} \frac{1}{|\mathbf{G}|^2} e^{-\frac{|\mathbf{G}|^2}{4\eta^2}} \cos[(\mathbf{R}_I - \mathbf{R}_J) \cdot \mathbf{G}] - \frac{\pi}{\eta^2 \Omega} \right]. \quad (2.15)$$

The term in brackets is the Coulomb energy due to the interaction between an ion positioned at \mathbf{R}_J and an array of ions positioned at $\mathbf{R}_I + l$ and is valid for any positive value of η . The two summations in brackets become rapidly converging for an appropriate value of η . Z_I and Z_J are the valences of ions I and J , respectively. Since the ions do not interact with themselves the $l = 0$ term for $I = J$ needs to be excluded from the summation.

2.2.3 Dipole Correction Method

The dipole correction method is used in periodic supercell calculations, when studying nonperiodic systems, to remove electrostatic dipole interactions between the periodic images. These

⁷Divergent $\mathbf{G} = 0$ term of both ionic and Hartree potentials is not included in Eq.2.14 since it cancels exactly with the same term of the ion-ion interaction when the total energies are computed.

⁸The following formula, in which certain inaccuracies related to the $G = 0$ term are resolved, is taken from reference [33].

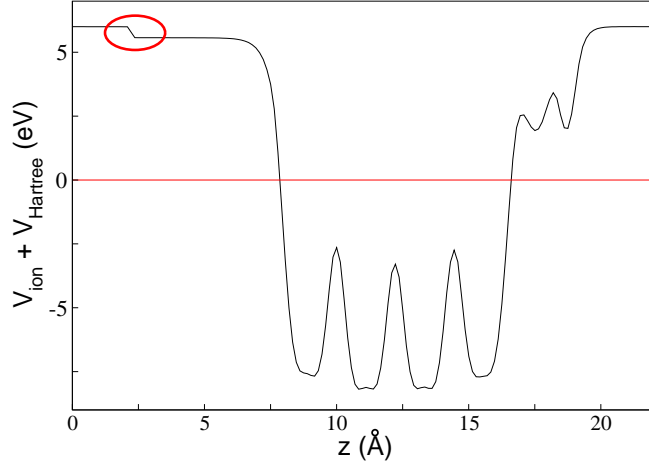


Figure 2.1: Electrostatic potential of the four layer Ir(111) slab with a CO molecule adsorbed on one side of the slab. The potential plotted in the direction perpendicular to the surface. Zero of the potential is put to the Fermi level of the system. Red ellipse encloses the potential drop due to the planar dipole layer placed in the vacuum region.

interactions appear when the system of interest has a nonzero dipole moment. An infinite periodic array of dipole moments leads to a macroscopic electrostatic field which influences the electrostatic potential of the system under consideration.

These problems typically appear when studying adsorption on surfaces. As a consequence of the charge transfer between the surface and the adsorbate the system develops a dipole moment in the direction perpendicular to the surface. One way of dealing with these kinds of errors is to duplicate the system in the unit cell in such a way that the dipole moments cancel. This is done in practice by using the symmetric slab with the adsorbate on both surfaces of the slab. However, the system size is doubled and the calculations are much more expensive which is not favorable for systems containing big number of atoms (of the order of 100 and more).

Second way of removing the dipole field in periodic supercell calculations is proposed by Neugebauer and Scheffler [36]. The idea is to add to the system an artificial planar dipole layer placed far away from the examined system inside the vacuum region, whose dipole strength is calculated selfconsistently in such a way that the adsorbate induced dipole field is compensated for (see Fig.2.1). In this way the asymmetric slabs with the adsorbates only on one side of the slab while the other side is kept fixed mimicking the bulk, can be used and the system size can be kept reasonably small. Moreover, the method can be generalized in order to treat the interaction of a true external electrostatic field with a surface or a molecule. Both possibilities are used in this work, the first to cancel adsorbate induced dipole fields and the second to study how the external field influences relative stability of Ir₄ clusters (check Sec.5.6).

2.2.4 Ionic Forces and Vibrational Analysis

The electronic structure calculations typically rely on a number of approximations. The first one presented in this thesis is the approximation for the exchange and correlation energy to density functional theory (LDA or GGA). However, the basic approximation used in the

majority of theories that deal with the electronic structure of matter, is the adiabatic or Born–Openheimer approximation [37]. This approximation allows to decouple the electronic degrees of freedom from the ionic ones because of the large difference in their masses. The ionic positions are then treated in the electronic structure calculations as parameters. The total energy of the system (Eq.2.3) can then be viewed as function of the ionic positions $E(\{\mathbf{R}_I\})$.

Moreover, the adiabatic approximation also allows relatively simple treatment of the dynamics of the ionic subsystem. The ionic motion is typically described by the classical (Newton) equations of motion for which the forces that are determined by $E(\{\mathbf{R}_I\})$ have quantum mechanical origin. The force acting on the ion positioned at \mathbf{R}_J is defined as

$$\mathbf{F}_J = -\frac{\partial E(\{\mathbf{R}_I\})}{\partial \mathbf{R}_J} = -\frac{\partial}{\partial \mathbf{R}_J} \langle \psi_0(\{\mathbf{R}_I\}) | H(\{\mathbf{R}_I\}) | \psi_0(\{\mathbf{R}_I\}) \rangle - \frac{\partial E_{ion}[\{\mathbf{R}_I\}]}{\partial \mathbf{R}_J}, \quad (2.16)$$

where $\psi_0(\{\mathbf{R}_I\})$ is the electronic ground state, $H(\{\mathbf{R}_I\})$ is the Hamiltonian of the electronic subsystem and $E_{ion}[\{\mathbf{R}_I\}]$ is the electrostatic *ion–ion* interaction energy. All these terms depend explicitly on the ionic configuration. Computation of the derivative of the ground-state expectation value of the electronic Hamiltonian can be simplified by using the Hellmann–Feynman theorem that states

$$\frac{\partial}{\partial \mathbf{R}_J} \langle \psi_0(\{\mathbf{R}_I\}) | H(\{\mathbf{R}_I\}) | \psi_0(\{\mathbf{R}_I\}) \rangle = \langle \psi_0(\{\mathbf{R}_I\}) | \frac{\partial H(\{\mathbf{R}_I\})}{\partial \mathbf{R}_J} | \psi_0(\{\mathbf{R}_I\}) \rangle. \quad (2.17)$$

Within DFT the only terms in the total energy of the system (Eq.2.3) that depend explicitly on the ionic configuration are the terms that describe electron–ion and ion–ion interactions. Therefore, the expression 2.16 for the force acting on the ion positioned at \mathbf{R}_J after the implementation of the relation 2.17 becomes

$$\mathbf{F}_J = - \int n_{\mathbf{R}}(\mathbf{r}) \frac{\partial V_{\mathbf{R}}(\mathbf{r})}{\partial \mathbf{R}_J} d\mathbf{r} - \frac{\partial E_{ion}[\{\mathbf{R}_I\}]}{\partial \mathbf{R}_J}, \quad (2.18)$$

where $n_{\mathbf{R}}(\mathbf{r})$ and $V_{\mathbf{R}}(\mathbf{r})$ are the electronic ground state density and the electron–ion interaction potential, both corresponding to the nuclear configuration \mathbf{R} . This expression allows very efficient simulations of the nuclear dynamics within DFT formalism. The equilibrium geometry of the system is given by the condition $\mathbf{F}_J = 0$, that all forces acting on the nuclei vanish. It can be used for finding the equilibrium configurations of the system. Moreover, by introducing the concepts of the ionic temperature and the canonical ensemble or adding history dependant (penalty) potentials in order to forbid the system to adopt already ”visited” configurations (scanning the potential energy landscape) various kinds of molecular dynamics can be studied.

The plane wave expansion (Sec.2.2.2) appears to be very useful in calculating ionic forces which can be computed analytically since the nuclear positions enter into the DFT formalism either in the ionic interaction energy (2.15) or as exponents in the structure factors that multiply Fourier components of the ionic potential. Moreover, the plane waves do not depend on the ionic positions inside the unit cell and the Hellmann–Feynman expression for the forces (Eq.2.18) is valid without any corrections (which is not true for the localized basis sets).

On the other hand, the second derivatives of the KS energy functional with respect to the ionic displacements, which are important for studying vibrational properties, cannot be computed analytically since they require calculations of the first derivatives of the ground state

electronic density $\partial n_{\mathbf{R}}(\mathbf{r})/\partial \mathbf{R}_j$ (check Eq.2.18). Two solutions for this problem are widely used in scientific community, the frozen phonon approximation and the density functional perturbation theory (references [19, 38]). In the former the second derivative of the energy with respect to the displacement of a certain atom is computed by displacing the atom in each of the three principal directions (both parallel and antiparallel) and calculating the total energy of the system. It is therefore, necessary to perform $6N$ calculations (N is the number of atoms in the unit cell) in order to compute all second order derivatives needed for construction of the dynamical matrix whose diagonalization leads to the vibrational spectrum of the system. However, in this way only the vibrations at the Γ point of the Brillouin zone can be studied. The vibrational spectrum at a generic \mathbf{k} -point in the Brillouin zone can be computed in the frozen phonon approximation by increasing the cell size to the wavelength of the desired phonon mode and repeating the same procedure. This is feasible only for phonons with relatively short wavelengths.

The full vibrational spectrum of the periodic systems can be computed with much less effort using the density functional perturbation theory (DFPT) approach [38]. A linear set of equations similar to KS equations for the variations of the electronic wave functions due to the perturbation of the system (in this case nuclear displacements) needs to be solved in order to compute the (linear) response of the electronic density needed for calculations of the density derivatives with respect to the nuclear displacements. The advantage of the DFPT is that the responses to perturbations with different wavelengths can be decoupled. This allows computations of the phonon frequencies at arbitrary wave vector \mathbf{q} avoiding the use of the supercells.

Since this work is concentrated on the systems which are mostly nonperiodic (isolated clusters and clusters adsorbed on surfaces) calculations of the vibrational spectra only at the Γ -point are relevant. Therefore, the frozen phonon approach is used for all phonon calculations. At this point it is important to underline that the atomic displacements in these calculations need to be small enough to ensure the validity of the harmonic approximation. This implies that the equilibrium configuration needs to be very well converged. Therefore, in this work all configurations used for studying the vibrational properties are considered as equilibrium configurations when the sum of all the forces acting on ions does not exceed $0.01 \text{ eV}/\text{\AA}^9$. The atomic displacements used in calculations can then be of the order of 0.01 \AA . Such a displacements produce the total energy differences between the ground state and the perturbed configurations of small Ir clusters of the order of 0.001 eV confirming the need for a very well converged structures.

2.2.5 Transition-state Theory and The Nudged Elastic Band (NEB) Method

Everything said up to this point is related mostly to the ground state properties of the system. DFT is a theory of the electronic ground state for a given atomic configurations which is not necessarily the ground state for the ionic subsystem. Therefore, the properties of the system that is far from equilibrium can also be studied under the constraint imposed by the adiabatic approximation¹⁰. This is typically done in the molecular dynamics simulations (see for example reference [31]). However, the activated processes in which the system undergoes a

⁹This does not apply to the adsorption of Ir_4 clusters at surfaces. The forces acting on the fixed ions from the surface bottom layer may be bigger and only the forces acting on nuclei which are allowed to relax are taken into account.

¹⁰That the electrons remain at each moment at their ground state for any reasonable atomic configuration.

transition from one local minimum to another across an energy barrier are extremely difficult to study by the means of standard molecular dynamics. Processes with a relatively low activation energy of 0.5 eV would require years of computer time to simulate classical trajectory of the system in order for a single transition event to be expected to occur.

This problem can be overcome and accurate estimates of the transition rates can be obtained by using the transition state theory (TST) [39]. In addition to the adiabatic approximation TST relies on two assumptions: (i) the rates are slow enough and a Boltzmann distribution describes the reactant state; and (ii) the initial and final states can be separated in the configurational space by a D-1 dimensional surface (D is the number of degrees of freedom) in such a way that the trajectory going from one state to the other crosses this surface only once. Since the range temperatures of interest, when considering condensed matter systems, lays typically far below the melting temperature, the harmonic approximation to TST (hTST) can be used for studying diffusion or reactions at crystal surfaces. This simplifies the problem which becomes that of finding the saddle point (transition state) along the minimal energy path (MEP) connecting the two states (initial and final). The rate constant for the transition can be obtained from the energy and the frequency of the normal modes of the initial and transition state [41]

$$k^{\text{hTST}} = \frac{\prod_i^{3N} \nu_i^{\text{init}}}{\prod_i^{3N-1} \nu_i^*} e^{-(E^* - E^{\text{init}})/k_B T}, \quad (2.19)$$

where E^* and E^{init} are the energies of the saddle point and initial state, respectively. The ν_i appearing in the prefactor that multiplies the exponential term in Eq.2.19 are the corresponding normal mode frequencies. In the cases where transition occurs along one of the normal modes of the initial states the whole prefactor or the attempt frequency could be approximated with the frequency of that mode solely. Moreover, in the solid state systems the frequencies are of the order of 10^{12} – 10^{13} Hz. These values are often used in the scientific community for rough estimations of the rate constants.

The MEP often has one or more minima in addition to those at the initial and final states which correspond to the (meta)stable intermediate configurations. Therefore, along the MEP there are also several saddle points, one between each pair of the neighboring minima. If a Boltzmann population is reached for the intermediate configurations the overall rate is then determined by the highest transition state.

Various methods are in use for calculating MEPs and finding the transition states. One of the most efficient is the nudged elastic band (NEB) method [40]. It has been widely used together with hTST. The idea is to discretize the initial path (guess) in the configurational space of the system between the two end points and to relax each of the resulting configurations only in the directions perpendicular to the path. This is done by putting all components of the forces that lay along the path to zero and performing standard minimization techniques. However, the definition of the tangent as well as the number of points used for discretization is crucial (see more about this in reference [40]). Since the relaxation of each point depends on the tangent and therefore on the configurations of other points, the relaxation towards the MEP is performed simultaneously for all points along the path. To prevent grouping of the images and other types of path instabilities the spring forces are added between neighboring configurations making an elastic band in the configurational space. The tangential components of the spring force are used to control the spacing between images (normal components are set equal to zero). Calculations of the energies and forces of different configurations are typically done using DFT methods.

The climbing image nudged elastic band method (CINEB) [41] can then be used to find the saddle points along the path. After the initial path has approached closer to the MEP the appropriately chosen configuration (or configurations) is detached from the springs and allowed to relax also in the tangential direction. This relaxation is done with inverted the tangential components of the forces. In this way the chosen configuration climbs to the point with the zero force, which is a minimum in all directions perpendicular to the path and a maximum in the tangential direction, the first order saddle point or the transition state.

In this work the CINEB method is mostly used to calculate barriers for structural transformations between different Ir_4 isomers. It is also used for calculations of the MEPs and finding the transition states for the CO dissociation on both gas-phase and $\text{MgO}(100)$ supported Ir_4 clusters. Pathways between different local minima are discretized and minimal set of five intermediate configurations is used at the beginning of simulations. Saddle points are found, for a fixed number of images along the MEP, by relaxing appropriately chosen intermediate configuration (configurations) along the path in the direction opposite to the forces, until the total force in this configuration reached the threshold of $0.05 \text{ eV}/\text{\AA}$. Afterwards, the number of images is increased and the convergence is achieved when energy of the saddle point (converged for a fixed number of images) changes less than 0.05 eV .

Chapter 3

Gas-phase Iridium Clusters

3.1 Iridium Atom

Iridium is a $5d$ transition metal with atomic number $Z = 77$ which, in addition to the electronic structure of Xe atom, has completely filled $4f$ and outer $6s$ subshell while the remaining seven electrons are accommodated in ten $5d$ orbitals ($[\text{Xe}]4f^{14}5d^76s^2$ [5]) giving rise to magnetic moment of $3 \mu_B$. The $5d$ and $6s$ electrons are usually treated as valence when constructing iridium pseudopotential, as it is done in this work.

As already mentioned in Sec.2.2.1 the ultrasoft pseudopotentials (USPP) are used throughout this work. They are constructed within the GGA framework with exchange and correlation energies described by PW91 XC functional [21]. The non-linear core-corrections (Sec.2.2.1) are added to iridium PP in order to take into account the nonlinearity of the exchange interaction between the valence and the core electrons. Relativistic effects are treated at the scalar level [94] neglecting the spin-orbit interaction. Bulk fcc iridium is used as the test system. Sampling of the fcc iridium Brillouin zone is done with $10 \times 10 \times 10$ Monkhorst-Pack \mathbf{k} -point grid [30]. The same plane wave and density cutoffs, which determine the size of the plane wave basis set, are used as for simulations of small Ir clusters (see below). Bulk parameters, the equilibrium lattice constant $a_0 = 3.85 \text{ \AA}$, bulk modulus $B_0 = 356 \text{ GPa}$ and cohesive energy $E_c = 7.48 \text{ eV}$, are obtained by fitting numerical results to the Murnaghan equation of state [49]. These results are in line with other calculations [50, 51]. When compared to experimental values ($a_0 = 3.84 \text{ \AA}$, $B_0 = 306 - 355 \text{ GPa}$ and $E_c = 6.94 \text{ eV}$ [52, 53]) it can be seen that the lattice constant is well reproduced (error $\sim 0.3 \%$) while E_c is overestimated by about 8% which are typical features of DFT methods.

In Fig.3.1 Kohn-Sham electronic spectrum of Ir atom is shown. Calculations are performed in a cubic unit cell with linear dimension $\sim 10.58 \text{ \AA}$ (20 Bohr). This cell size provides good convergence of the properties of small Ir clusters (cohesive energy, interatomic distances,...). Electronic wavefunctions are expanded in plane waves with the kinetic energy cutoff of $25 \times 13.606 \text{ eV}$. Cutoff for expanding the electronic density is set to $140 \times 13.606 \text{ eV}$ ensuring appropriate description of the pseudopotential augmentation functions (see Sec.2.2.1). These cutoffs provide sufficiently complete basis set for simulating small Ir clusters. Converged values of the physical quantities of interest, cohesive energies of small Ir clusters in particular, are obtained in this way¹.

¹Cohesive energy of iridium dimer changes by less than 0.02 eV when the cutoffs increase to 30×13.606 and $160 \times 13.606 \text{ eV}$, respectively.

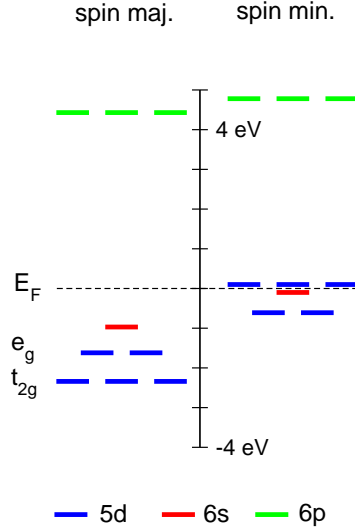


Figure 3.1: Spin resolved Kohn-Sham electronic spectrum of Ir atom.

Calculated population of atomic orbitals of Ir atom ($5d^76s^2$) compares well with experiment. However, this result is dependent on the super-cell symmetry. Due to the fact that d -shell is not completely filled there is a number of Slater determinants close in energy which are candidates for the atomic ground state. Different determinants are the ground state of Ir atom for different boundary conditions. This affects the atomic total energy, *i.e.* total energies of Ir atom calculated in hexagonal and triclinic super-cell differ by ~ 0.12 eV for the same nearest neighbor distance. Energy of an atom is typically used as a reference for calculating cohesive energies of more complicated systems. Different reference atom is one of the reasons for differences in cohesive energies of transition metal clusters reported in literature.

Cubic super-cell is chosen in this work for simulating Ir atom since, due to symmetry reasons, it does not allow mixing of s and d angular momentum channels which is the closest possible to the situation of an isolated Ir atom. However, it leads to cubic splitting of $5d$ orbitals into t_{2g} triplet and e_g doublet². This splitting is also a consequence of the symmetry of d orbitals and the number of electrons filling them. In order to minimize Coulomb repulsion, two or three d electrons in the spin minority channel will always tend to occupy only one d orbital in xy plane ($d_{x^2-y^2}$ or d_{xy}) and one or two orbitals orthogonal to that (d_{z^2} or d_{xz} and d_{yz}) which will lead to electronic density with the octahedral or cubic symmetry and consequently to t_{2g} - e_g splitting of d orbitals.

3.2 Ir Dimer

Results for iridium dimer are presented separately from bigger Ir_n ($n = 3, \dots, 8$) clusters since the dimer presents a basis for studying Ir-Ir bonding mechanism. Two reviews on transition metal dimers appeared in literature in the last 25 years [56, 57]. Both authors find a lack of experimental data on iridium dimer. They report only empirical estimates of the dimer

²The term *cubic* is used in the sense that the splitting is produced by reducing the symmetry from rotational $\text{SO}(3)$ to O_h group which is a symmetry group of both cube and octahedron. The t_{2g} and e_g denote respectively, triply and doubly degenerate irreducible representations of O_h group.

dissociation energy of 3.7 [56] and 3.5 eV [57] with the error bars as big as ~ 1 eV. On the other hand, several theoretical studies have been published recently treating the group VII transition metal dimers and comparing performances of different numerical approaches based on DFT [59, 60, 61]. It is shown that dissociation energies, magnetic moments as well as vibrational frequencies depend strongly on the XC functional used, while the dependence is less pronounced for the dimer bond distance. Moreover, in references [59, 61] the authors show that "pure" DFT methods (GGA) yield results in better agreement with experiments (in the cases where experimental results exist) than hybrid DFT schemes which are usually considered as more accurate. In addition to these, there is one GGA (PW91) study of the gas-phase iridium clusters consisting of 2–64 atoms [64] and one multiconfigurational self-consistent-field investigation on hydrogen activation by iridium dimers [62]. In both cases results for clean Ir_2 go in line with those obtained with corresponding method from the aforementioned references.

Properties of iridium dimer obtained in this work are presented in Tab.3.1 together with the bigger Ir clusters. Numerical setup is discussed in the previous section. Cohesive energy of 2.52 eV/atom, calculated as the difference $E_c = -(E(\text{Ir}_2) - 2E(\text{Ir}))/2$, agrees well with the value of 2.53 eV reported in reference [64] obtained using similar approach (ultrasoft PP and PW91 XC functional). This value together with calculated frequency of the dimer stretching mode $\hbar\omega_e = 33.6$ meV lays within the range ($E_c = 1.62\text{--}3.02$ eV and $\hbar\omega_e = 33.2\text{--}37.3$ meV) of all-electron GGA calculations [60, 61]. Spread in the reported E_c values is typically quite big for transition metal clusters. There are two main reasons for this: (i) E_c is calculated using total energy of an atom as a reference and, as already mentioned in Sec.3.1, different approaches yield different atomic ground state; and (ii) since molecular orbitals in transition metal clusters are formed either exclusively of atomic d orbitals or of dsp hybrid orbitals (see later in the text and in Sec.3.4) differences also arise from different description of the level of dsp hybridization which is very sensitive to the details of numerical approach.

The dimer bond distance of 2.17 Å calculated in this work is shorter than those (2.24–2.29 Å) reported in references [60, 61] and considerably shorter than 2.43 Å from reference [62]. Since, the interatomic distances in small Ir clusters from this work agree well with results from other calculations using pseudopotentials (see for example reference [65]) it might be concluded that somewhat shorter distances result from the pseudopotential approximation. However, test calculations with the pseudopotential that includes semicore 5s and 5p atomic orbitals resulted in the dimer bond length of 2.19 Å, only slightly bigger. Therefore, the differences in the Ir–Ir distance between pseudopotential and all-electron calculations probably reflect differences in numerical approaches (*i.e.* local versus plane wave basis sets,...) and the sensitivity of the d – s hybridization level on the details of the numerical scheme³.

Bonding mechanism in Ir_2 is similar to other platinum group transition metal dimers with partially filled d -shell. As it is usually done when studying bonding in molecules, molecular orbitals (MO) formed upon interaction, can be classified (and labeled) according to irreducible representations of the corresponding symmetry group. If a spherical symmetry is assumed for Ir atom then, by forming the dimer, symmetry is lowered to $\mathbf{D}_{\infty h}$ axial point group containing rotational axis of the infinite order and two mirror planes, vertical σ_v and horizontal σ_h ⁴. Since the vertical mirror plane associates atomic orbitals (AO) with opposite m_l values (angular

³This can be supported by the fact that just by replacing the ultrasoft with norm-conserving pseudopotential results for the dimer change ($d = 2.21$ Å and $E_c = 2.36$ eV).

⁴Due to the infinite order of the principal rotational axis there are infinitely many equivalent vertical mirror planes, but only one horizontal.

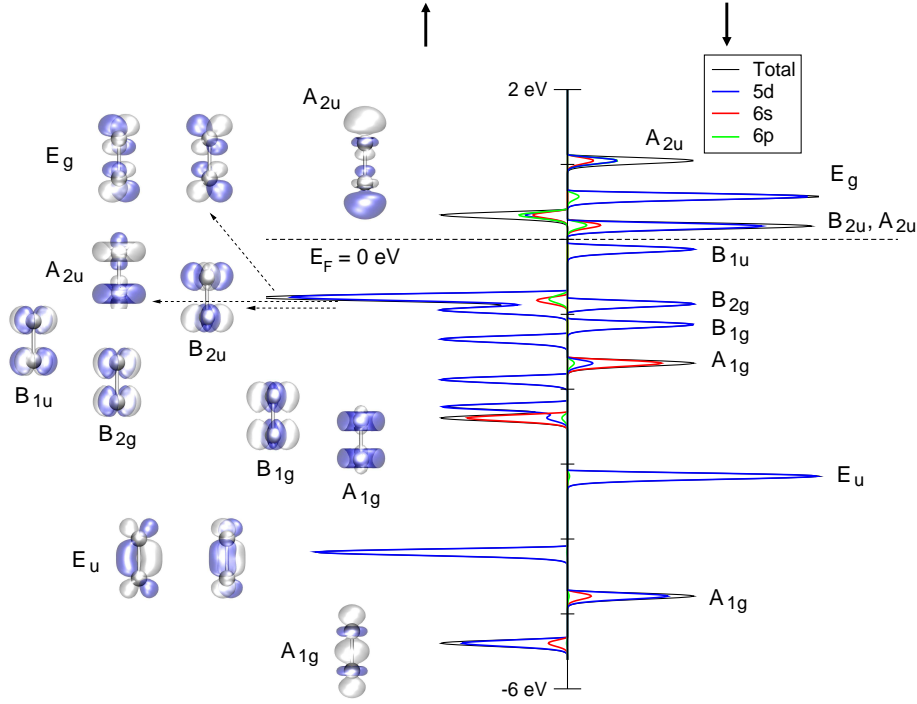


Figure 3.2: Spin resolved DOS of iridium dimer (\uparrow -spin maj. and \downarrow -spin min.). Gaussian broadening with the width of 0.07 eV is employed. The Fermi energy is positioned in the middle of the HOMO–LUMO gap. Projections onto orthogonalized atomic orbitals (see reference [55]) are also shown. Molecular orbitals, displayed in the left part of the figure, are labeled according to the symmetry properties with respect to \mathbf{D}_{4h} symmetry group (see text for details).

momentum along the principal axis) the $5d$ multiplets on each atom will split to $m_l = 0$ singlets (d_{z^2}) and $|m_l| = 1, 2$ doublets ($\{d_{xz}, d_{yz}\}$ and $\{d_{x^2-y^2}, d_{xy}\}$). The consequence of σ_h is mixing the orbitals from different Ir atoms. Therefore, AOs from both atoms with the same $|m_l|$ form a subspace that can be reduced, using the parity with respect spatial inversion (equivalently the parity with respect to σ_h can be used), to one or two dimensional even (g) or odd (u) irreducible representations of $\mathbf{D}_{\infty h}$ group.

Population of molecular orbitals (MO) reduces further the symmetry of the system. There is only one electron filling the antibonding spin minority E_{2u} doublet of the $\mathbf{D}_{\infty h}$ group. Given the shape of any of the two E_{2u} orbitals (antibonding combination of either d_{xy} or $d_{x^2-y^2}$ atomic orbitals from the two atoms) symmetry of the electron density is lowered to \mathbf{D}_{4h} group. This produces splitting of both E_{2u} and E_{2g} doublets to B_{1u} and B_{2u} or B_{1g} and B_{2g} singlets of \mathbf{D}_{4h} group, respectively. Therefore, the labeling of molecular orbitals is done according to the irreducible representations of \mathbf{D}_{4h} rather than $\mathbf{D}_{\infty h}$ axial point group (see App.B). In Fig.3.2 electronic density of states (DOS) of Ir_2 is shown together with DOS projected onto orthogonalized atomic orbitals using the scheme proposed by Löwdin [55]. Reduction of $\mathbf{D}_{\infty h}$ symmetry due to population of MOs can be seen.

Symmetry also provides an information about possible hybridizations. Only molecular orbitals belonging to the same irreducible representations are allowed to hybridize. In the case of Ir_2 this implies that hybridization is allowed between $5d_{z^2}$, $6s$ and $6p_z$ as well as $5d_{xz}$, $5d_{yz}$, $6p_x$ and $6p_y$ AOs from the same atom. From Fig.3.2 it is clear that only the first type

of hybridization is realized. Moreover, contribution of $6p_z$ orbital in the electronic spectrum is appreciable only at higher energies while in the lower part mainly $6s$ and $5d_{z^2}$ orbitals are mixed. Two σ bonds are formed, one strong (lowest A_{1g} orbital) and the other weaker (higher A_{1g}). In addition to the σ bonding there is also an interaction between $5d$ orbitals from the two atoms forming π and δ bonds. This type of interaction is responsible for creating bonding E_u (π bond) doublet and two B_{1g} and B_{2g} singlets (δ bonds) as well as the corresponding antibonding E_g , B_{2u} and B_{1u} orbitals. If the simplest possible definition of the bond order is adopted:

$$B.O. = \frac{\text{number of bonding electrons} - \text{number of antibonding electrons}}{2}, \quad (3.1)$$

then there is a triple bond connecting two Ir atoms.

3.3 Ir_n ($n = 3, \dots, 8$) Clusters


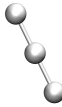
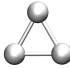
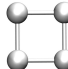
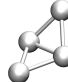

Free (gas-phase) iridium clusters were not extensively studied in the past, both experimentally and theoretically. While there are no experimental studies of the gas-phase as well as Ir clusters embedded in the rare gas matrices, several theoretical papers exist in literature. As already mentioned in the previous section only one systematic study on Ir_n ($n = 2, \dots, 64$) is published up to now [64]. The authors use method similar to that used in this work (PW91 and USPP). Two other more comprehensive studies of small Ir clusters also exist. They treat Ir_n clusters with $n = 4, 8, 9, 12, 13$ [65] or $n = 4, 6, 8, 10$ [66]. While the former is a comparative study of the properties of Ru, Rh, Pd, Ir and Pt clusters performed by the same authors as of reference [64], results in the latter are obtained with the Hartree-Fock method [67].


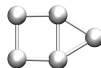

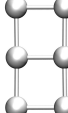

Results for Ir_n ($n = 2, \dots, 8$) clusters, obtained in this work, are presented in Tab.3.1. Properties of the most stable isomers (with the lowest total energy) are presented together with the properties of their low-energy counterparts. For Ir_4 and Ir_6 , except the data for the most stable structure and its closest isomer, the results for tetrahedral and octahedral structures, which are found in experiments treating supported Ir_4 and Ir_6 clusters [118, 119], are also given. Moreover, for Ir_7 three structures lay very close in energy and the properties of all three are presented.






Equilibrium atomic configurations are found by optimizing all degrees of freedom (including spin) of the certain number of starting configurations. For a small number of atoms there are several relevant starting configurations. However, as the number of atoms increases the number of possibilities grows immensely. Starting configurations are then chosen according to a certain group of rules (truncation from the bulk, symmetries different from the bulk, adding atoms to the stable configurations of smaller clusters,...). In the first stage, calculations are performed in the spin unrestricted fashion. Candidates for the local minima with their total energies and total S_z (z -component of the spin) are obtained in this way. Afterwards, for each geometry the spin dependence of the total energy is investigated by performing geometry optimization with the fixed spin for several lower and higher values in order to refine the group of potential configurations. The vibrational analysis is then used for final verification of the stability of these configurations.

Configurations with the lowest total energy are, of course, the most probably realized in experiments and therefore are the most important to study. However, in the opinion

Table 3.1: The most stable Ir_n ($n \leq 8$) structures are shown together with their isomers closest in energy. For Ir_4 and Ir_6 all structures between the most stable one and that found in experiments (tetrahedron and octahedron, respectively) are shown. Cohesive energies E_c , average nearest neighbor distances d_{sr} and total cluster magnetic moments per atom m are presented.

n	2		3		4	
Structure						
Symmetry	$\mathbf{D}_{\infty h}$	$\mathbf{D}_{\infty h}$	\mathbf{D}_{1h}	\mathbf{D}_{4h}	\mathbf{C}_{2v}	\mathbf{T}_d
E_c (eV/atom)	2.52	3.19	3.07	3.77	3.54	3.39
d_{sr} (Å)	2.17	2.15	2.34	2.31	2.36	2.44
m (μ_B /atom)	2.00	0.33	1.00	2.00	0.50	0.00

n	5			6	
Structure					
Symmetry	\mathbf{C}_{4v}	\mathbf{C}_{2v}	\mathbf{D}_{1h}	\mathbf{D}_{2h}	\mathbf{D}_{4h}
E_c (eV/atom)	3.98	3.97	4.36	4.29	4.23
d_{sr} (Å)	2.44	2.35	2.41	2.31	2.52
m (μ_B /atom)	1.40	1.40	1.33	0.67	2.00

n	7			8	
Structure					
Symmetry	\mathbf{C}_{2v}	\mathbf{C}_{3v}	\mathbf{C}_{2v}	\mathbf{O}_h	\mathbf{D}_{2h}
E_c (eV/atom)	4.46	4.44	4.44	4.92	4.68
d_{sr} (Å)	2.48	2.45	2.41	2.34	2.43
m (μ_B /atom)	1.57	1.28	1.17	0.00	1.00

of the author of this thesis, importance of the configurations that are higher in energy is underestimated in the scientific community. Their properties are presented in the scientific publications mainly as a proof that all relevant configurations are taken into account and that the most stable one represents the true global minimum. Only in the cases where there is a discrepancy with experiments such as Ir_4 [69] or where several nearly degenerate configurations exist (like the situation with Pt_4 [77, 76]) properties of the low energy structures are discussed in more details. It is shown in this work (Chapters 4, 5 and 6) that the isomers which are as much as ~ 1.5 eV higher in energy may become relevant due to the interaction with adsorbates and/or support.

For Ir_3 the linear configuration with the total magnetic moment of $1 \mu_B$ is found to be the most stable one. It is by 0.36 eV lower in energy than the isosceles triangle which carries a

magnetic moment of $3 \mu_B$. The equilateral triangle (D_{3h} symmetry) is Jahn–Teller unstable due to a large number of electronic levels close to the Fermi energy. Differences in the Ir–Ir coordination of the two isomers are reflected in the different average interatomic distance which is by 0.19 \AA shorter in the case of linear isomer. Results for the triangle agree very well with those reported in reference [64] ($E_c = 3.03 \text{ eV}$ and $m = 1.00 \mu_B$). However, the authors do not present at all, properties of the linear Ir_3 . On the other hand, the accord is not that good with the results obtained with the relativistic configuration interaction (RCI) method [63]. The authors treated only triangular Ir_3 and found, in the absence of spin–orbit (SO) coupling, nearly equilateral triangle with $d_{sr} \approx 2.52 \text{ \AA}$ as the ground state with the magnetic moment of $5 \mu_B$. The effect of SO coupling is mixing the $m = 5 \mu_B$ ground state with $m = 7 \mu_B$ first excited state which results in increasing d_{sr} to $\sim 2.7 \text{ \AA}$. However, the average RCI Ir–Ir distance in triangular Ir_3 is close to the experimental values of the Ir–Ir nearest neighbor distance in bulk iridium and in $\text{Ir}_4(\text{CO})_{12}$ molecule (2.72 and 2.69 \AA , respectively) where iridium atoms are highly coordinated.

Results for Ir_4 are discussed in details in Sec.3.4. For Ir_5 two nearly degenerate isomers are found well separated in energy from all the others (about 0.9 eV). Both structures are formed by adding one Ir atom to the square configurations. The square pyramid carrying magnetic moment of $7 \mu_B$ is the lowest in energy, only by 0.05 eV more stable than planar configuration where the added Ir atom bridges one side of the square. The latter structure is also magnetic and carries the same magnetic moment. The average Ir–Ir first neighbor distance is longer in the case of pyramid by 0.09 \AA . These results agree also very well with those from reference [64].

Total energy of the trigonal prism, the most stable Ir_6 isomer, is by 0.42 and 0.78 eV lower than that of planar and octahedral isomers, respectively. All three structures are magnetic with the total cluster magnetic moments of 8 (prism), 4 (planar) and $12 \mu_B$ (octahedral). Both perfectly symmetric prism and octahedron are Jahn–Teller (JT) unstable and lower their symmetries to D_{1h} and D_{4h} , respectively. Energies of JT deformations are about $\sim 0.1 \text{ eV}$ in both cases. Planar isomer has the lowest average Ir–Ir first shell coordination number and hence, the shortest average Ir–Ir first shell distance (2.31 \AA). As the coordination number grows from 3 (prism) to 4 (octahedral structure) the Ir–Ir distance increases from 2.41 to 2.52 \AA , respectively.

All theoretical studies treating the gas–phase Ir_6 [64, 66, 68] agree that the JT deformed trigonal prism is the most stable structure. However, details of the electronic ground state and the energy difference to the octahedral isomer are different. In reference [64] the prism has 8 unpaired electrons and is by 0.72 and 1.44 eV more stable than planar and octahedral structure each carrying magnetic moments of 8 and $6 \mu_B$, respectively. On the other hand, scalar relativistic all–electron DFT calculations [68] yield the prism with the moment of $6 \mu_B$ and $d_{sr} = 2.42 \text{ \AA}$ which is by 1.06 eV more stable than octahedral isomer (trigonal antiprism). Hartree–Fock calculations [66] also yield trigonal prism as the most stable Ir_6 isomer, but the authors do not report values of total energies⁵. Furthermore, calculated Ir–Ir distances are much bigger ($\sim 2.59 \text{ \AA}$ for the prism) than those reported here. As it is already mentioned, complexity in transition metal clusters arises from the large number of low lying many–electron states and even small differences between computational approaches may give different ground states which consequently produce differences in isomer relative energies⁶.

⁵They say for Ir_6 on the fourth page, sixth line "the calculated total energies are omitted here for simplicity".

⁶Again, test calculations with norm conserving pseudopotential for iridium give difference between the

Three configurations very close in energy exist in the case of Ir₇. All three are obtained by adding one Ir atom to the Ir₆ trigonal prism. The most stable isomer is the one with C_{2v} symmetry where the added Ir atom "sits" on one side of the prism while at the other two it is positioned either on top of the base (C_{3v}) or bridges one edge of the prism (C_{2v}). The lowest energy structure is only by 0.14 and 0.15 eV more stable than the other two (following the same order like in Tab.3.1). Each isomer carries a nonzero magnetic moment which decreases from 11 μ_B for the most stable structure to 9 and 7 μ_B for the less stable C_{3v} and C_{2v} configurations, respectively. The accord with the results from reference [64] is as good as for Ir₆. The most stable structure is the same, with the same magnetic moment, but the reported cohesive energy is by 0.05 eV higher. The second lowest structure is the C_{2v} one (with the same magnetization), while the isomer with C_{3v} symmetry is missing. Reported cohesive energy for that structure is only 0.01 eV higher than the value reported here which leads to considerably different relative energy of 0.42 eV.

Perfect cubic structure is by far the most stable Ir₈ configuration. The energy gain compared to eight isolated Ir atoms is 4.92 eV/atom, by 0.24 eV/atom higher than for the nearest (in energy) double-prism configuration. The difference between cohesive energies of the two isomers is similar to the Ir₄ case and bigger than for all the other clusters sizes. Hence, it implies that Ir prefers using the square geometry as the building block when forming small clusters. This is the point where all authors agree [64, 65, 68, 69]. The electronic ground state of the cube is nonmagnetic while the double-prism structure has eight unpaired electrons. Great stability of the cubic structure is also reflected by the drop of the average nearest neighbor Ir-Ir distance from 2.48 Å in Ir₇ to 2.34 Å. Results for Ir₈ agree well with those from references [64, 65].

In Fig.3.3 results from Tab.3.1 are represented graphically. Cohesive energy, average nearest neighbor Ir-Ir distance and magnetic moment per atom of Ir_n ($n = 2, \dots, 8$) are shown as a function of the cluster size. The dependence of the HOMO-LUMO gap is not presented here (at variance to other studies of the gas-phase clusters where it is usually done) since it is known that DFT methods underestimate this quantity (see Ref.[19]). It cannot be expected that the error is similar for all cluster sizes since the HOMO-LUMO gap depends strongly on the cluster geometry. Therefore, calculated trends in the HOMO-LUMO gap are not considered as reliable.

Cohesive energy grows monotonically with the cluster size. In reference [64] similar trend up to the eight atom cluster is reported. The authors also investigated bigger clusters and found much slower growth of E_c when going from Ir₈ to Ir₉, from Ir₁₀ to Ir₁₁ and Ir₁₂ to Ir₁₃ which they attributed to the increased stability of the 8, 10 and 12 atom clusters having the simple cubic structure as the building block. They also found that up to 48 atoms iridium clusters prefer simple cubic instead of fcc arrangement which is much more than for other transition metals (only Ru shows similar behavior [82] while for Pt transition occurs at the size of 13 atoms [64]). In addition to the trend for the most stable isomers, it is reported here that the dependence of E_c is similar also for structures nearest in energy. Moreover, as it is shown in Fig.3.3, low energy structures are quite close in E_c , except for Ir₄ and Ir₈ where strong preference towards square and cubic structures is found. In Sec.3.4 it is proved on Ir₄ clusters that the strong preference towards cubic-like structures is mainly due to very favorable d - s hybridization in iridium clusters.

However, results from EXAFS [133] measurements done on the MgO, TiO₂ and Al₂O₃

prism and octahedral structure of only 0.41 eV.

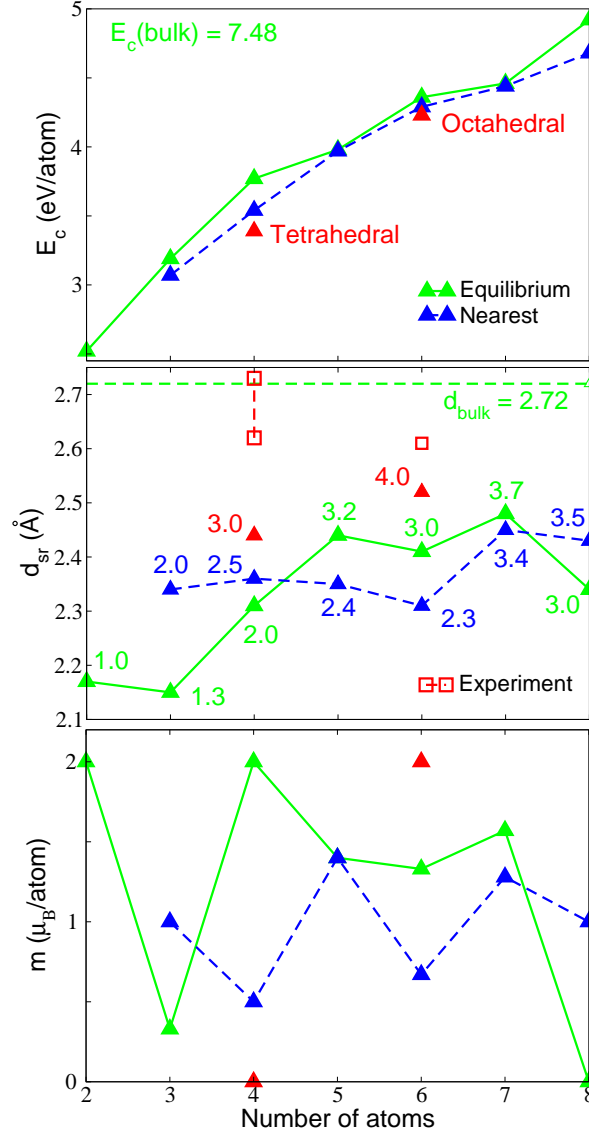


Figure 3.3: Properties of Ir_n ($n = 2, \dots, 8$) clusters: cohesive energy E_c , average nearest neighbor distance d_{sr} and magnetic moment per atom m , as a function of the cluster size. Data for the most stable isomers are presented as well as for those which are nearest in energy. For Ir_4 and Ir_6 properties of the tetrahedral and octahedral geometries, found in experiments for the supported clusters, together with experimental d_{sr} are also given. Numbers in the middle graph denote average first shell Ir–Ir coordination numbers.

supported Ir_4 and Ir_6 clusters [118, 119, 126] do not correspond to the the theoretically predicted stability. From the measured first shell Ir–Ir coordination number (CN) the authors concluded that, independently on the support, Ir_4 is tetrahedral while Ir_6 adopts octahedral shape. It also follows from the measured interatomic distances (check discussion below) that these discrepancies between theory and experiment may be attributed to interactions of the clusters with support and/or adsorbed atomic or molecular species. It is shown in this thesis that, indeed, the interaction with oxygen vacancies on $\text{MgO}(100)$ surface (Sec.5.5) or clean $\text{TiO}_2(110)$ (Sec.5.6) surface as well as with C adatom or CO molecules (Chapters 4 and 6) can

considerably affect relative energies between Ir₄ isomers making tetrahedral structure either degenerate or more stable than the square.

The average nearest neighbor Ir–Ir distance (d_{sr}) does not show monotonic behavior. The overall trend for the most stable isomers is growing with the bulk value as the upper limit, but in the cases of Ir₃, Ir₆ and Ir₈, d_{sr} decreases. By analyzing correlations with the average coordination of Ir atoms in the clusters it can be concluded that d_{sr} depends more on the average first shell Ir–Ir CN (shown in Fig.3.3) than on the cluster size. For the most stable Ir₆ and Ir₈ structures CN decreases from the values it has for the corresponding smaller clusters which is followed by the drop in d_{sr} . Only in the case of Ir₃ the d_{sr} shows opposite behavior. While first shell CN increases from 1 (dimer) to 1.3 (linear trimer) the average distance decreases from 2.17 to 2.15 Å. This is another manifestation of the strong d – s hybridization which favors linear Ir₃ configuration more than the triangle⁷. Particularly strong Ir–Ir bonds are formed in linear Ir₃ with better screening of the nuclei enabling shorter interatomic distances. However, the dependence of d_{sr} on the first shell CN is supported by the fact that for a fixed number of atoms d_{sr} is always the shortest for the isomer having smallest CN which is true also for Ir₃.

Experimental values of d_{sr} for MgO, TiO₂ and Al₂O₃ supported Ir₄ and Ir₆ clusters [118, 119, 126] (Fig.3.3) lay in the range 2.62–2.73 and 2.61–2.62 Å for Ir₄ and Ir₆, respectively. They are noticeably longer than the calculated values of the corresponding gas-phase structures and it follows from the experimental results that do not depend appreciably on the type of the support. These values are close to the bulk nearest neighbor distance of 2.72 Å [52, 53] and $d_{sr} = 2.69$ Å in Ir₄(CO)₁₂ molecule [16]. In these systems the Ir atoms are highly coordinated suggesting that interaction of Ir₄ and Ir₆ clusters with their environment (support and/or ligands) is responsible for the differences between theoretically predicted isomer stability and experimental results.

Magnetization of small Ir clusters also does not show monotonic behavior. It is, even not possible to anticipate the decreasing trend towards nonmagnetic bulk fcc iridium from the values for Ir_{*n*} clusters with $n \leq 8$. This is not surprising since the magnetic moment is highly sensitive to geometry. In reference [64] the authors show that starting from 9 atoms, magnetic moment is lower than 0.5 μ_B /atom for all studied clusters. However, since iridium has odd atomic number the nonmagnetic solution is not possible for clusters with odd number of atoms and magnetic moment shows oscillatory behavior also for big n values.

Bonding mechanism in Ir_{*n*} ($n \leq 8$) is similar to that in Ir₂ that is explained in Sec.3.2. Molecular orbitals of the clusters are either of purely d or mixed dsp character. The level of dsp hybridization strongly depends on the cluster geometry and is different for different isomers. This issue is elaborated in details on the example of Ir₄ clusters which are the subject of the following chapter.

3.4 The Case of Ir₄

Gas-phase Ir₄ clusters have been studied up to now only theoretically [64, 65, 69, 66]. Experimental studies treat only supported species [12, 118, 126]. Iridium tetramers are prepared

⁷Three s orbitals with one electron per orbital (three H atoms) form linear trimer rather than triangular. This is due to the same number of bonding molecular orbitals that are formed in two structures (there is exactly one) and more destabilizing occupied antibonding orbital in the case of triangle. Look in Sec.3.4.1 for a more detailed discussion of this issue.

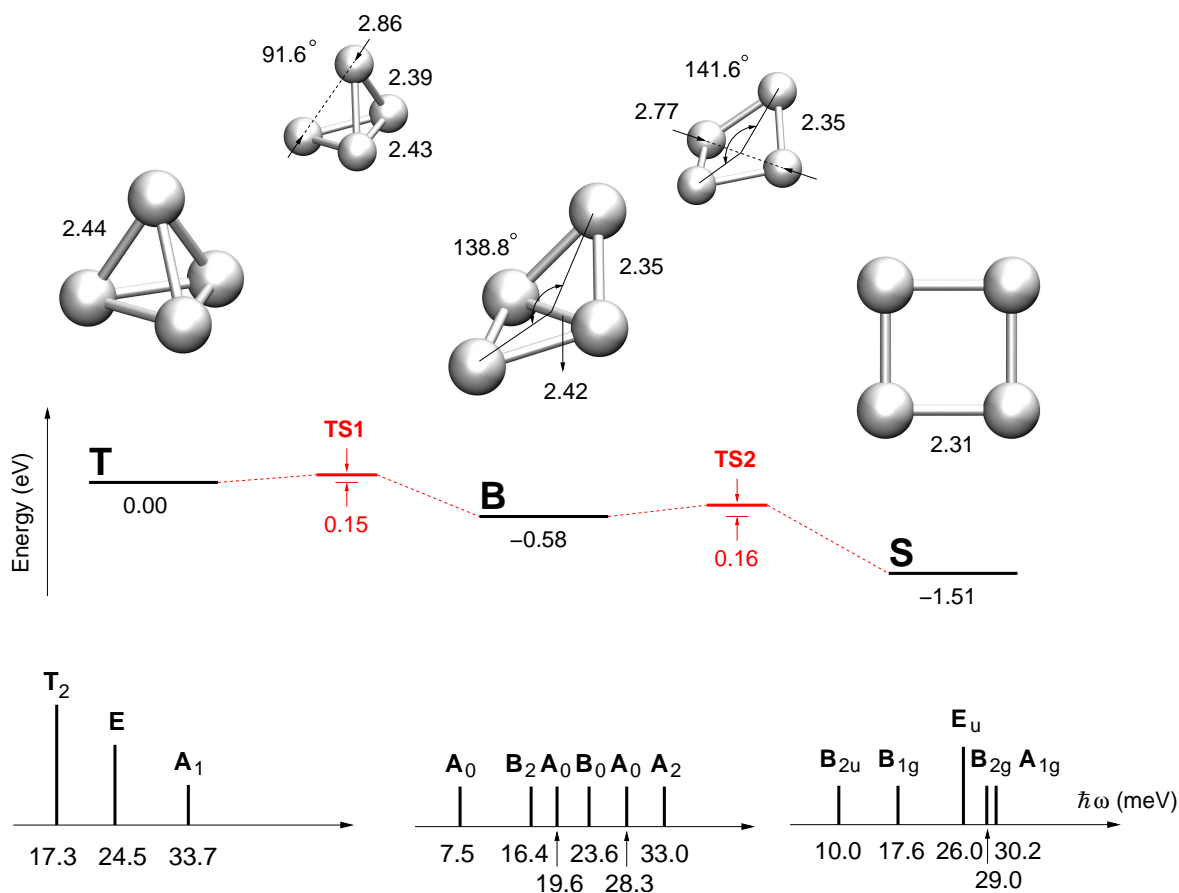


Figure 3.4: Three Ir₄ isomers (**T**, **B** and **S**) are shown together with the configurations of two transition states (TS1 and TS2) for structural transformation from **T** to **B** and **B** to **S**. Numbers beside each structure represent the Ir-Ir distances (in Å) or the butterfly bending angles. Relative energies (with respect to **T**) together with energy barriers are also displayed as well as vibrational spectra of the three stable structures. Length of the line representing certain vibrational frequency is proportional to the degeneracy of the corresponding mode. Vibrational modes are labeled according to their symmetry properties (see Tab.3.1 for the symmetries of Ir₄ clusters and App.B for labeling of their irreducible representations).

experimentally by decarbonylating Ir₄(CO)₁₂ complexes which are previously deposited over an oxide substrate. It follows from the EXAFS measurements (see reference [119] and the references therein) that, after the treatment, tetrahedral metal frame of the carbonyl molecules remains intact.

On the other hand, authors of theoretical studies on Ir₄ [64, 65, 69] agree that the most stable Ir₄ isomer is perfect square (**S**) followed by butterfly structure (rhombus which is bent around its shorter diagonal further denoted as **B**) and tetrahedron (**T**). All mentioned studies are done with DFT methods. Only one theoretical Hartree-Fock study of Ir₄ exists [66] whose authors also report that **B** isomer is more stable than **T**, but they do not present at all results for **S** structure.

Results for the gas-phase Ir₄ obtained in this work are presented in Tab.3.1 and Fig.3.4. Three relevant configurations (**T**, **B** and **S**) are found following the procedure for searching stable configurations explained in Sec.3.3. Namely, structures which are not stable with

respect to the magnetic moment variations (to the nearest possible values) are not considered as local minima.

It is confirmed here that **S** structure with eight unpaired electrons is the most stable form of the gas-phase Ir_4 . It has cohesive energy 3.77 eV/atom and nearest neighbor distance 2.31 Å. The method that is used in this work for modeling iridium clusters (see Chapters 2 and 3) yields nondegenerate electronic ground state of **S** structure and hence, there is no Jahn–Teller distortion. Stability of this structure is also confirmed by the vibrational analysis (see Fig.3.4). Six normal modes lay in the range 10.0–30.2 meV. Highest energy is the so called "breathing" mode (all interatomic distances increase) while the lowest in energy is antisymmetric out-of-plane mode which bends **S** structure towards **B** configuration.

The first less stable equilibrium configuration is **B** with the total cluster magnetic moment of $2 \mu_B$. It is by 0.93 eV less stable than **S** structure. Its average nearest neighbor Ir–Ir distance is 2.36 Å while the distance between two wing tip Ir atoms is 3.78 Å. The bending angle (angle between "wings" of the butterfly) is 138.8° . Range of frequencies of the vibrational modes is somewhat bigger compared to **S** isomer. The breathing mode (33.0 meV) is the highest in energy as well, but lays ~ 3 meV higher, while the bending mode (7.5 meV) is also lowest in energy and lays ~ 3 meV lower than the corresponding mode of **S** structure.

Authors of reference [64] report rhombus (butterfly with zero bending angle and D_{2h} symmetry) carrying magnetic moment of $6 \mu_B$ as the only structure between **T** and **S**. It is found in this work that the rhombic configuration with 6 unpaired electrons is indeed one of the candidates for the local minima, but it is higher in energy than **B** isomer by 0.18 eV and unstable with respect to the change of magnetic moment. Increasing magnetic moment to $8 \mu_B$ results in structural relaxations which transform rhombus into **S** configuration.

The least stable Ir_4 isomer whose properties are presented in this thesis is **T** structure, with the total energy by 0.58 and 1.51 eV higher than that of **B** and **S**, respectively. Its nondegenerate electronic ground state is also nonmagnetic. Of all three structures **T** isomer has the longest nearest neighbor Ir–Ir distance 2.44 Å. As discussed in Sec.3.3 this follows from the largest first shell Ir–Ir coordination number. Due to symmetry reasons (degeneracies) its low energy modes are shifted to higher frequencies compared to corresponding low energy sectors of the **B** and **S** vibrational spectra. The lowest frequency in the spectrum of **T** isomer is 17.3 meV and is triply degenerate. On the other hand frequency of the breathing mode, which is totally symmetric and therefore nondegenerate, remains close (by 0.7 meV higher) to frequency of the corresponding mode of **B** isomer.

Although, it is not possible to make direct comparisons between theoretical results for the gas-phase clusters and experimental ones for the supported species, the fact that **T** structure, that is by 1.51 eV less stable than **S**, is observed in experiments requires a closer inspection of the potential energy landscape around and between these configurations. It might occur that due to high energy barriers for structural transformations between these three isomers the **S** structure becomes kinetically inaccessible. Therefore, the pathways and energy barriers for structural transitions are investigated. Main tool in these kind of investigations is the nudged elastic band (NEB) method and its climbing image (CINEB) version. They are both described in Sec.2.2.5.

Results of the CINEB calculations are also presented in Fig.3.4. Minimal energy paths (MEP) for the transformations are found and the saddle points corresponding to the transition states located. It turns out that the MEP for transformation between the **T** and **S** structures passes through the intermediate **B** configuration. Therefore, two transition states exist along this pathway, one for the transition from **T** to **B** (TS1) and the second one from **B** to **S** (TS2).

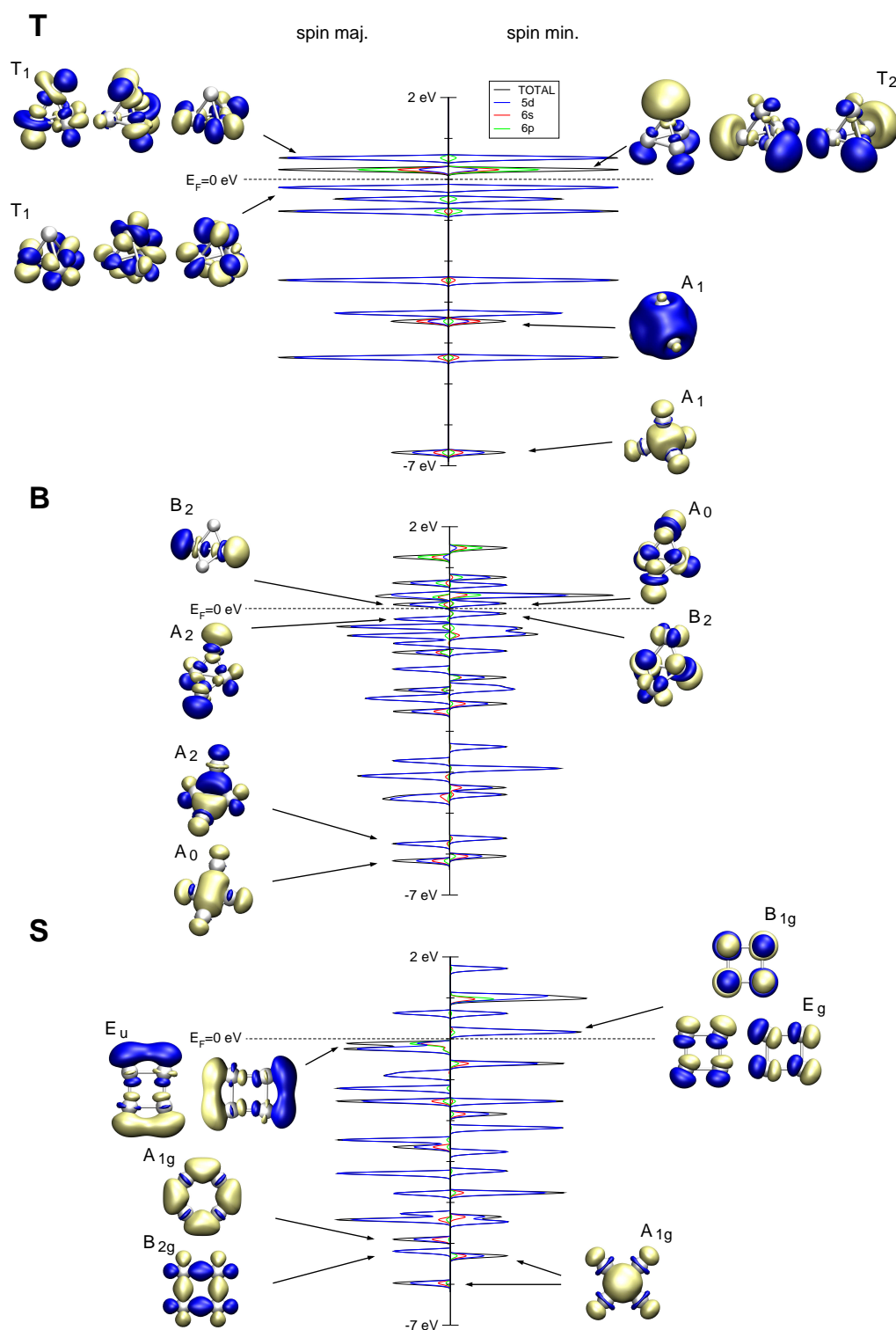


Figure 3.5: Total and projected DOS of the three Ir_4 isomers (**T**, **B** and **S**) are shown together with low lying and molecular orbitals (MO) around the Fermi energy. Orbitals are labeled according to the symmetry properties with respect to the corresponding symmetry group.

Energies of these two transition states relative to the initial configuration of the corresponding path (energy barrier for the process) are 0.15 and 0.16 eV for TS1 and TS2, respectively. These barriers are very low and after applying Eq.2.19 at room temperature, even using the lowest frequency vibrational modes of the two initial structures as the prefactors ($\sim 10^{12}$ Hz), the rate constants for these two transformations are of the order of 10^{10} Hz. Of course, if the system has enough energy to overcome the first it will have enough energy to pass the second transition state, too. The conclusion is that, at room temperature, gas-phase Ir_4 clusters quickly adopt **S** geometry.

Atomic structures of the two transition states are also shown in Fig.3.4. In both cases one Ir–Ir bond of the corresponding initial configuration is considerably elongated. By inspecting electronic densities of TS1 and TS2 it can be concluded (on the basis of Bader analysis [74] for example) that those Ir–Ir bonds are broken. Therefore, the two transition states are located in the points (in the configurational space) where one Ir–Ir bond of the corresponding initial configuration is broken enabling transition in the desired direction, while the other bonds are not strengthen enough yet. Pushing the system from both transition states in any of the two directions which lower its energy would result either in reestablishing the broken bond (going back to the initial state) or strengthening other bonds and stabilizing the system in the corresponding final configuration. Very small energy needed for breaking one bond in **T** structure is a consequence of the symmetry breaking which enables more efficient hybridization of atomic orbitals. Similar arguments can be used in explaining the transition from **B** to **S**.

In Fig.3.5 total and DOS projected onto orthogonalized (Löwdin [55]) atomic orbitals are shown for the three Ir_4 isomers (**T**, **B** and **S**). Spectra are broaden using Gaussians with width of ~ 0.07 eV (0.005 Ry). Low energy as well as molecular orbitals (MO) near the Fermi energy are also presented. In all three cases MOs are formed either purely of atomic $5d$ orbitals or by dsp hybridization. Calculated Löwdin charges (integrated projected DOS) on each atom are distributed like $5d^{8.03}6s^{0.59}6p^{0.35}$ for **T** structure, $5d^{7.82}6s^{0.75}6p^{0.40}$ for **B**⁸ and $5d^{7.62}6s^{0.86}6p^{0.48}$ for **S** isomer. The contribution of $6s$ and $6p$ AOs grows from **T** to **S** indicating bigger hybridization of atomic orbitals. The projected DOS shows that in the low energy part of all three electronic spectra the d – s hybridization dominates, while the contribution of $6p$ orbitals becomes appreciable at higher energies. This is due to the big energy difference between $5d$, $6s$ and $6p$ orbitals in Ir atom (see Sec.3.1). Therefore, the following discussion is restricted only to the d – s type of hybridization.

Different level of d – s hybridization in these three structures is a consequence of different cluster symmetries. Namely, being totally symmetric with respect to 3D rotations, s orbitals can form exactly one strongly bonding MO in any atomic configuration (this is a general conclusion and does not depend on the symmetry or number of atoms). All other linear combinations of s orbitals from different atoms are either nonbonding or antibonding. Good example is purely s –bonded H_4 molecule whose properties are presented in Sec.3.4.1 (the following one). As it is shown in Fig.3.8 in the case of tetrahedral H_4 all MOs higher in energy have antibonding character. On the other hand, in **B** and **S** configurations, strongly antibonding combinations are pushed to higher energies and remain unoccupied. Therefore, the binding in these two structures is considerably stronger. However, if the number of electrons is such that only bonding MO is filled (0.5 electrons/atom), relative energies change dramatically (H_4^{2+} in Tab.3.2). Therefore, H_4 in **T** geometry favors population of s orbitals

⁸For **B** structure average population of two symmetry nonequivalent Ir atoms is presented.

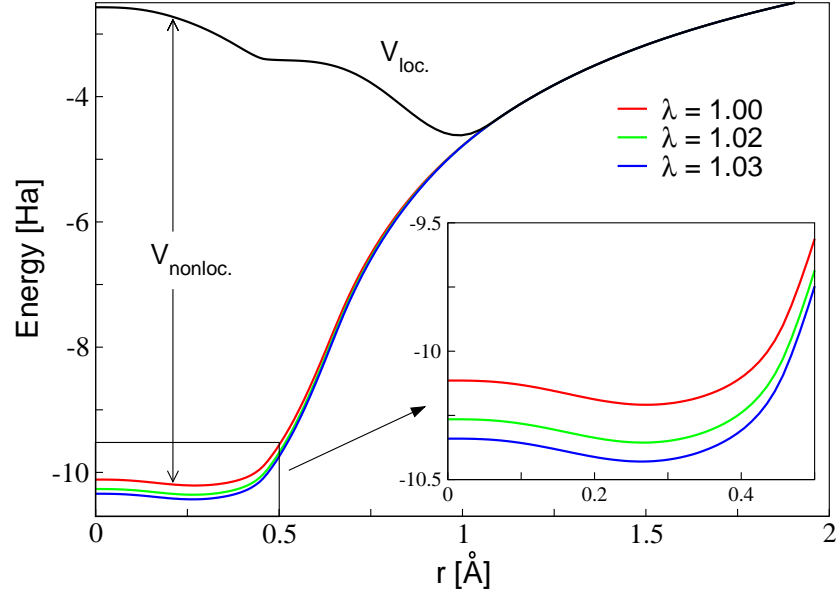


Figure 3.6: Modified iridium d pseudopotential is shown for various λ values (see Eq.3.3). The local s component of the pseudopotential is also presented.

of 0.5 electrons/atom, while for the other two configurations it is more favorable (relative to **T**) to have bigger population of s orbitals.

The same reasoning can also be applied to Ir_4 . In **T** geometry the binding would be enhanced if the d -like MOs hybridize only with the strongly bonding s -like linear combination. Since the strongly bonding s -like orbital is totally symmetric, only MOs of the same symmetry can hybridize and the only possibility is the bonding combination of d_{z^2} AOs (see App.B). In **B** and **S** configurations number of totally symmetric linear combinations of d AOs is bigger (three A_1 and two A_{1g} linear combinations in **B** and **S** structures, respectively). Moreover, participation of other s -like MOs (nonbonding or weakly antibonding) could also act stabilizing.

To extract the influence of d orbitals on the atomic structure of Ir_4 (and more general X_4 molecules) in similar way is more difficult. The system whose properties are governed only by d orbitals does not exist and the analysis based purely on the symmetry and population of d orbitals (without the real system as an example) would not lead to unambiguous conclusions. Therefore, another way of investigating the influence of d - s hybridization on atomic structure in Ir_4 clusters is followed here. The idea is to modify iridium pseudopotential in such a way to decrease the level of d - s hybridization. This can be done by making the d component of iridium pseudopotential more attractive which would shift the energy of d electrons deeper in the spectrum. The following transformation is applied

$$V^{l=2} = V_{loc.} + V_{nonloc.}^{l=2}, \quad (3.2)$$

$$V_{nonloc.}^{l=2} \longrightarrow \lambda V_{nonloc.}^{l=2}, \quad (3.3)$$

in which the nonlocal d component $V_{nonloc.}^{l=2}$ of the pseudopotential is multiplied by a constant factor λ . In order to avoid complications due to the augmentation charges, the normconserving pseudopotential (NCP) in the Troulier–Martins form [46] is used for this purpose. It is

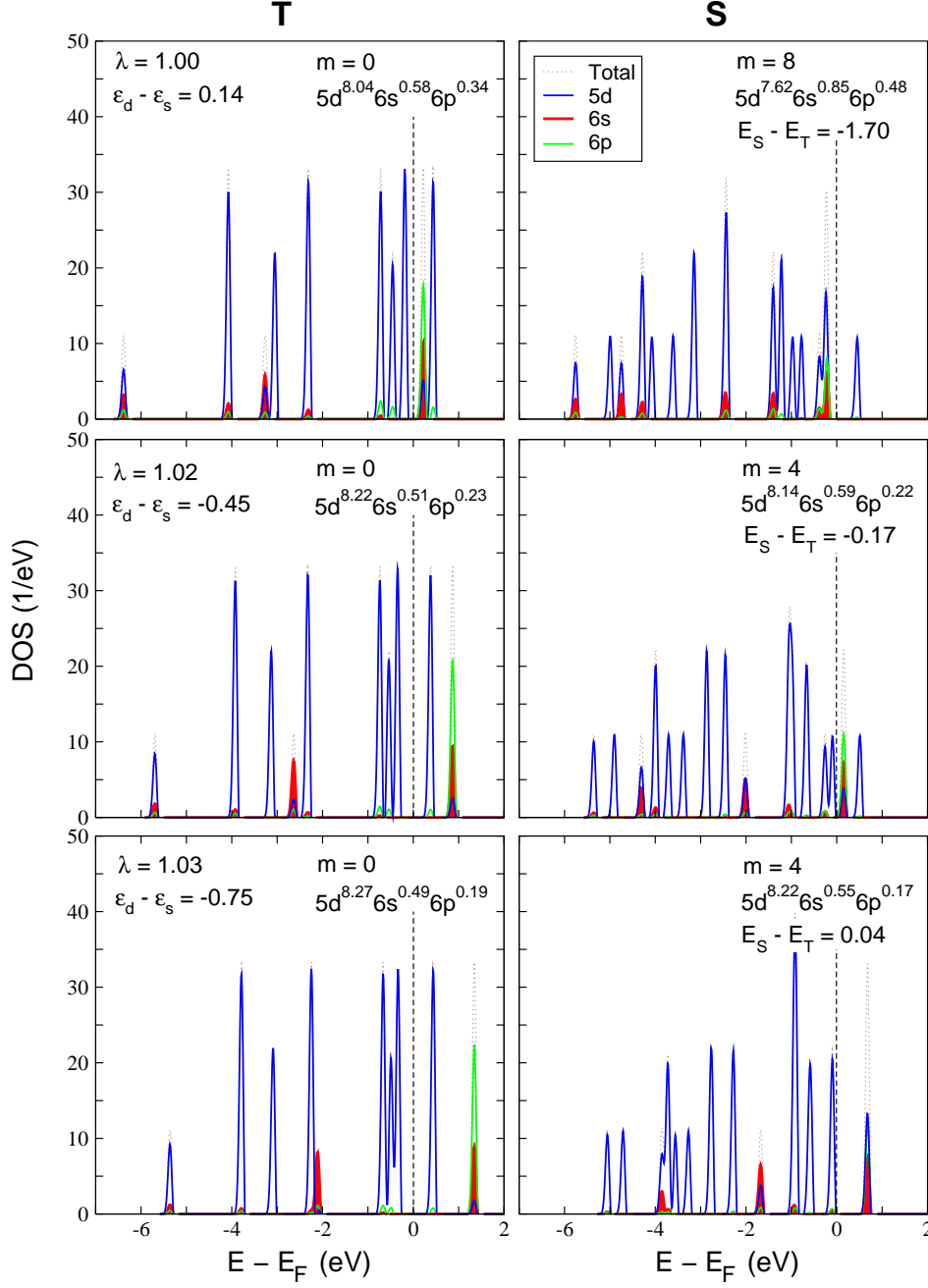


Figure 3.7: Total and projected spin majority DOS of **T** and **S** Ir₄ isomers calculated using modified norm-conserving PP (see Eq.3.3) are shown. Numbers denote values of modifying parameter λ , energy difference $\epsilon_d - \epsilon_s$ (in eV) between the KS eigenvalues of d and s electronic states in Ir atom calculated in the spherical screening approximation, total cluster magnetic moment m , Löwdin charges [55] of each iridium atom and the total energy difference (in eV) of the two isomers.

constructed with the **fhi98PP** pseudopotential program [47]. Effects of the modification (Eq.3.3) on the Ir pseudopotential are shown in Fig.3.6.

Three NCPPs are constructed in this way ($\lambda = 1.00, 1.02, 1.03$). Each of them yields different relative d - s energies in iridium atom and hence, different level of d - s hybridization in Ir_4 clusters as shown in Fig.3.7. For the sake of simplicity results for only **T** and **S** isomers are presented. Notice that the true iridium NCPP ($\lambda = 1.00$) gives different relative energy of **T** and **S** structures⁹. However, calculated population of different atomic orbitals is very close to that obtained by USPP. Results obtained using modified NCPPs indicate that in Ir_4 the level of d - s hybridization is responsible for the energy ordering of the three isomers. As the hybridization becomes less favorable and the population of s orbitals approaches 0.5 electrons/atom in both configurations, situation changes and the energy preference of 1.7 eV towards **S** isomer decreases to very low or even negative values.

3.4.1 Stability of X_4 isomers ($\text{X}=\text{H}, \text{Au}, \text{Pt}, \text{Ir}, \text{Rh}, \text{Co}, \text{Ru}$)

Subject of this section is the influence of d - s hybridization on the relative stability of the three X_4 isomers (**T**, **B** and **S**), where X is a transition metal. The most stable tetramer geometry for given transition metal is not necessarily among these three structures *i.e.* for Au_4 the most stable isomer according to reference [76] is a planar structure, triangle with the fourth atom bonded solely to one the other three. Reason for the restriction to only these three isomers is their relevance for Ir_4 which is subject of this thesis. Since bonding in late transition metal clusters is very complicated (they are in general multiparameter systems with a large number of parameters), simpler situation of purely s -bonded H_4 molecule and the relative stability of different H_4 isomers could give a better insight into the influence of s atomic orbitals on bonding in transition metal tetramers.

Results for the three H_4 isomers (**T**, **B** and **S**), both neutral and doubly ionized¹⁰, are presented in Fig.3.8 and Tab.3.2. In the neutral case, the least stable H_4 isomer is **T** structure that is by 2.72 eV higher in energy than **S** and by 4.36 eV than flat **B** configuration with D_{2h} symmetry (rhombus). The energy ordering of the three isomers can be understood from the symmetry analysis. Namely, atomic s orbitals are totally symmetric with respect to 3D rotations and as such they can form only one strongly bonding molecular orbital whatever is the symmetry and the number of atoms in a cluster¹¹. This MO is the lowest in energy and doubly occupied (see Fig.3.8) in all three cases. All other linear combinations of s orbitals have either weak or strong antibonding character.

In **T** configuration all Ir-Ir distances are equivalent and, except the totally symmetric MO, only strong antibonding combinations of s orbitals can be formed. In **B** and **S** structures due to the existence of different Ir-Ir coordination shells, linear combinations of s orbitals with less pronounced antibonding character can be constructed. After populating these orbitals,

⁹This is due to differences between USPP and NCPP in the description of atomic core in the absence of spherical screening approximation which is used for construction of both pseudopotentials. Small differences will be present in their Hartree potentials also outside the core. The NCPP atomic core is slightly more repulsive leading to somewhat different cluster relative energies.

¹⁰Charged systems are simulated using the Makov-Payne [75] corrections to remove spurious electrostatic interaction between supercells.

¹¹In fact, they can form more than one if there are nonequivalent (by symmetry) atoms in a cluster. However, those orbitals will all be totally symmetric with respect to the cluster's symmetry group and consequently they will hybridize forming only one strongly bonding MO spreading over all atoms in a cluster. This situation occurs in **B** configuration.

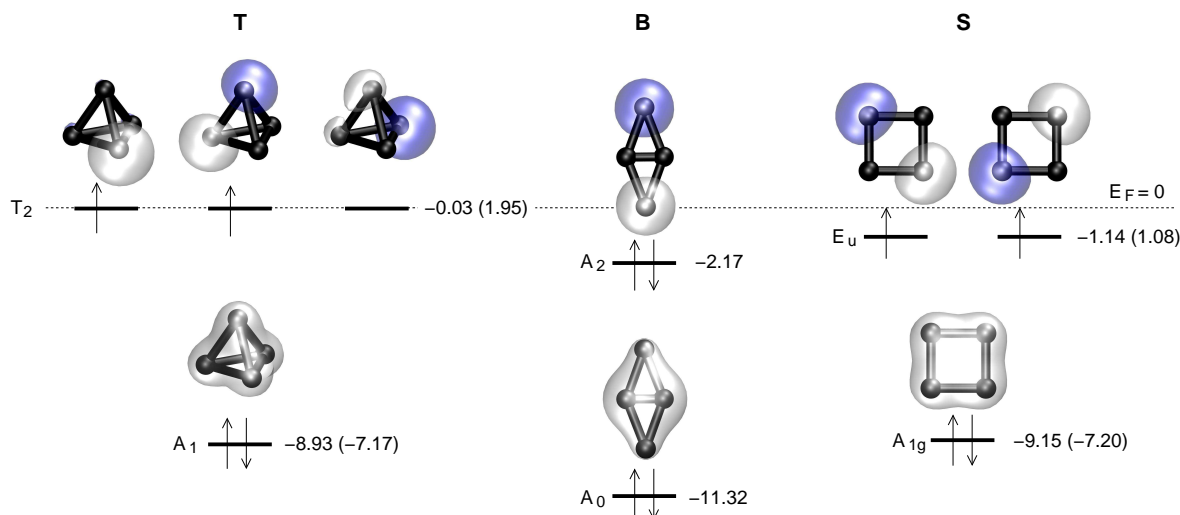


Figure 3.8: Occupied parts of the spectra of three H_4 isomers (**T**, **B** and **S**) are presented together with the spin majority (minority) KS eigenvalues (in eV). Spectra are aligned on the same Fermi energy. Molecular orbitals, labelled according to their symmetry properties, are also shown.

T configuration becomes much more destabilized than the other two. On the other hand, if two electrons are removed from the clusters (H_4^{2+}), the remaining two electrons occupy only bonding MO in a singlet spin state and the relative energies of the three isomers are completely different. The **B** structure remains the most stable, but now only by 0.34 eV lower in energy than **T**, while **S** becomes the least stable structure that is by 0.82 eV higher than **T**. However, as soon as the electrons begin to fill antibonding MOs energies change in favor of the two planar structures. When the number of electrons is $\sim 0.6/\text{atom}$ **T** and **S** become degenerate and about 1.4 eV less stable than **B** configuration. This result is useful in understanding the influence that s atomic orbitals have on relative energies of transition metal tetramers.

Beside iridium, four other platinum group transition metals (Pt, Pd, Rh and Ru) plus Co and Au are examined (see Fig.3.9). Their tetramers are simulated with the same theoretical approach used for Ir clusters (Chapter 3). The energy differences between the three cluster geometries (**T**, **B** and **S**) as well as the population of their AOs are investigated. Results obtained in this work agree reasonably well with already published theoretical results on tetramers of Au [76], Pt [76, 77], Pd [78, 79], Rh [80, 81], Ru [82] and Co [84, 85]. Similarly to iridium, differences exist when relative energies of different isomers are compared.

As expected, energy ordering of the three Au_4 isomers is the same as in H_4 . Symmetries of the three isomers are the same as in H_4 as well as their magnetic moments. Qualitative similarities to hydrogen come from the fact that Au atoms has completely filled $5d$ shell and only one electron occupying the $6s$ AO. However, the energy differences between isomers are much smaller and there is also some depopulation of both $5d$ and $6s$ and population of $6p$ orbitals. Moving one place left in the periodic table to Pt_4 , isomer relative energies become very small. The d shell in Pt atom has one electron less than Au and influence of d orbitals on binding is much bigger. Magnetic moments of the three structures are different (2, 4 and $6 \mu_B$ for **T**, **B** and **S**, respectively) and the symmetry of **B** isomer is changed. Flat rhombic structure bends (angle 158.9°) and reduces its symmetry to C_{2v} . The population of atomic

	27 Co $3d^8 4s^1$	
44 Ru $4d^7 5s^1$	45 Rh $4d^8 5s^1$	46 Pd $4d^{10} 5s^0$
	77 Ir $5d^7 6s^2$	78 Pt $5d^9 6s^1$
		79 Au $5d^{10} 6s^1$

Figure 3.9: Elements whose tetramers are used for the analysis. Their symbols, atomic numbers and calculated valence populations are shown.

Table 3.2: Properties of the three X_4 isomers (**T**, **B** and **S**). The clusters' energies relative to **T** configuration $E - E_T$ (in eV) and Löwdin population LP of the valence atomic orbitals are presented. **B** configuration is not a stable structure of Pd_4 and therefore no results are presented.

system	T		B		S	
	$E - E_T$	LP	$E - E_T$	LP	$E - E_T$	LP
H_4	0.00	$s^{0.97}$	-4.36	$s^{0.97}$	-2.72	$s^{0.97}$
H_4^{2+}	0.00	$s^{0.45}$	-0.34	$s^{0.45}$	0.82	$s^{0.45}$
Au_4	0.00	$d^{9.75} s^{0.81} p^{0.38}$	-1.31	$d^{9.77} s^{0.86} p^{0.32}$	-0.60	$d^{9.74} s^{0.88} p^{0.32}$
Pt_4	0.00	$d^{9.13} s^{0.57} p^{0.28}$	-0.08	$d^{8.89} s^{0.74} p^{0.35}$	0.12	$d^{8.73} s^{0.84} p^{0.40}$
Ir_4	0.00	$d^{8.04} s^{0.58} p^{0.34}$	-0.58	$d^{7.71} s^{0.71} p^{0.56}$	-1.51	$d^{7.62} s^{0.85} p^{0.48}$
Pd_4	0.00	$d^{9.31} s^{0.47} p^{0.20}$			0.79	$d^{9.31} s^{0.51} p^{0.16}$
Rh_4	0.00	$d^{8.11} s^{0.55} p^{0.29}$	0.05	$d^{8.10} s^{0.56} p^{0.29}$	0.04	$d^{8.09} s^{0.60} p^{0.26}$
Ru_4	0.00	$d^{7.06} s^{0.57} p^{0.35}$	-0.44	$d^{7.14} s^{0.58} p^{0.26}$	-0.72	$d^{7.15} s^{0.59} p^{0.25}$
Co_4	0.00	$d^{7.66} s^{0.69} p^{0.60}$	-0.52	$d^{7.66} s^{0.76} p^{0.54}$	-0.40	$d^{7.67} s^{0.76} p^{0.54}$

orbitals in Pt_4 is such that it is not clear what type of geometry would be favored if the binding was only due to $5s$ orbitals. On the other hand, there is a clear preference of iridium d orbitals towards **S** structure. It follows from similar population of s orbitals in Ir_4 (as in Pt_4) and a strong energy preference to **S** isomer. This is also supported by the results from Fig.3.7 where, for $\lambda = 1.02$ or 1.03 , s population favors **T** structure, but the two isomer become almost degenerate.

In Pd_4 the **B** configuration is not stable structure and it relaxes to **S** isomer which is by 0.79 eV lower in energy than **T**. The population of $5s$ in Pd_4 prefers **T** configuration and it seems that d orbitals do not influence a lot the energy ordering of **T** and **S** isomers. The three Rh_4 structures are almost degenerate. Since population of atomic s orbitals in

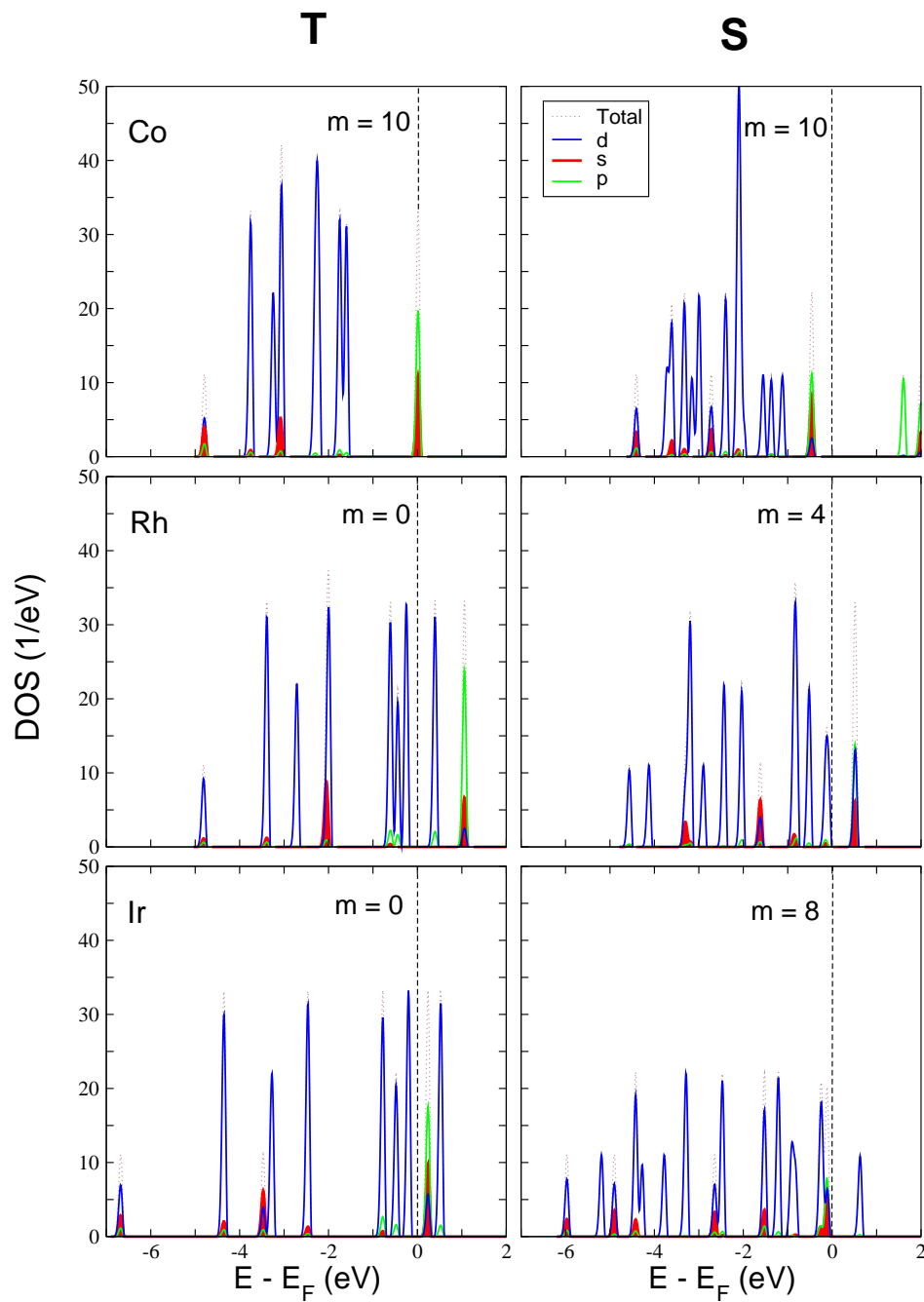


Figure 3.10: Total and projected spin majority DOS of **T** and **S** isomers of Co_4 , Rh_4 and Ir_4 (iridium column in the periodic table) are shown. Numbers denote values of the total cluster magnetic moment m (in μ_B). Similarities of Rh_4 spectra with those Ir_4 calculated using modified PP for $\lambda = 1.03$ (Fig.3.7) are obvious.

Rh₄ clusters should also have weak preference to **T** configuration it can be concluded that *d*-bonding favors (also weakly) **S** structure. In Ru₄, on the other hand, interaction of *d* AOs clearly favors **S** geometry. Population of *s* is such that the two isomers should be close in energy, but **S** is by 0.72 more stable. Situation in Co₄ is different than in other X₄ clusters presented here. The **B** isomer is the most stable followed by **S** and **T** that are by 0.12 and 0.52 eV less stable, respectively. Calculated Löwdin charges of *s* atomic orbitals should produce stronger preference towards **B** and **S** configurations. However, all three structures have high magnetic moments (10 μ_B) and the gain in exchange energy also influences relative energies of the three isomers.

Since the relative stability of different isomers in X₄ clusters depends strongly on the level *d*-*s* hybridization it also depends on the approximations used in DFT calculations, especially on XC functional. In the cases where relative energies are small (*i.e.* Pt and Rh) differences in the predictions of the most stable isomer can be expected. However, strong preference of Ir₄ clusters towards **S** structure guarantees that results obtained for Ir₄ should be robust enough that reliable conclusions can be drawn. It is shown in Sec.3.4 that, in order to alter relative stability between **T** and **S** isomers, one needs to reduce the level of *d*-*s* hybridization. On the other hand, the method that yields that level of *d*-*s* hybridization would produce poor description of Ir atom (completely wrong population of atomic orbitals) and probably would fail in reproducing properties of the bulk iridium.

Chapter 4

Influence of Adsorbates on the Stability of Ir₄ clusters

Understanding the interactions of (potential) catalysts with atomic species is the first step in understanding their interactions with more complicated molecular systems. Since atomic H as well as O are always present in real situations and since carbon is a key ingredient of all organic molecules, interaction with these three atomic species is probably among the most important to study. Moreover, the experimental procedure used to produce supported Ir₄ clusters involves quite complicated decarbonylation of Ir₄(CO)₁₂ molecules. Hence, the experimentally produced tetrairidium clusters could contain atomic or molecular impurities. To investigate the effect of adsorbates on structural properties of Ir₄, atomic H, C, and O as well as CO molecules are added to the clusters. Results for adsorption of these adsorbates on the gas-phase clusters are presented in the following two sections.

4.1 Adsorption of H, C or O atoms

The most favorable geometries of Ir₄X (X = H, C and O) complexes, their total energies and binding energies of the species adsorbed on the three gas-phase Ir₄ isomers are shown in Fig.4.1 and Tab.4.1, respectively. While interaction of atomic H and H₂ with Ir₄ has already been studied [71, 72], adsorption of atomic O and C on Ir₄ is a novel result. Computational method was tested against the already published data for the adsorption of atomic H, C and O over Ir(111) surface and the agreement with theoretical predictions as well as with available experimental results is confirmed (check reference [86] and the references therein).

It is found during this work (reported in reference [69]) that adsorption of one carbon atom in the most stable, bridging configuration, alters relative stability predicted for clean gas-phase Ir₄ clusters. At **T** and **B** isomers binding energies of the C adatom are 8.24 and 8.00 eV, respectively. These values, by 1.82 and 1.58 eV larger than that found at the **S** cluster, show that big differences in the C chemisorption lead to the change in the isomer stability in favor of **B** configuration. The energy preference of **B** compare to **T** isomer is 0.34 eV. On the other hand, differences in binding energies of both H and O adatoms are much smaller than the relative energies of the three isomers. Therefore, the energy ordering of the three structures remains the same as for the clean gas-phase Ir₄. All three types of adsorbates bind stronger to **T** and **B** isomers than to clean defect-free Ir(111) surface. This is also true for the adsorption of atomic H and O on **S** structure. However, C adatom binds by 0.29 eV

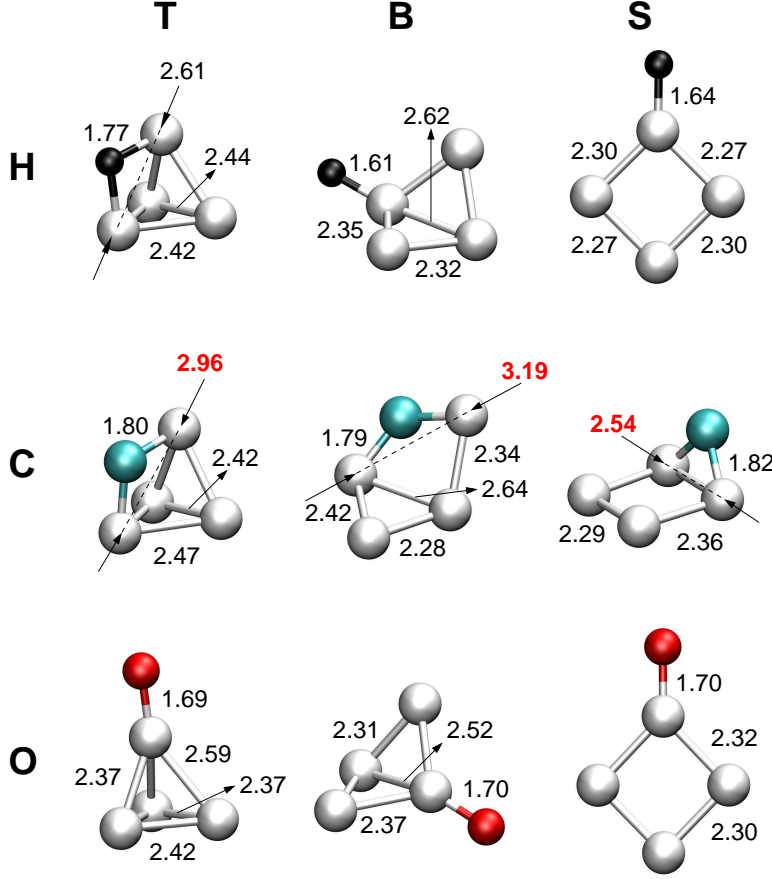


Figure 4.1: The most favorable adsorption geometries of atomic H, C and O on the gas-phase Ir_4 clusters in **T**, **B**, and **S** configurations. Numbers denote interatomic distances (in Å).

Table 4.1: Properties of the three gas-phase Ir_4 isomers (**T**, **B** and **S**) interacting with atomic H, C and O. Total energies ΔE (eV) with respect to that of **T** configuration, binding energies E_b (eV) of the adsorbed species and total magnetic moments m (μ_B) of the molecules are shown. Results for the adsorption on Ir(111) surface are also shown for comparison.

	T			B			S			Ir(111)
	ΔE	E_b	m	ΔE	E_b	m	ΔE	E_b	m	E_b^1
H	0.00	3.12	1.00	-0.82	3.36	3.00	-1.54	3.15	3.00	2.73 (top)
C	0.00	8.24	2.00	-0.34	8.00	4.00	0.31	6.42	4.00	6.71 (hcp)
O	0.00	6.47	2.00	-0.62	6.51	2.00	-1.26	6.22	4.00	4.57 (fcc)

1 Values taken from reference [86]

weaker to **S** isomer than to Ir(111) surface. This indicates that it is not only the reduced coordination compared to the atoms at surfaces that influences stronger reactivity of clusters, but also geometry and type of adsorbates play an important role.

The carbon adatom in the bridging site induces much larger distortions when adsorbed on the **T** and **B** than on the **S** isomer, as shown in Fig.4.1. The Ir–Ir bond bridged by carbon,

in the **T** and **B** structures is elongated to the values of 2.96 and 3.19 Å, respectively. The corresponding distance of 2.54 Å calculated for the **S** isomer remains close to the value in the pristine cluster, indicating that the Ir–Ir bond is not broken. By looking at the electronic density of the three structures in the plane defined by the two Ir atoms and the bridging carbon (Fig.4.2(b)), this residual Ir–Ir bonding in the **S** structure can clearly be seen. Even though in all three cases there is no critical point in the density along the line that connects two Ir atoms and, therefore no bonding line in the sense of Bader analysis [74], the gradient of the density in the direction perpendicular to that line is much larger for the **T** and **B** isomers than for the **S** one. Hence, change in the electron density between the two Ir atoms of **S** isomer is smaller, reflecting the residual interaction. This is further supported by the shape of the C–2*p* projected density of states shown in the Fig.4.2(a). Larger part of the C–2*p* spectral weight is transferred to lower energies in the cases of **T** and **B** isomers than in the **S** one.

For all three isomers weak interaction of carbon 2*s* and stronger interaction of carbon 2*p* orbitals with the clusters' MOs exist. The biggest contribution to the carbon binding energy comes from the interaction of its 2*p_z* orbitals (*z*-axis is as in Fig.4.2(b)) with molecular orbitals (MOs) of the clusters. These MOs of the **T** and **B** structures show strong antibonding character. They mostly belong to the unoccupied parts of the two spectra and after the interaction with the carbon adatom they become occupied which facilitates breaking of the corresponding Ir–Ir bonds. This is easier to see for **T** isomer where the unoccupied MO of the cluster that interacts with C–2*p_z* orbital corresponds to one of the low energy (with respect to E_F) orbitals with mixed T_1 and T_2 character (shown in Fig.3.5). The corresponding MO of **S** structure is a combination of half-filled B_{1g} (also shown in Fig.3.5) with a number of occupied MOs. It has much less pronounced antibonding character.

Therefore, the strongly antibonding MOs of the **T** and **B** clusters are transformed by the interaction to strongly bonding and the energy gain is much bigger for those two isomers than for the **S** one. In addition, interaction of the C–2*p_x* atomic orbital with the filled MOs of **T** isomer is also significant (second peak in the projected DOS). The MO formed by the interaction of C 2*p_y* AO and MOs of **S** structure, represented in the DOS by the second smaller peak, clearly shows the residual Ir–Ir interaction. Shapes of MOs of intermediate **B** structure after the interaction resemble features of the other two isomers. Strong interaction of the C–2*p_z* state with the antibonding MO of the free cluster gives the main contribution to the binding energy of 8.00 eV, while the interaction of 2*p_x* and 2*p_y* atomic orbitals is clearly a transition between **T** and **S** structures.

On the other hand, both H and O adatoms are not capable of altering energy ordering of the three Ir₄ isomers. As already reported [71] hydrogen binds to **T** structure in the bridging configuration as well, but due to the symmetry reasons it is not able to interact with the same strongly antibonding MOs of the cluster. In fact, H binds stronger to the single Ir atom, but this geometry is not stable and transforms to one of the butterfly Ir₄H configurations¹. Oxygen adatom, due to differences in its electronic configuration compared to carbon (see Fig.4.3), binds preferentially to a single Ir atom in all three cases.

¹In this case H adatom interacts with strongly antibonding MOs of the cluster. Resulting structure is not the most stable **B** configuration with the H adatom and therefore, is not presented here.

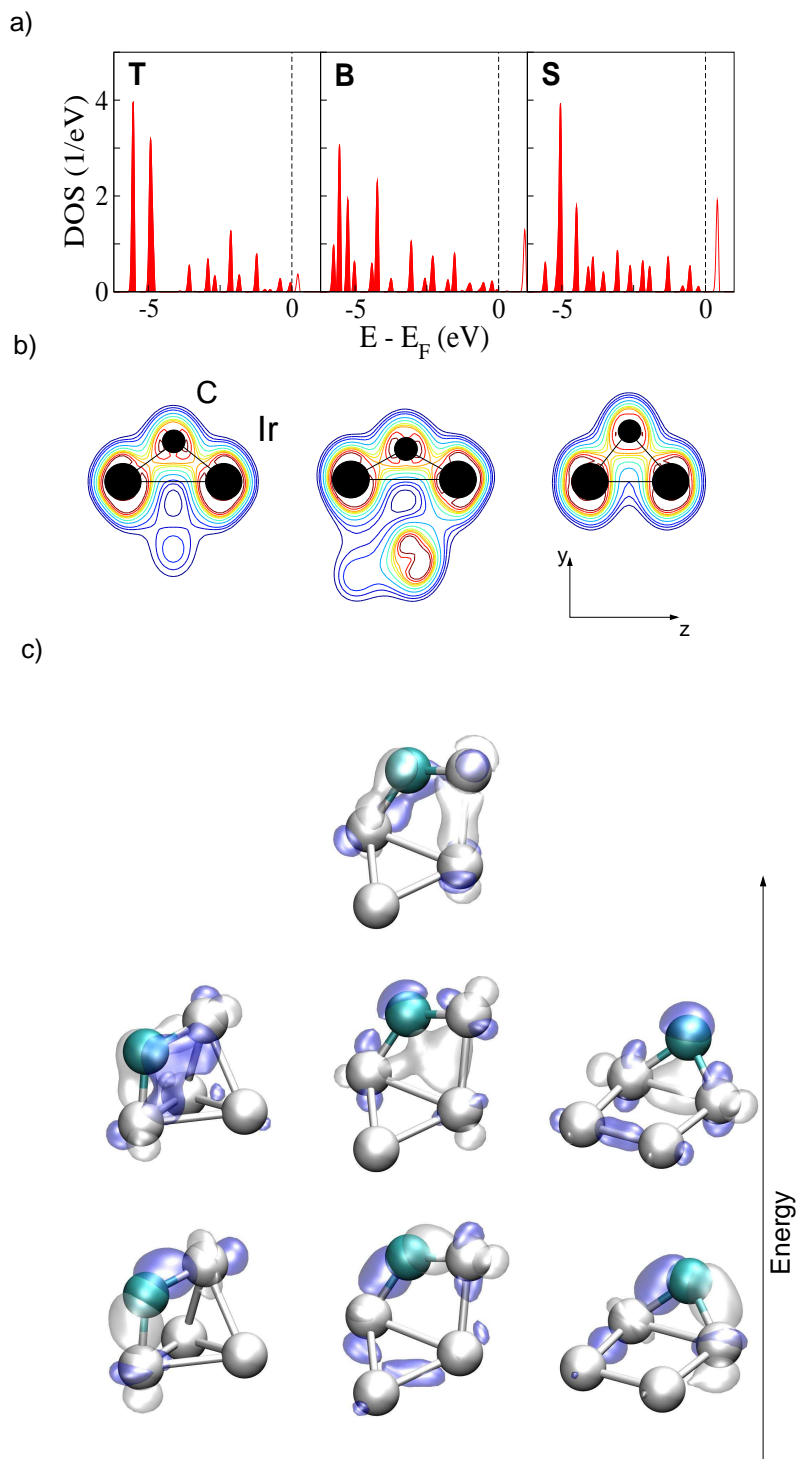


Figure 4.2: a) Spin majority C-2p Löwdin projected DOS of the three Ir₄C molecules. b) Contour plot of the electronic density of the three Clr₄ molecules in the plane determined by the two Ir atoms interacting with a bridging C adatom. c) Kohn-Sham molecular orbitals of the three molecules corresponding to the peaks in the C-2p projected DOSs.

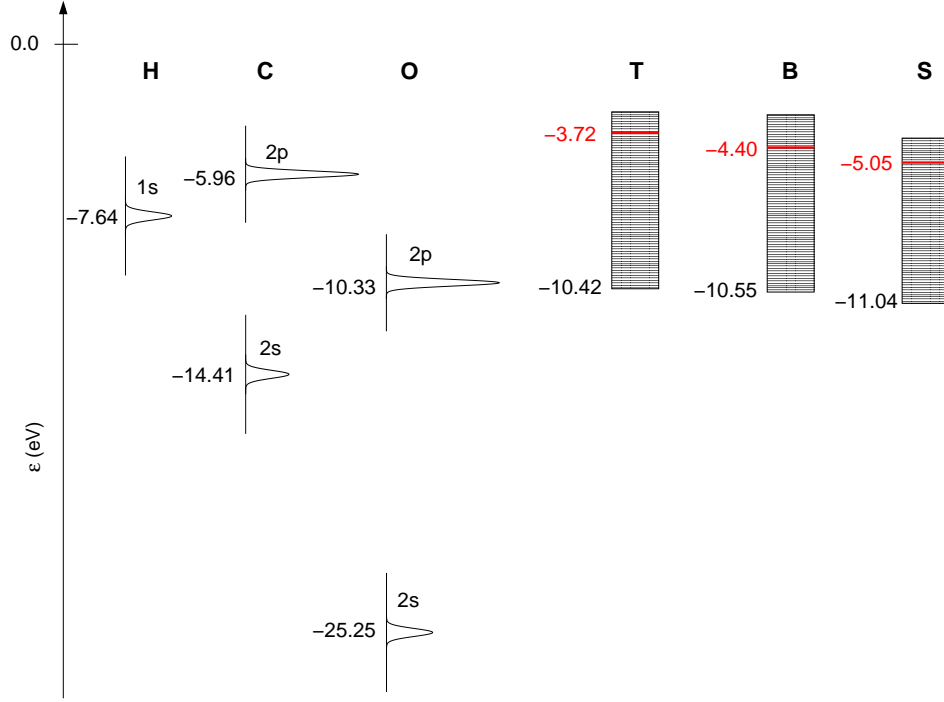


Figure 4.3: Schematic plot of the relative positions of the spin majority KS energy levels of atomic H, C and O and energy ranges of the occupied parts of electronic spectra of the three Ir₄ isomers (**T**, **B** and **S**). Spectra are aligned to the same vacuum level. Numbers denote energies of the corresponding levels while red horizontal lines represent the Fermi energies.

4.2 Adsorption of a single CO molecule

Many possible configurations of a CO molecule interacting with the three Ir₄ isomers (**T**, **B** and **S**) are carefully inspected and the properties of the most stable ones are presented in Tab.4.2 and Fig.4.4. Both molecular and dissociative adsorption are studied. The CO binding energies are always calculated using the isolated CO molecule as the reference.

Accuracy of the method is tested against available experimental data. Calculated CO atomization energy $E_a = 10.97$ eV, bond length $r_e = 1.155$ Å and the frequency of its stretching mode $\hbar\omega = 272$ meV (2198 cm⁻¹) agree reasonably well with the experimental values ($E_a = 11.17$ eV [87], $r_e = 1.128$ Å and $\omega = 2169.8$ cm⁻¹ [88]). Moreover, DFT predicts correct adsorption site of a CO molecule on Ir(111) surface [86] which is also confirmed in this work.

Molecular CO displays a range of bonding modes with transition metal clusters. The CO ligand is usually observed as terminal, edge-bridging or face-capping [15]. When adsorbed to Ir₄ clusters a single CO adsorbed in the molecular form binds stronger in the terminal geometry with the carbon atom in contact with the cluster (Fig.4.4). The CO binds slightly stronger to **B** than to **T** isomer, while the difference in binding energies is bigger ~ 0.5 eV compared to the adsorption at **S** structure. The binding to Ir₄ is stronger by 0.55–1.1 eV than at Ir(111) terraces for all three cluster geometries (see Tab.4.2).

Interaction with the molecular CO does not induce significant deformations of the three Ir₄ structures. Certainly, the symmetries of the clusters are broken and the distortions exist,

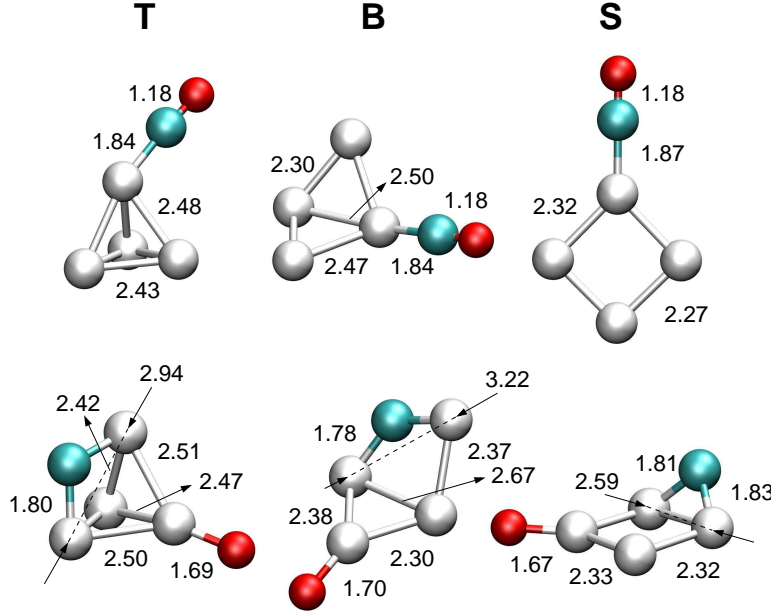


Figure 4.4: The most favorable adsorption of a CO molecule on the gas-phase **T**, **B**, and **S** Ir₄ clusters. For all three structures adsorption of the CO both in molecular and dissociated form is presented. Numbers denote interatomic distances (in Å).

Table 4.2: Energetics of the three gas-phase Ir₄ isomers (**T**, **B** and **S**) interacting with a single CO molecule both in molecular form (full) and dissociated (diss.). Total energies ΔE (eV) with respect to that of Ir₄CO in **T** configuration with a CO molecule in the dissociated form and binding energies E_b of the CO molecules are presented. Values in parentheses denote binding energies of O adatom to the Ir₄C molecule. All energies are in eV.

	T		B		S		Ir(111)
	ΔE	E_b	ΔE	E_b	ΔE	E_b	E_b^1
CO full	0.83	3.16	0.19	3.23	-0.20	2.68	2.13
CO diss.	0.00	3.99(6.70)	0.03	3.38(6.34)	0.75	1.72(6.25)	0.32

¹ Values taken from reference [86]

but they are less than 0.1 Å on average for all three structures. Both **B** and **S** structures remain magnetic upon the interaction ($4 \mu_B$ in both cases), while the ground state of **T** isomer with one terminal CO ligand is, as for the free cluster, nonmagnetic.

Dissociated, a single CO binds considerably stronger to **T** (by 0.83 eV) and only slightly stronger to **B** isomer (by 0.16 eV). On the other hand, dissociative adsorption on **S** structure is by 0.95 eV less favorable (qualitatively similar to the adsorption at Ir(111) surface) than adsorption in the molecular form. By inspecting adsorption geometries (Fig.4.4) this huge difference in the energetics of the CO dissociation reaction on the three isomers can be associated to a particularly strong binding of carbon adatom in the bridging configuration to both **T** and **B** isomers. The coadsorbed oxygen binds almost as strong as without carbon (check Tables 4.1 and 4.2). Upon the interaction with a single CO molecule **S** isomer with a single

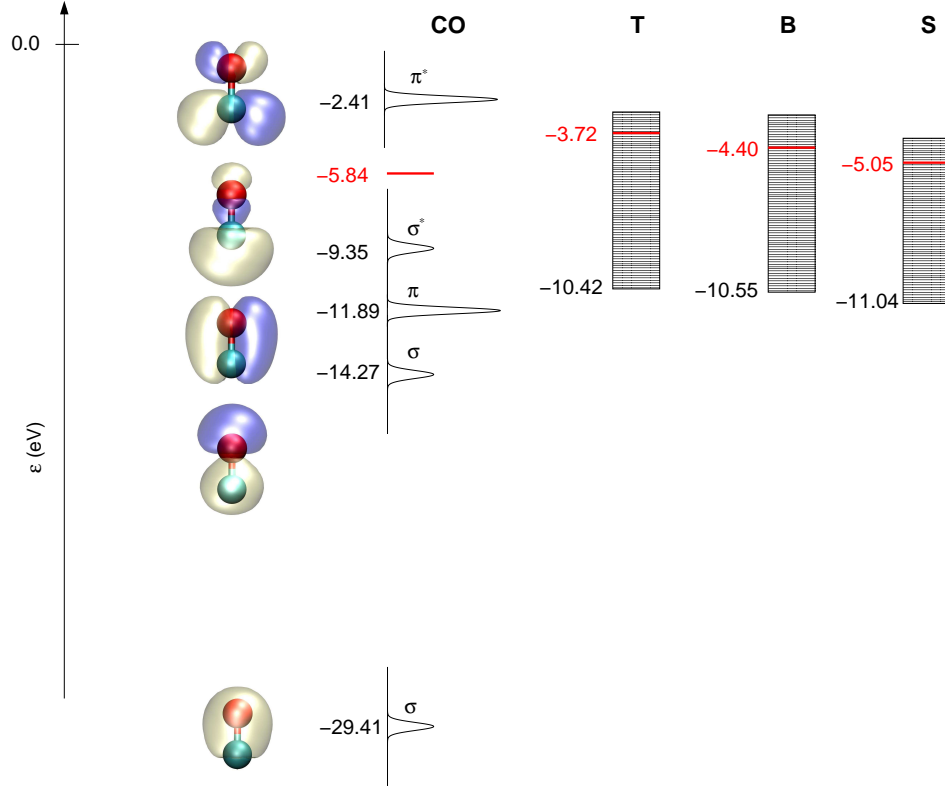


Figure 4.5: Schematic plot of the relative positions of the spin majority KS energy levels of a CO molecule and energy ranges of the occupied parts of electronic spectra of the three Ir₄ isomers (**T**, **B** and **S**). The same description as for Fig.4.3 applies also here. The corresponding CO molecular orbitals are also displayed.

molecular CO is the most stable Ir₄ structure, but now only by 0.20 and 0.23 eV more stable than **T** and **B** structures with the dissociated CO, respectively.

Interaction of a single CO molecule, adsorbed in the molecular form, with the transition metal clusters is similar to the interaction with surfaces of transition metals. It can be understood in terms of the charge donation from the CO molecule to the metal and backdonation to the molecule [15, 89]. At surfaces, it is proved that highest occupied σ molecular orbitals (HOMO) and lowest unoccupied π^* molecular orbital (LUMO) of the CO (see Fig.4.5) are mainly responsible for the interaction [90, 89]. Charge is donated from the HOMO to the metal surface and backdonated to the LUMO. Backdonation to the antibonding π^* orbitals increases the C–O distance and facilitates σ donation which in turn increases backdonation and so on (cooperative σ – π^* bonding).

Mechanism of binding to the clusters is similar. However, deeper CO orbitals also play a role in binding. In fact, due to reduced symmetry σ and π orbitals are able to mix. Only, the lowest σ and the LUMO of the CO molecule do not hybridize much with the others because of the big energy difference (Fig.4.5). In Fig.4.6 (upper panel) the total and DOS projected (within the Löwdin scheme [55]) on the orbitals of CO molecule are shown. The lowest energy σ orbital of the CO molecule (mostly of the O-2s character) at ~ -23 eV below the E_F is not shown. Each of the three spectra can be divided in two regions (shorter dashed line in

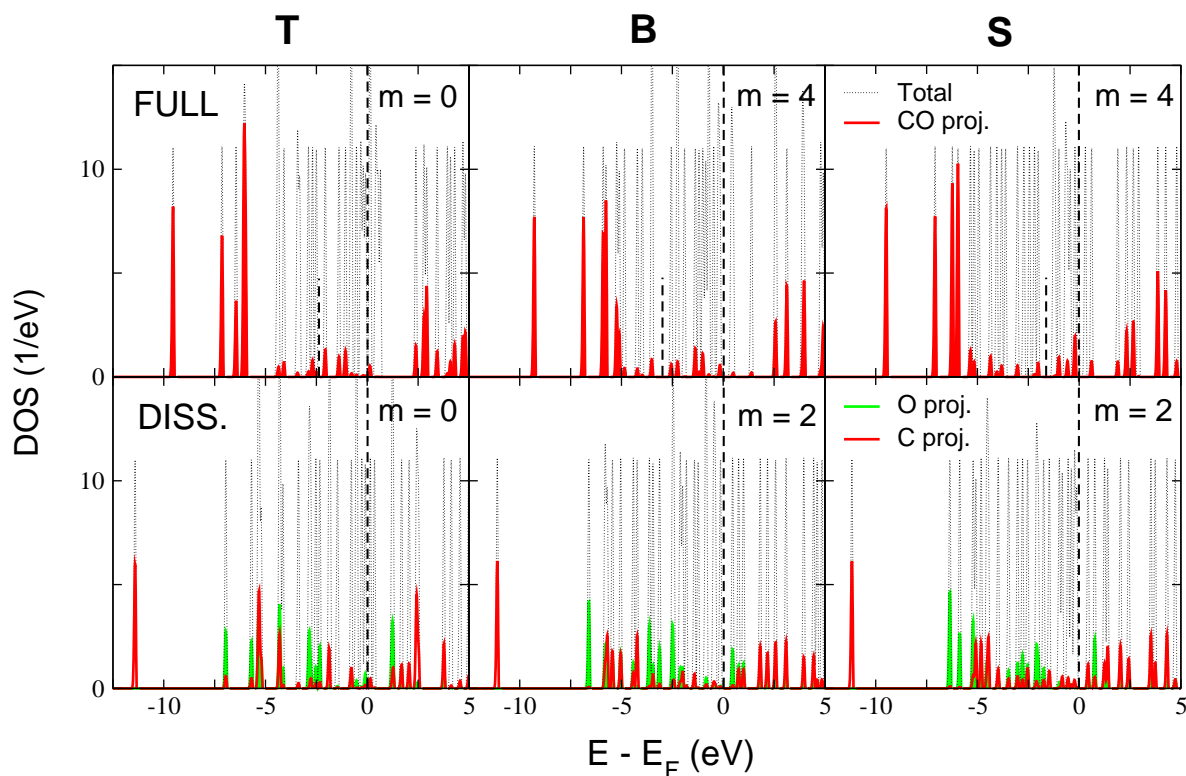


Figure 4.6: Spin majority total and CO projected DOS (using the Löwdin scheme [55]) of the three Ir_4CO geometries (**T**, **B** and **S**). Densities of states are shown for both CO adsorption in the molecular form (upper panel–FULL) and dissociative CO adsorption (lower panel–DISS.). Dashed lines (shorter) in the upper panel delimit σ – π and π^* parts of the spectra.

Fig.4.6), low energy region that is of the CO mixed σ and π character, and high energy region which is exclusively of the π^* character. Energies of the bonding π^* combinations lay closer to the Fermi energy while parts of the spectra around and above 2.5 eV are composed of the antibonding π^* combinations with the orbitals of the three Ir_4 clusters. By integrating π^* projections up to the E_F it is possible to estimate the amount of the backdonation from the three Ir_4 isomers to the CO molecule.

The biggest backdonation occurs for the CO molecule adsorbed to **B** isomer. In total, 0.82 electrons are transferred from the CO molecule to the cluster², 0.44 and 0.38 electrons in the spin majority and minority channels, respectively. Somewhat smaller amount of charge 0.36 electrons in each spin channel is backdonated to the CO molecule from **T** structure. In case of the CO adsorption to **S** isomer, filled bonding π^* combinations in the spin majority channel are shifted closer to the Fermi energy and due to the magnetization of the cluster ($4 \mu_B$) these orbitals in the spin minority channel remain mostly empty. Therefore, the backdonation is the smallest for the adsorption to **S** structure and amounts to 0.34 and 0.1 electrons divided in two spin channels. Differences in the amount of the backdonation correspond well to the ordering of the CO binding energies to the three isomers proving that the proposed binding mechanism is correct.

²Since the total charge transfer is very close to zero for CO adsorption to all three Ir_4 isomers, this number also measures the charge donation.

In the lower panel of Fig.4.6 the total and projected DOS of the three Ir₄ isomers with a single CO molecule in the dissociated form are shown. The O-2s atomic orbital that does not interact with any of the clusters' electronic states is not presented. It is obvious from the three spectra that coadsorbed C and O adatoms interact with different molecular orbitals of the three clusters. Only minor changes are produced in the binding energies of the two atoms compared to the binding energies of the single C or single O atoms. This can be proved by summing C and O binding energies from the Tab.4.1 and subtracting the energy of 10.97 eV needed for the CO atomization. Resulting energies are 3.74 eV (**T**), 3.54 eV (**B**) and 1.67 eV (**S**) proving that C and O coadsorption are to a good approximation two independent processes³.

4.3 CO Dissociation on Ir₄

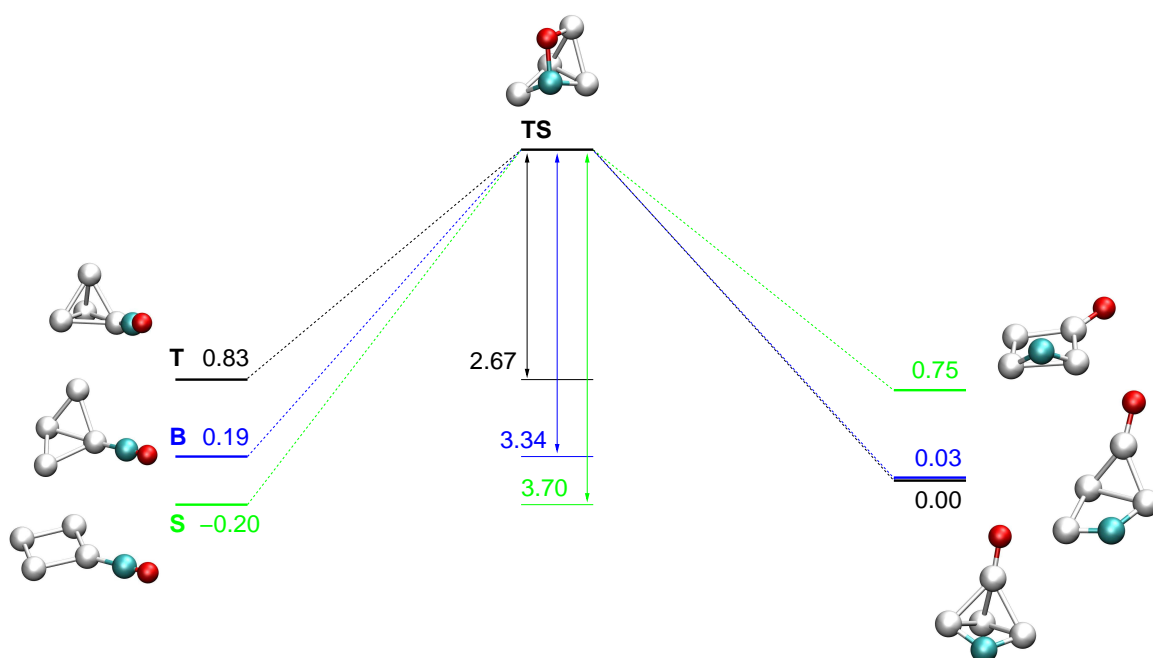


Figure 4.7: Initial, final and transition state (TS) configurations for the CO dissociation on the three Ir₄ isomers (**T**, **B** and **S**) are shown. Numbers denote energies (in eV) of the initial and final configurations relative to that of **T** final configurations (as in Tab.4.2). Energy of the transition state is determined by the three energy barriers. Notice that the transition state is the same for CO dissociation on any of the three Ir₄ isomers.

Dissociation of carbon monoxide is an important chemical reaction for industrial applications (see Chapter 1). It is also one of the important reactions in the transition metal carbonyl cluster chemistry. Moreover, stability of **T** isomer found in experiments on supported Ir₄ clusters can be explained by assuming the presence of adsorbates, C adatoms in

³In the case of **T** calculated total binding of the two adatoms is by ~ 0.2 eV stronger and in the case of **B** is ~ 0.2 weaker than these numbers. This is only a small portion of the total binding energy, but it makes the two isomers with the dissociated CO molecule almost degenerate.

particular (see Chapter 6). One possible source of C adatoms are carbonyl ligands present during the preparation procedure.

The CO dissociation over the surfaces of transition metals has already been studied by the means of density functional theory. It is found that the reaction requires as much as 1.11 eV on Fe(100) surface [91], while the same reaction takes to occur as much as ~ 3.20 eV on Rh(111) terraces, ~ 2.0 eV on the stepped Rh(210) surface [92] and about 2.70 eV on Co(0001) surface [93]

On the three Ir₄ clusters the CO dissociation reaction is studied using the CINEB approach (see Sec.2.2.5) starting from the configurations with a CO molecule adsorbed in the molecular form (initial configurations) and taking the structures after the dissociative CO adsorption as the final configurations. Many different pathways have been inspected for the CO dissociation on all three Ir₄ structures. One dimensional energy diagram for the reaction is shown in Fig.4.7. The reaction is exothermic on both **T** and **B** isomers while it is necessary to invest at least 0.95 eV for the reaction to occur on **S** structure.

It turns out that the minimal energy paths (MEP) for the reaction on all three isomers pass through the same transition state. It is located in the butterfly-like configuration with the carbon atom bridging the two "wing" Ir atoms, while the oxygen is also placed in bridging position, but between the C and the wing-tip Ir atom of the opposite wing. This configuration enables strong interaction between C-2*p* orbitals, as already explained in Sec.4.1, which on the other hand, weakens the C-O bond through the backdonation mechanism. However, the situation is rather peculiar since it is not clear which route will be taken when going from the transition state in either direction.

Since the transition state is the same, energy barriers for the reaction on all three isomers are determined by the energies of the initial configurations. The biggest activation energy 3.70 eV is for the reaction on **S** structure while the activation requires at least 3.35 and 2.67 eV for the CO dissociation on **B** and **T** isomers. respectively. These barriers are quite big and the CO dissociation requires, according to Eq.2.19 with the prefactor of 10^{13} Hz (the CO stretching frequency), temperatures of over 1000° C. However, the barrier on **T** isomer is by 0.49 eV lower than the CO binding energy indicating that the CO dissociation is more favorable process (provided there is enough energy) on **T** isomer than the CO desorption. Influence of possible promoters for this reaction, *i.e.* other CO molecules present on the cluster that would interact with the oxygen atom and form CO₂, have not been studied yet.

Chapter 5

Ir₄ Clusters Supported by MgO(100) and TiO₂(110) Substrates

Adsorption of the metal particles over an oxide support is an important step in preparation of the real catalysts. Understanding the interaction of the metal clusters with an oxide surface at the atomic scale enables better control of the process of preparation and better insight into the properties of the adsorbed species.

The adsorption of different Ir₄ isomers on two widely used (both experimentally and theoretically) oxide surfaces, rocksalt MgO(100) and rutile TiO₂(110) is studied in this chapter. The influence of the support on relative stability, atomic and electronic structure of the adsorbed species is analyzed and the obtained results are compared to the available experimental data. Diffusion mechanisms on defect-free MgO(100) surface are also studied as well as the influence of point defects (neutral and charged oxygen vacancies) present on MgO(100) on the properties of the adsorbed Ir₄ clusters.

At the beginning the properties of the clean surfaces are presented. The theoretical model used for predictions is introduced through the analysis of the clean surfaces as well as the adsorption of atomic iridium on defect-free MgO(100) surface.

5.1 Bulk Oxides and Their Surfaces

5.1.1 Bulk MgO and the MgO(100) Surface

Bulk MgO is a material extensively studied both experimentally [95, 96] and theoretically [98, 99, 100, 101] due to its importance in technological applications. In this work bulk MgO is modelled using similar numerical setup as that already used for gas-phase Ir clusters (Chapter 3).

The ultrasoft pseudopotentials are employed with the same cutoff energies (25 and 140 Ry for wavefunctions and augmented charges, respectively). Brillouin zone integration is performed over 6×6×6 Monkhorst–Pack mesh [30]. Converged structural parameters, lattice constant of the rocksalt MgO $a_0 = 4.26$ Å and bulk modulus $B = 150$ GPa lay within standard DFT error bars (1–2 % for lattice constants and ~10 % for bulk modulus) compared to the experimental $a_0 = 4.21$ Å and $B = 155$ GPa [95]. On the other hand band-gap of the

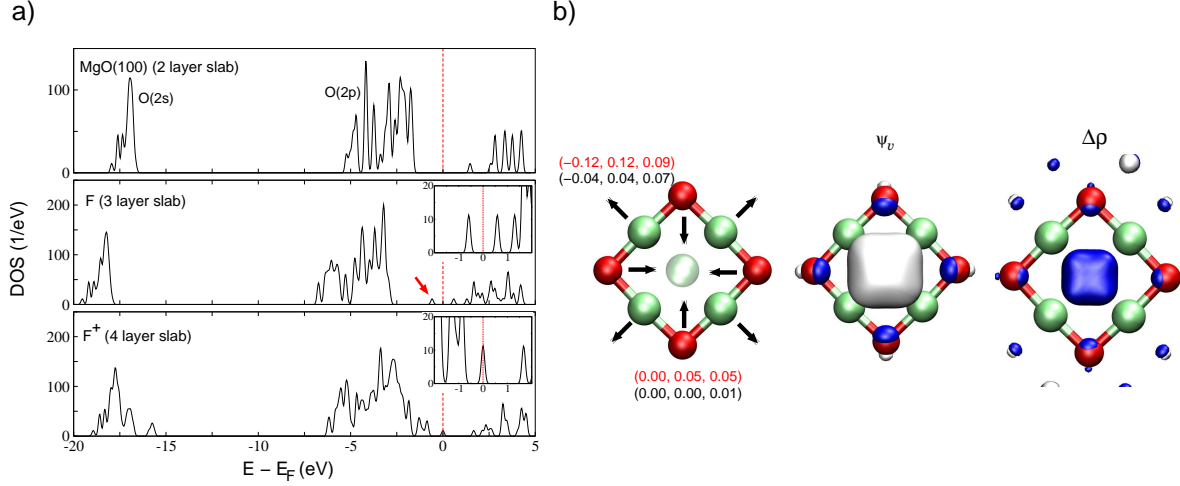


Figure 5.1: (a) Total DOS of MgO(100) surface, defect-free as well as with neutral (F) and charged oxygen vacancies (F⁺). Insets show structure of the corresponding DOS around Fermi energy. The arrow indicates states in the band-gap formed upon creating the vacancy. (b) From left to right: relaxations of surface atoms close to the vacancies with (x, y, z) displacement vectors for both F (black) and F⁺ (red) centers; electronic orbital of the neutral vacancy appearing in the surface band gap; and the difference of the electronic densities $\Delta\rho = \rho_F - \rho_{F^+}$, isosurfaces are at $\pm 0.08 e/\text{\AA}^3$ and negative value is represented by the blue isosurface.

system is severely underestimated 4.49 against experimental 7.8 eV [97]. This is a well known feature of DFT methods since the Kohn–Sham eigenvalues do not formally correspond to excitation energies. Different values obtained theoretically are reported in literature and the value calculated in this work agrees well with that from reference [99], obtained within similar theoretical scheme.

Clean, defect-free MgO(100) surface is modelled with a supercell periodic slab approach. Large $4\sqrt{2}/2 a_0 \times 4\sqrt{2}/2 a_0$ surface unit cell is used. Sampling of the surface Brillouin-zone is restricted to the Γ -point only. Population of the KS electronic orbitals is done according to the Fermi distribution function with $k_B T = 0.1$ eV. Periodically repeated slabs are separated by the vacuum region chosen in such a way that the perpendicular translational period equals to the thickness of ten MgO(100) layers (21.3 Å). Further increase of the vacuum did not result in any appreciable change of the physical quantities of interest, *i.e.* binding energies of adsorbates. It is shown in Sec.5.2 that only two layer slab with the bottom layer fixed in the calculated bulk configuration is sufficient to obtain converged binding energy of atomic iridium (check also reference [103]). The asymmetric two layer slab is also good enough to reproduce structural properties of MgO(100) surface. Almost zero relaxation of the top layer plane and ~ 2 % positive rumpling¹ is in line with results reported in reference [100] obtained with the slab containing seven layers.

On the other hand, two layers of MgO(100) are not sufficient to calculate accurately the band gap of the surface. Moreover, the asymmetric configuration with a small number of layers is not suitable for calculating band gaps at all since the states localized at the top of the valence band typically belong to the unrelaxed bottom layer. Therefore, calculations

¹Rumpling is defined as the ratio $(z_O - z_{Mg})/d_{\text{bulk}}$, where z_O and z_{Mg} are z coordinates of the top layer O and Mg atoms while d_{bulk} represents the bulk interlayer distance.

using the symmetric slab are performed and converged surface band gap of 3.62 eV is obtained using five MgO(100) layers (equivalent to 3 layer asymmetric slab). The "unconverged" gap of our model does not influence binding energies of iridium clusters since they interact only with states from the surface valence band (see following sections).

The valence bands of MgO(100) surface can be associated to O 2s and O 2p orbitals (structures around -17 and -5 eV in Fig.5.1(a)). On the other hand states from the conduction band do not follow "simple" charge-transfer model of ionic materials. The nature of the states in the conduction band of bulk MgO as well as the reduction of the band gap upon forming MgO(100) surface is elaborated in details in reference [101] and will not be discussed further here.

Neutral oxygen vacancy (F center) is produced by removing one of the surface O atoms. Since the oxygen removal induces additional relaxations of both topmost and layers below, the three layer slab was used in calculations. Again, only the bottom layer is kept fixed and the other two are fully relaxed. As shown in Fig.5.1 removal of the surface O atom leaves two electrons localized both in energy (state marked by arrow appearing in the band gap) and in the space between neighboring Mg ions. The description of the neutral vacancy goes in line with the results reported in reference [102].

Charged O vacancy (F^+ center) is simulated, by replacing the substrate Mg cation, belonging to the bottom layer, with a Na cation which has one less valence electron. The charge that is concentrated in the vacancy is reduced, by this procedure, from two to one electrons (see Fig.5.1(b)). In this way the problem of electrostatic interactions between supercells is circumvented. Similar model was successfully employed by Molina *et al.* [103]. In order to avoid relaxations that could be induced by the presence of the Na cation calculations are performed with the four layer slab with positions of the two bottom layers fixed while positions of all the other atoms are fully relaxed.

Electronic state localized in the band gap is shifted, upon charging, closer to the valence band in agreement with results reported in reference [102]. It has been proved that the exact position of Na in the bottom layer does not influence energetics of Ir adsorbates. The DOS structure at the top of the valence band around -1 eV (Fig.5.1) is an artifact of the model and it is due to the presence of sodium. However, those states are localized in the bottom layer (O atoms around the Na cation) and do not influence interaction with adsorbates.

5.1.2 Bulk TiO_2 and the $\text{TiO}_2(110)$ Surface

Bulk rutile TiO_2 is modelled with the ultrasoft pseudopotentials and $6 \times 6 \times 8$ \mathbf{k} -point grid. Converged structural parameters ($a = 4.65$ Å, $c = 2.98$ Å and $B = 234$ GPa) are in a good accord with the experimental ones ($a = 4.587$ Å, $c = 2.954$ Å and $B = 211$ GPa [104, 105]). Calculated band-gap of the material $E_g = 1.92$ eV is underestimated compared to the experimental gap $E_g^{exp} = 3.0$ eV [106] and is in line with other theoretical predictions [107, 108].

Surface calculations are performed with a four layer asymmetric slab (Fig.5.2). Only the bottom layer of the slab is kept fixed in the theoretical bulk configuration, while all the others are fully relaxed. Monoclinic supercell is used with the in-plane dimensions $\sqrt{2}a^2 + 4c^2$ and $4c$ whose unit vectors form the angle $\alpha = 47.85^\circ$. Dimension of the supercell in the perpendicular direction equals to $5a\sqrt{2}$ (ten surface layers ≈ 32.88 Å). The Brillouin zone is sampled with $2 \times 2 \times 1$ Monkhorst-Pack mesh [30]. This geometry ensures at least 6 Å distance between the periodic images of the adsorbed Ir_4 clusters. Further increase of the

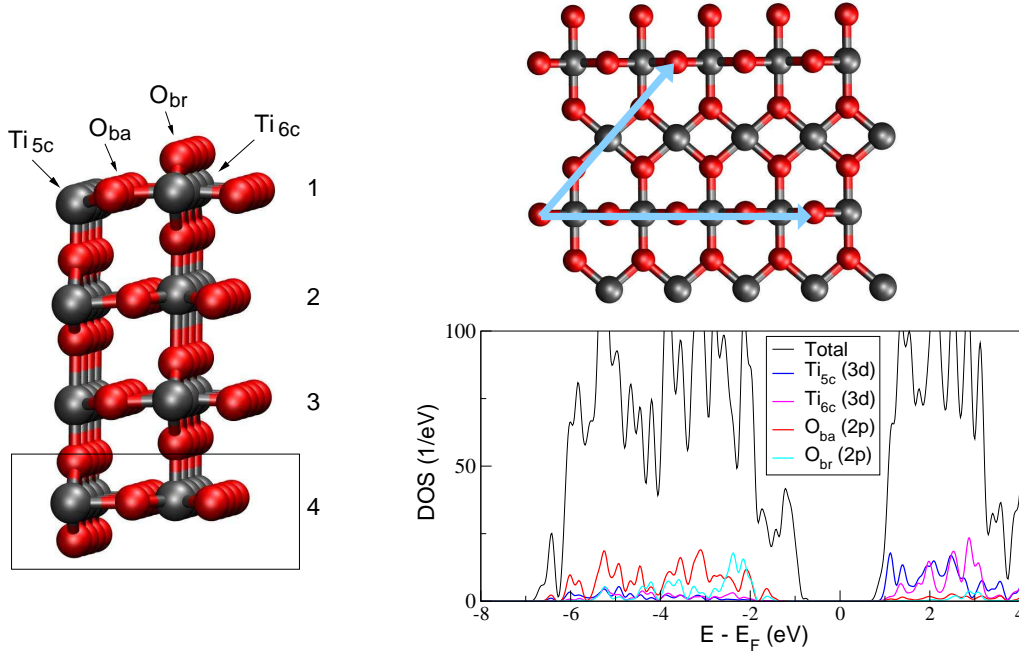


Figure 5.2: The four layer asymmetric slab used to model stoichiometric $\text{TiO}_2(110)$ surface (left). Arrows denote two types of the surface Ti (five and six fold coordinated) and O (bridge and basal) atoms nonequivalent by symmetry. The rectangle encloses the fixed fourth layer of the slab. The surface unit cell used in calculations (right up) and the total DOS of the TiO_2 surface (right) together with the projections on the atomic orbitals of the surface atoms.

unit cell, the number of \mathbf{k} -points or the vacuum region resulted in changes of binding energies smaller than 0.02 eV.

Description of the atomic structure of stoichiometric $\text{TiO}_2(110)$ surface obtained with the explained setup agrees well with other theoretical results available in the literature. Discrepancies of the surface relaxations compared to experiments are of the order of several 10^{-2} Å (reference [106] and the references therein). The asymmetric slab approach provides good convergence of the surface structural properties. In this way the even-odd oscillations of the surface relaxations with respect to the slab thickness are avoided (for details check reference [109]). On the other hand, as already discussed in previous section, the asymmetric slabs are not suitable for extracting unambiguously the electronic structure of the surface close to the valence band maximum as well as the conduction band minimum². However, main features of the surface DOS are reproduced well. In Fig.5.2 the valence and part of the conduction band of the slab are shown. In agreement with the studies available in literature [110, 111] the surface valence band is mainly of the O 2p character while the Ti 3d character dominates the lower part of the conduction band. The p - d mixing in both parts of the DOS is not negligible.

²As it is also discussed in previous section this disadvantage of the asymmetric slab approach is not a problem for studying adsorption since adsorbates always interact with the states from the relaxed slab surface. It is just inconvenient for extracting the electronic properties of the surface that can be compared with experiments *i.e.* photoemission spectroscopy.

5.2 Adsorption of Atomic Iridium on MgO(100)

At variance to adsorption of Ir₄ clusters on TiO₂(110), their adsorption on MgO(100) surface can be understood from the features of the adsorption of atomic iridium. Therefore properties and adsorption mechanism of the Ir atom on MgO(100) are presented before those of the tetramers.

Adsorption of platinum group transition metal atoms over the (100) surface of MgO has already been extensively studied with both all-electron and pseudopotential DFT methods. For atomic Fe [112], Ni [113, 116, 117], Pd [115, 116, 117], Pt [114, 115, 116, 117] and Ir [117] supported by MgO(100) a clear preference to the adsorption atop the surface oxygen is found. However, binding energies obtained by different methods may differ considerably³. These differences can be associated to different reference atom used to calculate binding energies.

It is confirmed in this work that Ir atom binds in the same way as the other transition metals. Converged values for the binding energy, Ir–O bond length and the induced dipole moment are achieved using the setup equivalent to that explained in Sec.5.1.1. As shown in Tab.5.1 the asymmetric two-layer slab, with the adsorbate only on one side, and the Γ -point BZ sampling with $4a_{\text{MgO}} \times 4a_{\text{MgO}}$ surface unit cell⁴ is sufficient for achieving the accuracy of 0.03 eV and 0.01 Å in binding energy and Ir–O distance, respectively. Similar numerical setup is used by other authors for the adsorption over MgO(100) surface (see for example reference [114]). A dipole correction method (Sec.2.2.3) is used to cancel the artificial electric field produced by the charge transfer and the asymmetry of the system. The surface dipole can be calculated as the difference

$$\mathbf{P}_{\text{Ir/MgO(100)}} - \mathbf{P}_{\text{MgO(100)}} \quad (5.1)$$

between the total dipole moments of the slab with and without the adsorbate. Due to the geometry of the model the system can develop surface charges (on both surfaces of the slab) that may not be the same in the presence of adsorbates and hence does not cancel exactly when subtracting the dipole moments. To test validity of Eq.(5.1), calculations in the symmetric slab configuration with the adsorbates on both sides of the slab, which does not suffer from the abovementioned problems, are carried out. In this case surface dipole is proportional to the difference of the electrostatic potentials of the slab with and without adsorbates (aligned at the middle layer) far away from the surface. The symmetric slab approach yields essentially the same results (Tab.5.1).

Optimized geometry of the Ir atom adsorbed atop the surface oxygen is shown in Fig.5.3. Calculated binding energy of 2.33 eV is by 1.66 eV higher than at the Mg site. The surface hollow site is a saddle point for diffusion between two O atoms and lays 0.74 eV above the atop oxygen adsorption energy. The Ir binding energy of 1.39 eV is reported in reference [117], calculated within the embedded cluster all-electron approach. As already said, this difference can be associated to the different reference Ir atom. On the other hand, at the most stable oxygen site, calculated Ir–O distance 1.91 Å is in reasonable accord with the value of 2.00 Å from the same reference.

³For example binding energy of Pt atom 1.54 eV is calculated with the periodic supercell approach [114] while the value of 2.39 eV is obtained when the all-electron embedded cluster method is used [117].

⁴Strictly speaking, the smaller cell would also be sufficient to simulate adsorption of Ir atom. Bigger one is used here only because of consistency with the simulations of Ir₄ adsorption.

Table 5.1: Convergence tests of the binding energy E_b , Ir-O bond length and the z -component of the induced dipole moment p_z of atomic Ir adsorbed on MgO(100) as a function of number of layers n and a number of the special, Monkhorst–Pack (MP) \mathbf{k} -points [30] used in simulations.

n	MP grid	E_b [eV]	Ir–O [Å]	p_z [D]
asymmetric slab				
2	Γ	2.33	1.906	-0.88
	2×2	2.30	1.910	-0.92
	3×3	2.30	1.910	-0.89
3	Γ	2.35	1.898	-0.87
symmetric slab				
3	Γ	2.32	1.909	-0.87
5	Γ	2.34	1.898	-0.90

The surface distorts upon adsorption in such a way that the Ir–bonded O atom is pushed down for 0.02 Å while the neighboring Mg atoms pop up from the surface for about 0.05 Å. These local distortions are not enough to change sign of the surface rumpling as in the case of Pt adsorption [114].

To rationalize binding of atomic Ir to MgO(100) surface analysis of the electronic structure is performed. Both charge transfer and projected density of states (PDOS) onto atomic orbitals are studied and the results are presented in Fig.5.3 and Fig.5.4. Charge transfer is estimated using the in-plane integrated electronic density difference along z axis

$$\Delta\rho(z) = \int \int \Delta\rho(x, y, z) dx dy = \int \int [\rho_{\text{Ir/MgO}} - \rho_{\text{Ir}} - \rho_{\text{MgO}}] dx dy, \quad (5.2)$$

where $\rho_{\text{Ir/MgO}}$, ρ_{Ir} and ρ_{MgO} are electron densities of the full system and the two non-interacting subsystems, Ir atom and MgO(100) surface (in their frozen interacting configurations), respectively. It is clear from Fig.5.3(b), in which only the region where $\Delta\rho$ is significantly different from zero is displayed, that the charge transfer occurs from the surface to the adsorbate. It can be estimated by integrating $\Delta\rho(z)$ up to the mid-plane between the two subsystems (red dashed line in Fig.5.3(b)) to 0.31 e resulting in the surface dipole of 0.88 D directed from the adsorbate to the surface. If a simple point charge model is constructed with the negative charge (-0.31 e) positioned in the center of $\Delta\rho(z)$ above the mid-plane and positive charge positioned in the center of $\Delta\rho(z)$ below, their interaction energy would be ~ 1.3 eV (the distance between charges is about 1.05 Å). Therefore, more than half of the binding energy is due to electrostatics while the other part is a consequence of the energy gain due to the orbital overlap.

After the analysis of the shape of $\Delta\rho$ it is evident that density is depleted mostly from the oxygen out of plane electronic orbitals as well as the metal states pointing towards the oxygen whereas the Ir states parallel to the surface accumulate electrons. This is a consequence of the interaction of iridium atomic orbitals with the valence p -band of the surface. The \mathbf{C}_{4v} symmetry of the system (surface plus the adsorbate) allows the interaction only between states with the same symmetry properties. Thus only the iridium s , d_{z^2} , d_{xz} and d_{yz} orbitals can interact with the filled $2p$ states of the Ir–bonded oxygen atom. In Fig.5.4 total and PDOS of the MgO surface prior and the full system after the interaction are presented,

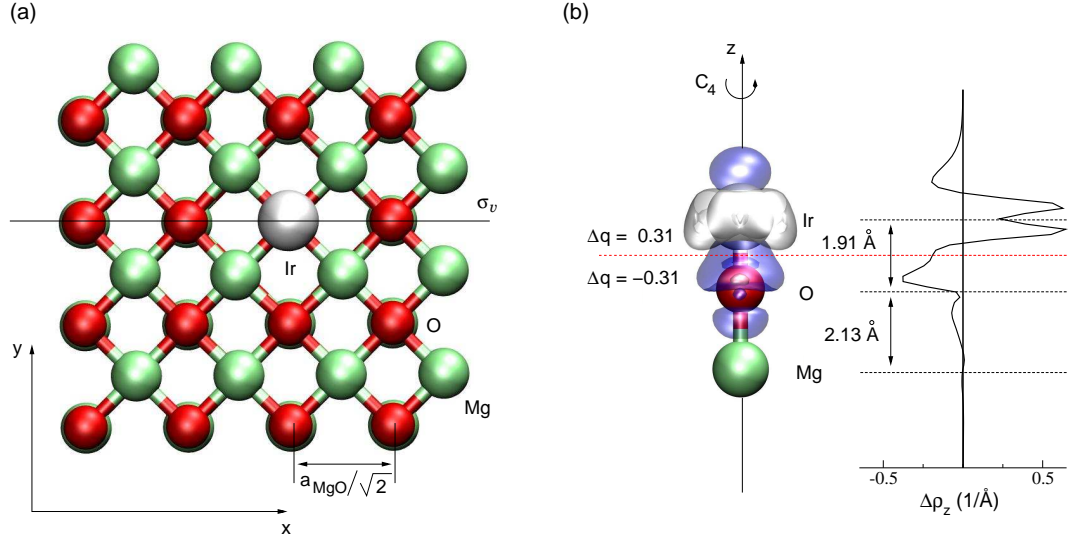


Figure 5.3: (a) Top view of the Ir adsorption geometry over MgO(100) surface. Full $4a_{\text{MgO}} \times 4a_{\text{MgO}}$ simulation cell is shown. (b) Side view of the adsorbed Ir atom, Ir-bonded O and bottom layer Mg atoms as well as the electron density difference $\Delta\rho$ (Eq.5.2). Bright isosurface indicates a density gain while blue one indicates density depletion. The isosurfaces are at $\pm 0.035 e/\text{\AA}^3$. The curve to the right is the in-plane integrated density difference $\Delta\rho_z$ whose integral below (above) the mid-plane, represented by the red dashed line, estimates total charge transfer Δq . Numbers in Å denote interatomic distances. Mirror plane σ_v and the C_4 rotations belonging to the C_{4v} symmetry group of the system are also presented.

respectively. Energy range which, for the oxide, is dominated by $2p$ and $2s$ states is displayed. MgO(100) surface without the adsorbate is "frozen" in the same atomic configuration as after the interaction. The PDOS clearly shows how the Ir $5d$ and $6s$ orbitals interact with the oxygen $2p$ ones. Deformation of the surface, that costs 0.33 eV, localizes p states of the Ir-bonded oxygen energetically at the top of the valence band. Most of their spectral weight is pushed by the interaction to the bottom and smaller portion to the top of the p band. The covalent type Ir-O bond is established. Bonding σ orbital, formed by the interaction of Ir $5d_{z^2}$ - $6s$ hybrids with O- $2p_z$ states, lays at the bottom of the new valence band. Next to it in the low energy part of the valence band the doubly degenerate π bonding orbitals are positioned. They are formed by the interaction of iridium $5d_{xz}$ and $5d_{yz}$ orbitals with $2p_x$ and $2p_y$ from the interacting O atom. Corresponding antibonding orbitals are pushed to the top of the valence band or above the Fermi energy. The weakly interacting $5d_{x^2-y^2}$ (with neighboring O atoms) and non-interacting $5d_{xy}$ iridium orbitals are positioned in the vicinity of the Fermi energy, slightly below the antibonding σ^* and π^* combinations. Interaction is the strongest between oxygen $2p_z$ orbital and iridium $5d_{z^2}$ - $6s$ hybrids. Thus, the charge transfer is mainly due to: (i) the antibonding σ^* state in the spin majority channel, pushed above the Fermi energy causes the electron transfer to the spin minority Ir orbitals parallel to the surface; and (ii) the Ir $5d_{xz}$ and $5d_{yz}$ orbitals in the spin minority channel that were empty prior the interaction become partly occupied because of the interaction with oxygen $2p_x$ and $2p_y$.

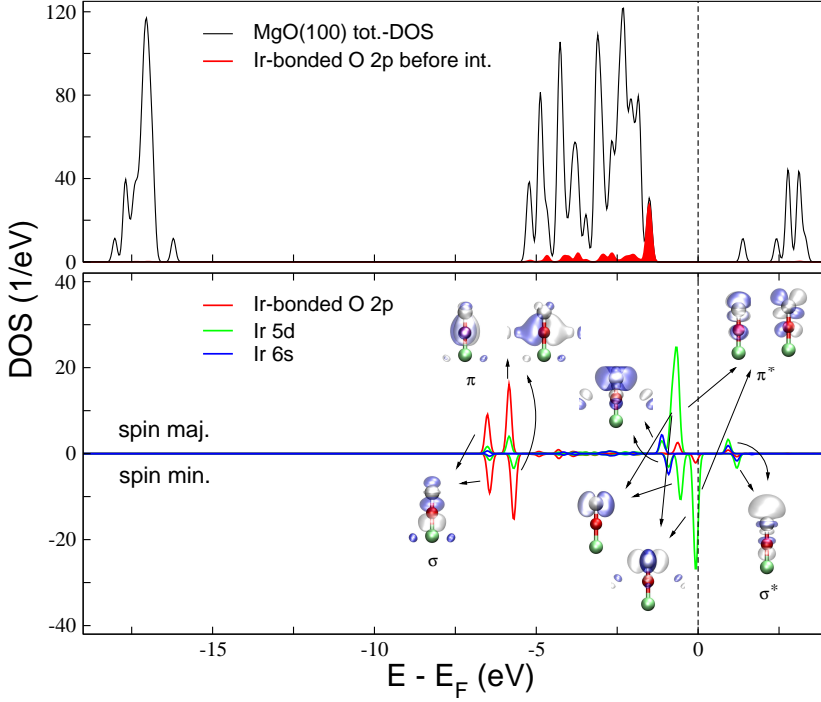


Figure 5.4: Total DOS of two layer MgO(100) slab (upper graph) "frozen" in its interacting atomic configuration for the Ir adsorption and spin-resolved projected DOS (lower graph) on Ir 5d and 6s as well as on Ir-bonded oxygen 2p atomic orbitals. Gaussian broadening of 0.1 eV is employed. The corresponding wavefunctions are also presented.

5.3 Adsorption of Ir₄ Clusters on MgO(100)

Interaction of the Ir₄ clusters with clean and defect-free MgO(100) surface is studied by placing the clusters, in their equilibrium gas-phase configurations, at the surface and performing the full geometry optimization. Many different adsorption geometries were carefully inspected for each of the three Ir₄ isomers, tetrahedral (**T**), butterfly (**B**) and square (**S**). Only results for the configurations with the lowest total energies are presented here. Details of the adsorption geometries as well as the relative energies of the three clusters are depicted in Fig.5.5.

More quantitative description of the adsorption geometries and energetics is given in Tab.5.2. Relative and binding energies, details of the electronic structure as well as the Ir coordination numbers and average distances for all iridium coordination shells up to 3.5 Å are given. As a coordination shell a group of distances to a specific type of neighbors spanned over the region not wider than 0.2 Å is considered⁵. Available experimental data from EXAFS measurements (references [118, 119]) are also shown for comparison. Calculated distances are presented for only those shells with coordination numbers larger than 0.25 and the standard deviation (from the corresponding average distance) smaller than 0.1 Å. This is due to the fact that static disorder (measured by the standard deviation), together with the thermal disorder and inelastic effects, reduces the amplitude of the associated electron backscattering wave in EXAFS measurements (see Appendix A).

Similarly to the adsorption of Ir atom all three Ir₄ isomers bind to the surface oxygen. **T** isomer forms three contact points to three oxygen atoms with a total cluster binding energy of 3.83 eV. One side of the basal Ir triangle is considerably elongated (~3.3 Å). The resulting configuration is similar to a butterfly geometry with two different Ir-Ir coordination shells

⁵Value taken from the Ref. [133]

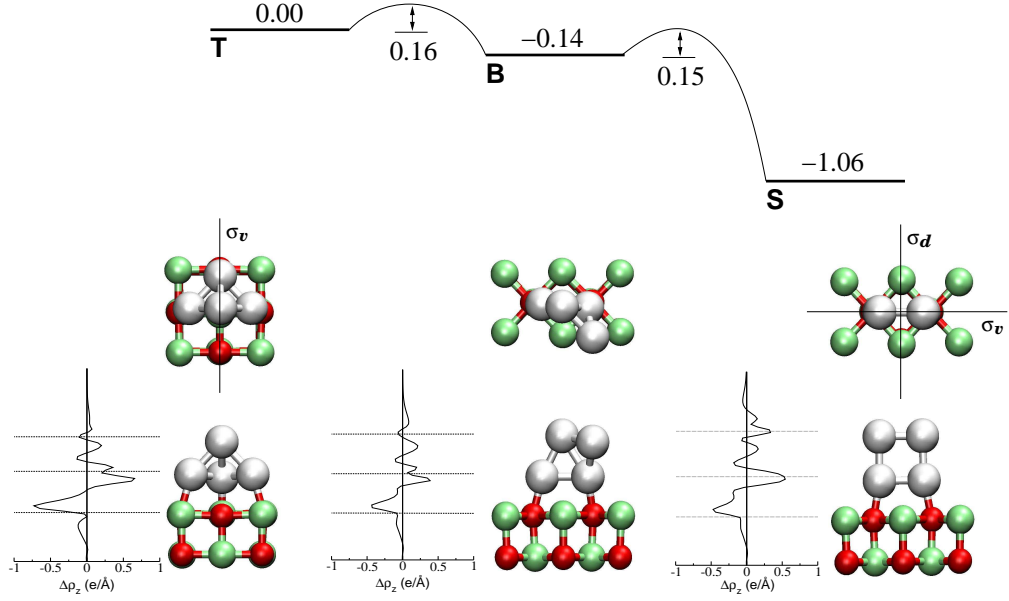


Figure 5.5: Top and side views of the atomic structures of the three Ir₄ isomers (**T**, **B** and **S**) adsorbed on defect-free MgO(100) surface. Numbers represent relative energies (in eV) calculated with respect to **T** configuration and the energy barriers for structural transformations between different isomers. The curves to the left of each configuration are the corresponding in-plane integrated density differences $\Delta\rho_z$. Symmetry operations of each configuration are also indicated.

whose coordination numbers are 2.5 and 0.5, and the corresponding average Ir–Ir distances 2.43 and 3.29 Å, respectively⁶. Angle between the "wings" of the deformed tetrahedron increases from the perfect tetrahedral value 70.52° to 106.4°. **T** isomer lowers its total energy by deforming (Tab.5.3). It relaxes due to the interaction with the surface in the direction of the gas-phase **B** structure ending in a configuration (not a gas-phase local minimum) that is for 0.28 eV lower in energy. Deformations also increase the magnetic moment of the cluster to 4 μ_B which is lowered to the value 3.46 μ_B upon adsorption.

The support relaxes as well increasing its total energy for 0.65 eV. Surface atoms neighboring to those which interact with the clusters move in-plane as well as out-of-plane for about several hundredths of an angstrom from their equilibrium positions at MgO(100). The interacting oxygen atoms and the Mg atom positioned below the cluster are displaced somewhat more, as shown in Fig.5.6.

Both **B** and **S** structures bind to defect-free MgO(100) surface with similar total binding energies of 3.35 and 3.33 eV, respectively. Hence, after the adsorption **S** isomer remains the most stable form of Ir₄. Both **B** and **S** interact with only two surface O atoms. Configurations where two isomers interact with more than two surface O atoms are not favorable due to the large mismatch between the surface O–O distance (3.01 Å) and the average bond lengths of the two isomers (2.35 and 2.31 Å for **B** and **S**, respectively). Interatomic distances in the two clusters are barely altered due to the interaction with the surface. Average Ir–Ir distances of **S** (**B**) isomer are 2.31 Å (2.38 Å) and 3.27 Å (3.68 Å) for the two Ir–Ir coordination shells,

⁶Since **T** isomer distorts noticeably upon adsorption, the term *tetrahedron* (or the **T** symbol), when speaking about supported clusters, refers to the lowest total energy configuration formed after the relaxation of the gas-phase **T** on the MgO surface.

Table 5.2: Calculated properties of **T**, **B** and **S** Ir₄ isomers adsorbed on MgO(100) surface. Total energy ΔE relative to that of **T** configuration, cluster binding energy E_b , total magnetic moment M , charge transfer Δq (in electrons), z -component of the induced dipole moment p_z , coordination number N , average distance R of the corresponding coordination shell for all shells up to 3.5 Å and all types of Ir neighbors (see the text for details). Available experimental data are also presented.

	ΔE [eV]	E_b [eV]	M [μ_B]	Δq [e]	p_z [D]	Ir-Ir		Ir-O		Ir-Mg		Ir-C	
						N	R[Å]	N	R[Å]	N	R[Å]	N	R[Å]
T	0.00	3.83	3.46	-0.50	-4.31	2.5	2.43	0.75	2.15	0.5	2.72		
						0.5	3.29			0.5	3.00		
										1.0	3.34		
B	-0.14	3.35	2.04	-0.34	-3.60	2.5	2.38	0.5	2.06				
						0.5	3.68						
S	-1.06	3.33	2.31	-0.38	-3.88	2.0	2.31	0.5	2.07	1.0	2.88		
						1.0	3.27			1.0	3.19		
Exp. Ref.[118]						2.6–3.1	2.62–2.73	0.6–1.1	2.07–2.16				
								2.5–3.0	2.59–2.73				
Exp. Ref.[119]						2.9	2.62	1.1	2.05	0.6	2.45	0.5	1.91

Table 5.3: Deformation energies $E_d = E_{deformed} - E_{ground\ state}$ (in eV) for the adsorption of Ir_4 clusters over $\text{MgO}(100)$. Values are for the three Ir_4 isomers (E_d^1) as well as for $\text{MgO}(100)$ support (E_d^2). $E_{int.}$ is purely electronic interaction energy (in eV) that can be calculated as the total cluster binding energy (Tab.5.2) plus the total deformation energy $E_d^1 + E_d^2$.

	$E_d^1(\text{Ir}_4)$	$E_d^2(\text{support})$	$E_d^1 + E_d^2$	$E_{int.}$
T	-0.28	0.65	0.37	4.19
B	0.10	0.63	0.73	4.09
S	0.03	0.52	0.55	3.88

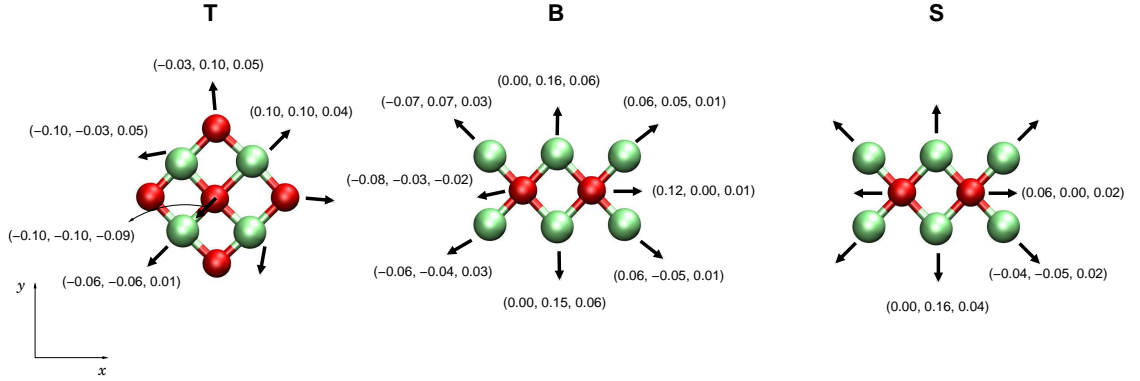


Figure 5.6: Deformations of $\text{MgO}(100)$ surface after the adsorption of the three Ir_4 isomers (**T**, **B** and **S**). Arrows denote displacements that are shown only for the interacting O as well as the neighboring Mg atoms. Numbers in parentheses are the (x, y, z) displacement vectors (in Å). They are given only for those atoms nonequivalent by symmetry.

respectively. Angle between the wings of **B** structure changes from the gas-phase 138.13° to 133.13° . This slight closing of **B** structure increases its energy by 0.1 eV. Distortions of the support, especially neighboring cations, are similar in both cases (Fig.5.6). Differences in deformation energies of the support come from different displacements of the interacting O atoms due to different symmetries of the two systems. Both clusters are magnetic upon adsorption, but while the magnetic moment of **B** is unchanged ($2.04 \mu_B$) with respect to its gas-phase value, moment of **S** structure is lowered to the value of $2.31 \mu_B$.

As in the case of free clusters, CINEB calculations showed that **S** isomer, the most stable form of $\text{Ir}_4/\text{MgO}(100)$, is not kinetically inaccessible starting from the other two. The numerical setup used for calculations is explained in Sec.2.2.5. The minimal energy path (MEP) for the transformation from **T** to **S** structure passes, similarly to the gas-phase MEP (Sec.3.4), through **B** configuration (see Fig.5.5). Activation energy for the transformation from **T** to **B** is calculated to be 0.16 eV while from **B** to **S** 0.15 eV is needed. However, main features of the transformations between **T** and **B** structures are different. One Ir–Ir bond of **T** structure between the two basal Ir atoms is already broken. Therefore, to transform into **B** configuration only one Ir–O bond is needed to brake. The activation of that Ir–O bond needs similar energy as one Ir–Ir bond in the gas-phase. The fact that very low energy is required for activation of the Ir–O bond can be attributed to the stronger bonding (binding energy per Ir–O bond is 1.28, 1.68 and 1.67 eV for **T**, **B** and **S**, respectively) of both **B** and **S** isomers to the surface. Activation energy of the Ir–O bond of **T** structure is to a good extent

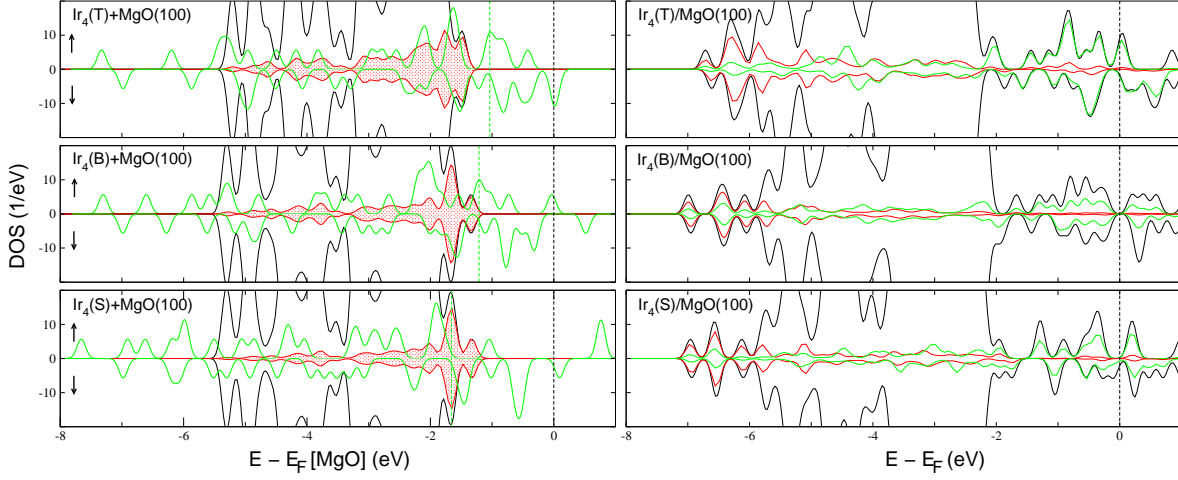


Figure 5.7: Left panel: spin resolved total DOS of Ir_4 in the **T**, **B** and **S** configurations (green curves) together with the total DOS of $\text{MgO}(100)$ surface (black) aligned on the same vacuum level. dashed lines denote the Fermi energy of the corresponding (of the same color) DOS. Projections on $2p$ orbitals of the Ir-bonded surface O atoms are shown in red. Clusters and the supports are "frozen" in their interacting configurations. Right panel: Total DOSs of the corresponding systems after the interaction. Projections on $2p$ and $5d$ orbitals of the interacting O and Ir atoms are shown in red and green, respectively.

compensated by the energy gain due to the strengthening of other two and the energy of the transition state is low. For further transformation along the MEP from **B** towards **S** isomer there is only one Ir-Ir bond that breaks, as in the gas-phase, which requires similar activation energy. Finally, the same conclusion can be drawn that at room temperature, both **T** and **B** configurations supported by defect-free $\text{MgO}(100)$ remain metastable structures with a short lifetime.

Even though the gas-phase energy ordering of the three isomers remains the same upon adsorption, relative stability is considerably changed. As a consequence of different binding, relative energies of **S** and **B** isomers, calculated with respect to **T** one, are lower for 0.42 and 0.44 eV, respectively. If the interaction with the surface is divided in two contributions (*i*) deformations and (*ii*) purely electronic interaction; it can be shown that a good part of the reduction in relative energies comes from the different deformation energies of the three clusters. When differences between adsorption of **T** and **B** isomers are analyzed it can be seen that only a small portion (0.1 eV) of the change in their relative energy is due to purely electronic effects (Tab.5.3). This results from the unusual, negative deformation energy of **T** isomer.

From the analysis of the electronic structure of the three isomers (Fig.5.7) it follows that main features of the electronic interaction between the three isomers and $\text{MgO}(100)$ surface are similar to those of Ir atom. Clusters interact mainly with the states from the surface valence band and the charge is transferred from the surface to the adsorbates. The charge transfer is estimated in the same way as explained in previous section. Due to the bigger number of interacting O atoms **T** isomer interacts with bigger number of O- $2p$ orbitals (surface under the red curves on the left panel of Fig.5.7). This results in bigger charge transfer as well as larger surface dipole moment (Tab.5.2). However the electronic interaction is only by 0.1 and 0.27 eV stronger than that of **B** and **S** isomers, respectively. This can be attributed to

more favorable overlap of the molecular orbitals of **B** and **S** isomers with the states on the surface. Somewhat stronger interaction of **B** compared to **S** is mainly due to the different cluster symmetry and differences of the molecular orbitals near the Fermi energy.

From Tab.5.2 it is clear that geometry of none of the MgO(100) supported Ir₄ isomers corresponds well to experiment. Intriguing is the fact that geometry of **T** configuration, predicted theoretically to be the least stable, is the closest to the experimental situation. It has the biggest Ir–Ir first shell coordination number and the longest Ir–Ir bond length. However, contributions coming from the second Ir–Ir shell are not measured and the calculated Ir–Ir distances are noticeably shorter than those reported from experiments.

When comparing theoretical results with those obtained by EXAFS it is necessary to take into account that the errors of EXAFS are not small. They are estimated to $\sim 10\%$ for the coordination numbers and about 0.02 Å for the distances coming from the metal–metal contributions. For low-*Z* scatterers (carbon, oxygen,...) these errors can be even bigger [124]. Differences from the calculated results may also arise from temperature effects since the EXAFS spectra are recorded at room temperature. Finally, there are also differences between different measurements that are dependent on the preparation procedure of the substrate. In Ref.[118] each coordination shell is characterized by a range of values depending on the calcination temperature of the substrate. No contribution from the Ir–Mg and Ir–C shells is reported. In a more recent publication [119] the same authors measure different longer Ir–O contribution as well as the contributions coming from the Ir–Mg and Ir–C shells. The latter could come either from the non-desorbed CO ligands (partial decarbonylation)⁷ or from the standalone C adatoms. As it is already shown for the gas-phase clusters (references [69, 70] and Chapter 4) and will be confirmed also for the MgO supported species (Sec.6.1 and Ref.[69, 70]) one C adatom is sufficient to stabilize **T** configuration.

5.4 Diffusion of Ir₄ Clusters on MgO(100) Surface

Diffusion of supported atoms or small clusters is an important issue in understanding the processes related to their deposition. Low barriers for diffusion lead to aggregation of the supported species and island formation (sintering). In this case defects at surfaces act as the nucleation centers due to their ability to trap adsorbates. It has been found recently that small palladium clusters are highly mobile on MgO(100) surface [120, 121]. Moreover, by varying external parameters during the preparation procedure of MgO(100) supported Ir₄ clusters signs of aggregation have been discovered when the supported clusters were treated in He gas at temperatures above 400° C [123].

According to the results presented for clean Ir₄ clusters adsorbed over defect-free MgO(100) surface (previous section) it makes sense to study diffusion only of **S** isomer. It is found in this work that any adsorption configuration of the other two isomers, different from those adsorption geometries shown in Fig.5.5 lays much higher in energy than the transition states for the structural transformations to **S** structure. Therefore, for **T** and **B** isomers it is energetically more favorable to transform to **S** configuration than anything else.

On the other hand, for **S** to diffuse over MgO(100) surface several possibilities exist: (*i*) to move, keeping the same plane normal to the surface, to the configuration with only one

⁷The same Ir–C and long Ir–O coordination numbers go in line with this assumption, but in that case the CO bond would be considerably elongated (~ 1.4 Å) which is not confirmed by our calculations and/or other measurements.

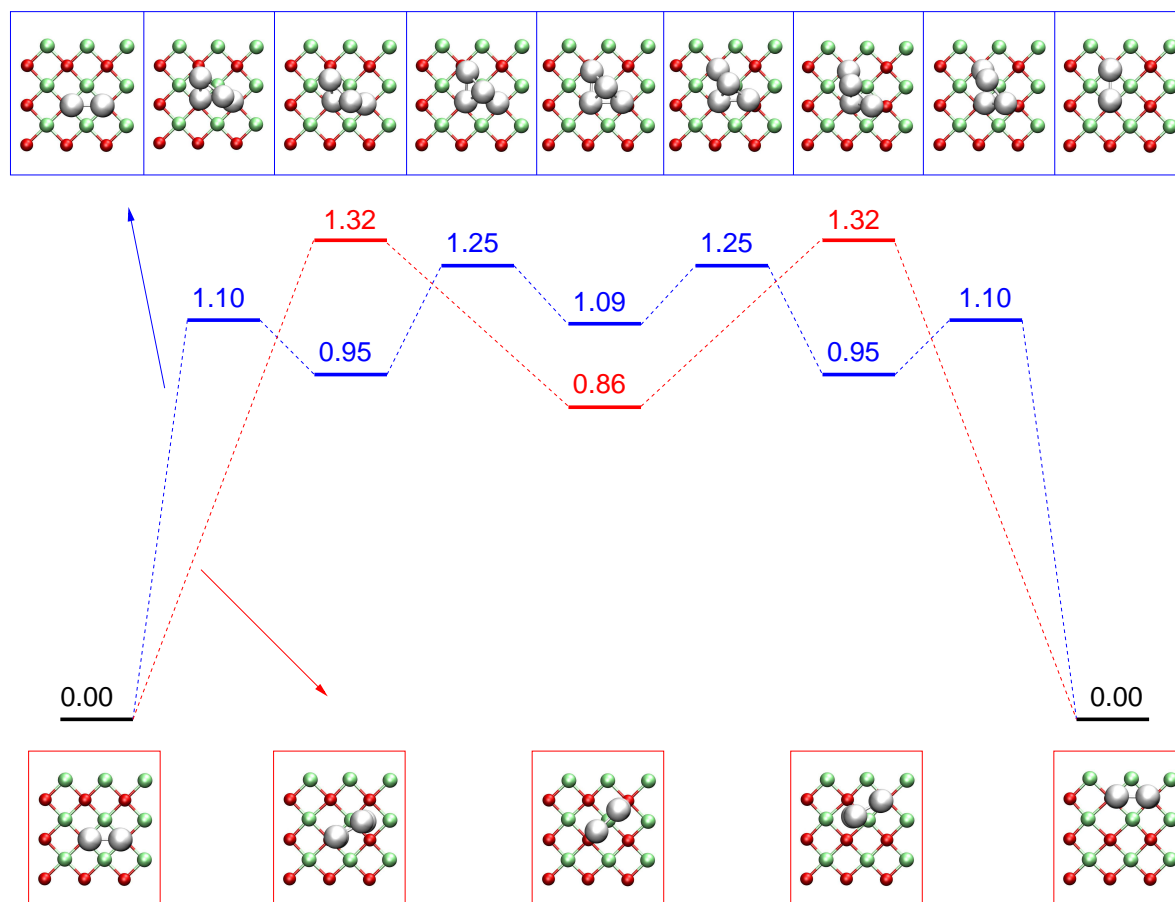


Figure 5.8: Energy diagram for the two diffusion pathways (blue and red) of Ir_4 in **S** geometry. Both pathways have the same initial and equivalent final states. All numbers are given in eV. The corresponding atomic configurations are also shown.

Ir in contact with the surface oxygen and then to continue "rolling" in the same direction to the next second O atom; (ii) to transform to geometry parallel to the surface and then to straighten itself up to the same configuration as the starting one, but now in contact with two different surface O atoms; (iii) to transform to the configuration with **S** structure also straighten up interacting with two surface oxygen atoms, but with one Mg atom below the cluster and then to continue to the configuration equivalent to the starting one with one of the interacting surface O atoms different from those at the beginning (cluster walk); and finally (iv) to transform from the same starting to the equivalent final configuration as under (iii) but not preserving the square shape and passing through **B**, **T** and then again **B** configuration. It turns out that the energies of the intermediate configurations along the pathways (i) and (ii) are by 1.42 and 2.39 eV higher than that of the most stable **S** adsorption geometry, respectively. On the other hand, the intermediate configuration for the transformation (iii) (**S** isomer positioned above one surface Mg atom interacting with two oxygen atoms) lays only 0.86 eV above the most stable **S** adsorption configuration. Calculated energy barrier for the structural transformation along the pathway (iii) is 1.32 eV. Transition state lays in the configuration with one Ir atom in contact with the surface and the other in-between the two potentially interacting O atoms. Calculated activation energy for the diffusion channel (iv) is

1.25 eV⁸ and is simply the energy needed to go backwards from **S** to **B** and **T** configurations⁹.

In Fig.5.8 energies of the stable configurations as well as of the transition states for the transformations (iii) and (iv) are shown together with the corresponding geometries. All energies are presented relative to the most stable **S** adsorption configuration (initial and final). According to the calculated energy barriers these two diffusion channels are relevant for the Ir₄ clusters supported by MgO(100). The temperatures that could activate the diffusion can be estimated using Eq.2.19. The prefactor (attempt frequency) in Eq.2.19 is of the order of 10¹²–10¹³ Hz since the highest vibrational frequencies of Ir clusters are ~30 meV (~10¹² Hz) and it is known that vibrations of MgO(100) surface lay below 88 meV (~10¹³ Hz) [122]. Both barriers of 1.25 and 1.36 eV are not small and for the temperature of 300° C the rate constants for the two processes are in the range 1–10 Hz. With these rate constants the average half-life for diffusion of **S** configuration is ~0.07–0.7 s. This is not much, since the probability of returning to the same starting configuration after two cycles is the same as displacing further, which reduces considerably the number of clusters that pass a certain distance. If the temperature increases to 400° C rate constants become two orders of magnitude higher 100–1000 Hz which significantly changes the timescale for the diffusion (half-life is 0.0007–0.007 s). Increasing further the temperature from 400° C the half-life decreases rapidly. This result is in a good agreement with experimental findings [123] and confirms that Ir₄ clusters prepared at and below 300° C should be well separated, while the aggregation can be expected at higher temperatures.

5.5 Adsorption of Ir₄ Clusters on MgO(100) Surface With a Neutral and Positively Charged Oxygen Vacancy

As in previous section, properties of only the most stable adsorption configurations for each of the three Ir₄ isomers on MgO(100) surface with neutral (F) as well as with positively charged oxygen vacancy (F⁺ center) are presented here (Fig.5.9). Modelling of the defected surface is already explained in Sec.5.1.1.

The three isomers bind stronger to the neutral vacancy site than on defect-free MgO(100) surface. Stronger binding of *d*-metals to the O vacancy than at defect-free MgO(100) surface is a well known feature [125] that is attributed to the charge transfer from the support to the adsorbate. Again **T**, the least stable gas-phase structure, binds with the highest binding energy of 6.32 eV followed by **B** and **S** with binding energies of 5.21 and 5.06 eV, respectively (Tab.5.4). Increase in binding energies is the biggest for **T** isomer (2.49 eV), while this shift amounts to 1.86 and 1.73 eV for **B** and **S** structures, respectively. The Energy ordering is now different. The most stable isomer is still **S** with the total energy for only 0.25 eV lower than **T** while **B** isomer becomes the least stable structure with the energy for 0.53 eV higher than **T** configuration.

The adsorption geometries are similar to those at the defect-free surface and can be obtained by removing one of the interacting O atoms (with additional relaxations). At a variance to the adsorption of **S**, where there are two equivalent (by symmetry) interacting O

⁸One could also imagine a two step process **S**→**B**→**T** which would require 1.10 eV. However, the probability of going from the intermediate **B** backward to **S** is much higher than going forward. Therefore, the rate constants are determined by the highest transition state which is 1.25 eV above the initial configuration.

⁹Already calculated for the purpose of investigation of the relative stability of the three isomers and presented in Sec.5.3.

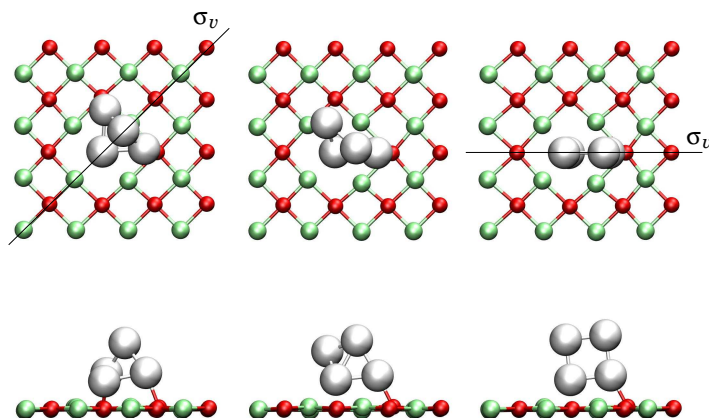


Figure 5.9: Top and side views of the most stable adsorption configurations of the three Ir₄ isomers **T**, **B** and **S** at MgO(100) surface with neutral oxygen vacancy. Only the topmost MgO layer is shown. Color scheme is the same as in Fig.5.3. Mirror planes, the only symmetry operations, are also displayed. Upon charging the vacancy configurations remain similar to the displayed ones.

atoms, in the cases of **T** and **B** two possibilities exist. The most stable adsorption configuration of **T** is obtained by removing the oxygen atom that lays at the σ_v mirror plane. In case of **B** the vacancy lays next to the oxygen that interacts with one of the wing-tip iridium atoms (Fig.5.9). Structures of all three isomers relax from their configurations when adsorbed on the defect-free surface bringing the Ir atom, that was interacting with the missing oxygen, closer to the vacancy. These relaxations are very close to a rigid shift of atomic positions towards the vacancy for both **B** and **S**. Average Ir–Ir distances associated to the two coordination shells of both **B** and **S** are only slightly bigger (Tab.5.4) than at defect-free MgO(100) surface. The angle of **B** structure is also only slightly changed to the value of 131.9°. On the other hand **T** distorts considerably. Distances between the two basal Ir atoms which interact with the remaining oxygen atoms are somewhat smaller (3.20 Å) as well as distances between them and the two other Ir atoms (average value is 2.41 Å). Distortion comes from the motion of the Ir atom, that interacts with the vacancy, towards the vacancy elongating the distance to the topmost Ir atom to the value of 2.75 Å. Therefore the coordination number of the first Ir–Ir shell is lowered to 2 and another shell appears with coordination number 0.5 due to the distortion. Again, the deformation lowers the energy of **T** structure (Tab.5.5), but now for 0.18 eV, while the energy of **B** isomer is 0.1 eV higher and the energy of **S** does not change its gas-phase value.

The Ir–O distances in all cases remain unchanged (they are smaller only for 0.01 Å). This is mainly due to the relaxation of the support. While the magnitude and directions of these relaxations for **T** adsorption are almost the same as of the defect-free surface leading to the similar deformation energy, relaxations of the support for the adsorption of **B** and **S** isomers are bigger. Therefore, the relaxations of the defected MgO(100) surface in the two cases (adsorption of **B** and **S**) are more expensive as shown in Tab.5.5. Magnetic moments of the clusters are also affected by the vacancy and while moment of **T** isomer increases for 1.19 μ_B this change is +0.56 and +0.28 μ_B for **B** and **S**, respectively.

Binding of the Ir₄ clusters to the charged vacancy is weaker than to the neutral one, but while the binding energy of **T** structure decreases by only 0.16 eV, binding energies of **B** and **S**

Table 5.4: Calculated properties of **T**, **B** and **S** Ir₄ isomers adsorbed in the vicinity of the oxygen vacancy (F and F⁺ centers) at MgO(100) surface. Cluster binding energies E_b, total energy ΔE relative to that of **T** configuration, total magnetic moment (M), z-component of the induced dipole moment p_z, coordination number (N), average distance (R) of the corresponding coordination shell for all shells up to the distance of 3.5 Å and all types of neighbors.

		ΔE [eV]	E _b [eV]	M [μ_B]	p _z [D]	Ir-Ir		Ir-O		Ir-Mg	
						N	R[Å]	N	R[Å]	N	R[Å]
Ir ₄ /F	T	0.00	6.32	4.67	-4.13	2	2.41	0.5	2.14	2	2.74
						0.5	2.75			1	3.38
						0.5	3.20				
	B	0.53	5.21	2.60	-3.62	2.5	2.42	0.25	2.01	1.5	2.76
						0.5	3.63			0.75	3.38
	S	-0.25	5.06	2.59	-3.96	2	2.32	0.25	2.06	1.5	2.75
Ir ₄ /F ⁺	T	0.00	6.16	2.69	-3.59	2	2.38	0.5	2.04	2	2.79
						0.5	2.70			1	3.43
						0.5	3.24				
	B	0.79	4.79	2.86	-3.02	2.5	2.42	0.25	1.93	0.5	3.46
						0.5	3.60				
	S	0.01	4.64	3.44	-3.09	2	2.32	0.25	1.98	1	2.73
						1	3.28			0.5	2.98
										0.5	3.48

isomers drop as much as 0.42 eV for both structures. The energy ordering of the three isomers changes even more. Two structures **T** and **S** become almost degenerate (they differ by 0.01 eV in favor of **T**) and the difference to the least stable **B** isomer further increases to 0.79 eV. It can be seen from Tab.5.5 that **T** isomer lowers its energy by relaxing for remarkable 0.40 eV (change of -0.22 eV compared to adsorption at neutral vacancy). The Ir-Ir distances of **T** cluster are now shorter while the two basal Ir atoms that interact with two oxygen atoms become further apart (Tab.5.4). However, this gain is compensated by the stronger relaxation of the support and somewhat weaker (by 0.1 eV) electronic interaction leading to the small net decrease in the total cluster binding energy.

Although the ~0.4 eV drop in binding of **B** and **S** isomers is the same it has different origin. While in case of **B** it comes from bigger support relaxations, for **S** isomer this difference comes from electronic effects (Tab.5.5). Both clusters do not relax almost at all, but at variance to the support deformations in case of **S** which are more similar to those of the neutral vacancy, the support relaxes considerably in case of **B** isomer. This is predominantly due to the relaxation of the remaining interacting O atom which is displaced in case of **B** (**S**) for 0.35 (0.26) Å in *x* direction (Fig.5.10) and 0.22 (0.18) Å out of plane. This increases the deformation energy of the support in case of **B** for 0.5 eV which is very close to the difference of binding to the neutral vacancy.

The magnetic moments of the three isomers are also influenced by the charging. The moment of **T** structure is lowered for almost 2 μ_B upon charging and moments of the **B** and **S**

Table 5.5: Deformation energies $E_d = E_{deformed} - E_{ground\ state}$ (in eV) for the adsorption of Ir_4 clusters over $\text{MgO}(100)$ with the neutral (F) and charged (F^+) O vacancy. Values are for the three Ir_4 isomers (E_d^1) as well as for $\text{MgO}(100)$ support (E_d^2). $E_{int.}$ is purely electronic interaction energy (in eV) that can be calculated as the total cluster binding energy (Tab.5.4) plus the total deformation energy $E_d^1 + E_d^2$.

	F				F^+			
	$E_d^1(\text{Ir}_4)$	$E_d^2(\text{support})$	$E_d^1 + E_d^2$	$E_{int.}$	$E_d^1(\text{Ir}_4)$	$E_d^2(\text{support})$	$E_d^1 + E_d^2$	$E_{int.}$
T	-0.18	0.66	0.48	6.80	-0.40	0.93	0.53	6.69
B	0.10	0.93	1.03	6.24	0.04	1.43	1.47	6.26
S	0.00	0.83	0.83	5.89	0.00	0.87	0.87	5.51

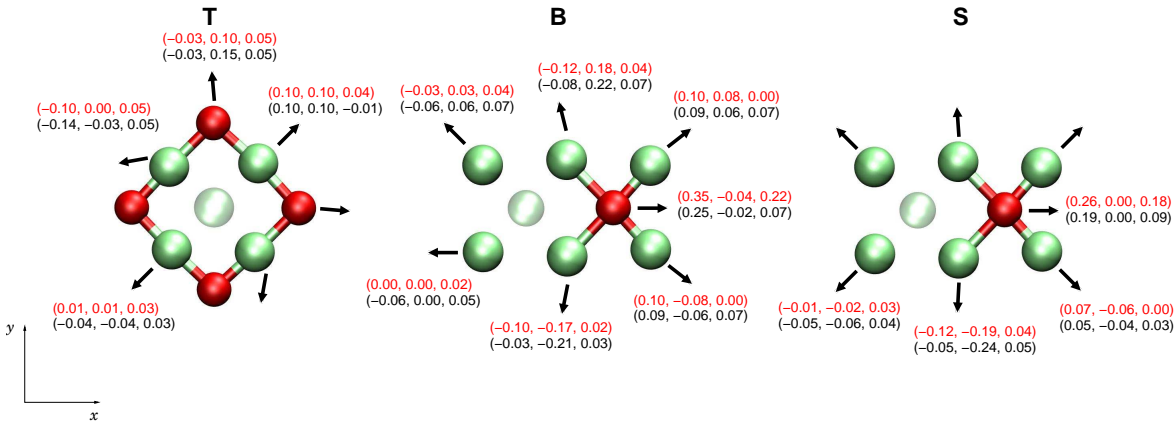


Figure 5.10: Deformations of the MgO surface with neutral and charged O vacancy caused by the adsorption of the three Ir_4 isomers (**T**, **B** and **S**). Arrows denote displacements that are shown only for the interacting O as well as the neighboring Mg atoms. Numbers in parentheses are the (x, y, z) displacement vectors (in Å). They are given only for those atoms nonequivalent by symmetry. Black color is used for the displacements in the case of neutral while displacements in the case of charged vacancy are given in red.

are bigger by 0.26 and $0.85 \mu_B$, respectively. These changes can be attributed to the removal of an electron (charging) from different spin states of the three isomers and smaller portion to the electron transfer, upon charging, between the two spin channels.

The electronic effects of the neutral (as well as charged) O vacancy in the cases such as these, where vacancy introduces only relaxations of the same adsorption geometries as at the defect-free MgO surface, can be understood by analyzing changes in the electronic structure of the support and how it influences the interaction with adsorbates. Instead of having three oxygen $2p$ orbitals at the site from which the O atom is removed, there is only one surface state. This state is totally symmetric with respect to the site symmetry of the missing oxygen (in this case C_{4v} point group) as shown in Fig.5.1. It is shifted in energy compared to the analogous state (totally symmetric $2p_z$) of the missing oxygen, and its charge distribution is different as well. However, due to the relaxations, overlap of molecular orbitals of the Ir_4 isomers with the state in the vacancy remains similar, for all three isomers, to the that with the $2p_z$ orbital of the missing oxygen. The fact that surface dipoles remain almost the same upon creating the vacancy goes in line with this assumption, since, as shown for the Ir adsorption (Sec.5.2), charge transfer occurs from the states perpendicular to the surface

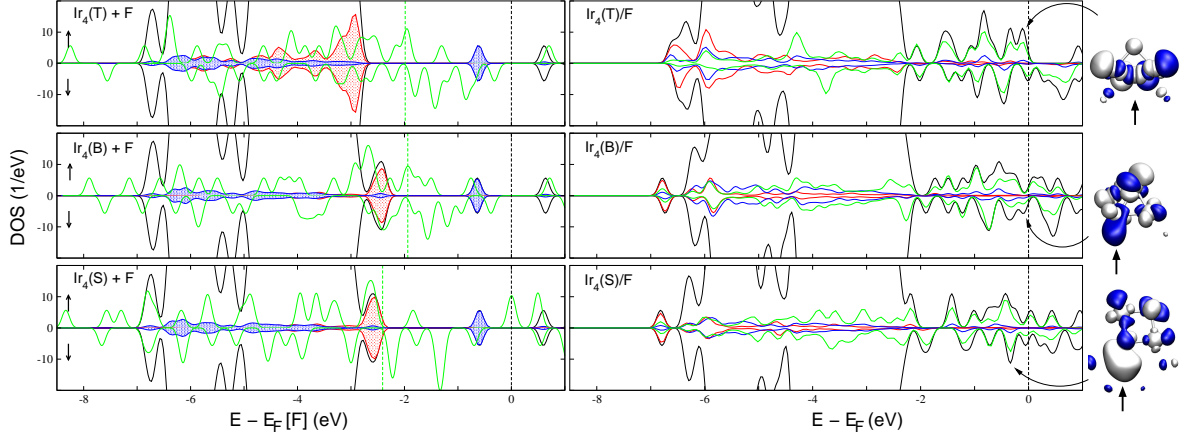


Figure 5.11: Left: spin resolved total DOS of Ir_4 in the **T**, **B** and **S** configurations after the deformations (green curves) together with the total DOS of deformed $\text{MgO}(100)$ surface with neutral O vacancy (black). DOSs are aligned on the same vacuum level. Dashed lines denote the Fermi energy of the corresponding (of the same color) DOS. Projections on $2p$ orbitals of the Ir-bonded surface O atoms and on $2p$ and $3s$ orbitals of Mg atoms surrounding the vacancy are shown in red and blue, respectively. Right panel: Total DOSs of the corresponding systems after the interaction. Projections on the interacting O $2p$, Mg $2p$ and $3s$ as well as Ir $5d$ orbitals are shown in red and green, respectively. On the far right the electronic states that are emptied upon charging the vacancy are displayed (only the Ir atoms are shown). Arrows denote position of the vacancy as well as the position of each state in the corresponding spectrum.

(totally symmetric) to the Ir orbitals parallel to it. The charge transfer is responsible for the increase in binding energies of all three clusters since it lowers considerably the repulsive Coulomb interaction between the two electrons localized inside the vacancy.

Creation of the vacancy affects, above all, the interaction of the cluster molecular orbitals with $2p_x$ and $2p_y$ states that are now missing. What really makes the difference between the electronic interaction of the three clusters (Tab.5.5) is the number of remaining surface states available for bonding. In case of **S** isomer the number of O- $2p$ orbitals decreases from 9 to 7 (22 % change) while in the other two it goes from 6 to 4 (33 %) upon creating the vacancy. In Fig.5.11 DOSs of the subsystems (clusters and the support) prior and of the full system after the interaction are shown. The vacancy state appears in the band-gap of the surface, as already explained in Sec.5.1.1. It interacts mainly with the molecular orbitals of the three isomers close to the Fermi energy. The difference in the number of O- $2p$ states that are interacting with the three isomers is clear. The 0.35 eV difference in electronic interaction between **B** and **S** can be again attributed to the lower symmetry of the **B** isomer and the ability of its molecular orbitals to hybridize.

Upon charging, electronic interaction of both **T** and **B** isomers remains almost the same as when adsorbed to the neutral vacancy (Tab.5.5), while it further decreases in case of **S**. This can also be understood by analyzing electronic structure of the three systems. There is, due to similar geometry, one-to-one correspondence between electronic orbitals of the clusters adsorbed to the neutral and charged O vacancy. Then, charging of the vacancy can be viewed as removal of an electron from one of the states of the system when the cluster is adsorbed at the neutral vacancy site. On the far right in Fig.5.11 electronic orbitals, for each adsorbed isomer, from which the electron is removed are shown as well as their position in the

corresponding spectrum. Differences come from different character of those orbitals. In case of **T** the most favorable option is to remove an electron from a state, which almost does not interact with the surface. Induced relaxations of the cluster and the support cancel leading to only slightly changed electronic interaction energy (~ 0.1 eV). On the other hand in case of **B** the state is a weak bonding cluster–vacancy combination, while the corresponding state of **S** structure has the same, but much more pronounced bonding character. Small reduction in binding of **B** to the vacancy is compensated by strengthening other interaction channels due to bigger deformations of the surface resulting in the same electronic interaction energy. This is not the case for **S** isomer whose electronic interaction decreases for ~ 0.4 eV. In addition, charging is followed by a certain electron transfer between the spin channels for both **T** and **B** systems.

When comparing theoretical results for the three clusters adsorbed at the defected MgO(100) surface (Tab.5.4) with EXAFS measurements (Tab.5.2) it is evident that disagreement becomes even bigger. Calculated Ir–Ir distances are still too short and the Ir–O coordination numbers do not agree at all. Although, by introducing the vacancy relative stability of the three Ir₄ isomers is considerably affected, **T** structure becomes very close in energy to **S** at the neutral and degenerate at the charged vacancy, the distortions are so strong that it would not be possible to identify it in experiments as a tetrahedral-like any more.

5.6 Adsorption of Ir₄ on TiO₂(110)

Several experimental studies on adsorbed iridium nanoparticles and small Ir clusters on the surfaces of both anatase and rutile TiO₂ have been performed recently [126, 10, 11]. Various techniques are used for preparation and characterization such as decarbonylation of Ir₄(CO)₁₂ carbonyl molecules dispersed on TiO₂ powder (mixture of rutile and anatase phases) and EXAFS spectroscopy [126], size and energy-selected deposition of Ir_n⁺ ($n = 1, 2, 5, 10, 15$) clusters on rutile TiO₂(110) and X-ray photoelectron spectroscopy (XPS) [10] or the vapor-deposition of Ir nanoparticles also on rutile TiO₂(110) and scanning tunneling microscopy (STM) [11]. The authors did not observe any aggregation of the Ir clusters. Moreover, there is no oxidation/reduction reactions at the surface–cluster interface [10] similarly to the adsorption of other transition metals on TiO₂(110) surface (see reference [106] and the references therein). This is also supported by theory which does not predict any significant charge transfer between the stoichiometric surface and adsorbed late transition metal atoms [127, 128].

Similar kind of analysis as for MgO(100) (Sec.5.2) for the adsorption of atomic Ir on the TiO₂ surface has been carried out. Convergence tests showed that the theoretical model presented in Sec.5.1.2 (unit cell size, slab and vacuum thickness, **k**-point sampling, ...) describes well the adsorption of atomic Ir. Equilibrium adsorption geometries of Ir₄ clusters on TiO₂(110) surface are obtained in the same way as for adsorption on MgO(100) support (Sec.5.3). Details of the adsorption energetics, electronic structure and geometries of the three Ir₄ isomers (**T**, **B** and **S**) are presented in Fig.5.12 and Tab.5.6. Due to the large differences in the binding energies of the three isomers their relative stability is considerably altered. The **S** isomer is now only by 0.03 eV more stable, while **B** structure becomes 0.22 eV higher in energy than **T**. The difference of 0.03 eV is very small and therefore **T** and **S** structures may be considered as two degenerate Ir₄/TiO₂(110) configurations. Magnetic moment of **S** isomer is reduced from the gas-phase $8 \mu_B$ to $0 \mu_B$, while **T** and **B** structures retain their gas-phase

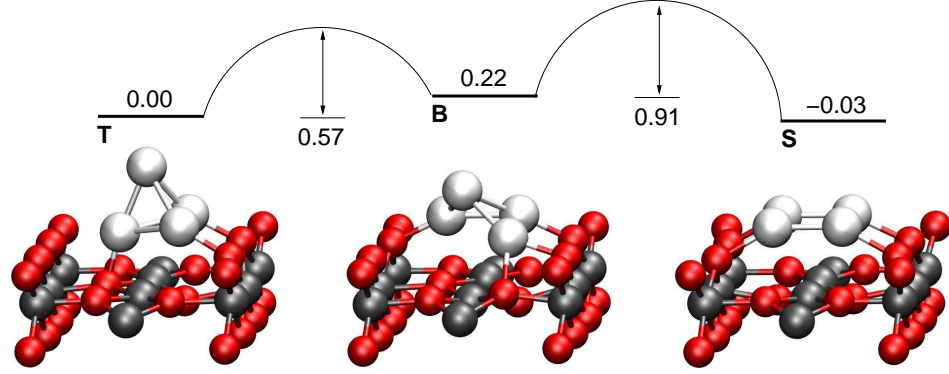


Figure 5.12: Equilibrium atomic configurations of **T** and **S** Ir₄ isomers when adsorbed on stoichiometric TiO₂(110) surface. Numbers above each structure denote corresponding total energies calculated with respect to **T** isomer. Energy barrier for the transformation between the two Ir₄ structures is also shown.

magnetization upon adsorption of 0 and 2 μ_B , respectively.

Geometries of **T** and **S** isomers are not altered much by the adsorption. Their average Ir–Ir distances are elongated only by 0.03 Å. Consequently their deformation energies are also small and amount to 0.11 and 0.17 eV, respectively (Tab.5.7). These deformations do not influence the gas-phase magnetization of the two isomers. On the other hand **B** structure relaxes somewhat more. The average bonding Ir–Ir distance is longer by 0.08 Å and angle between the two wings is reduced to 127.68° (gas-phase value is 138.13°). This has almost no effect on the distance between the two wing-tip Ir atoms that are separated by 3.74 Å, very similar to the gas-phase 3.79 Å. The energy needed for the deformation of **B** isomer is also bigger (0.29 eV) and its gas-phase magnetic moment increases to 4 μ_B due to the deformation. It decreases back to 2 μ_B upon interaction of the deformed cluster with the TiO₂ surface.

On the other hand, adsorption of the three Ir₄ isomers induces considerable relaxations of TiO₂(110) surface, much bigger than defect-free MgO(100) (Sec.5.3). The surface bridging O atoms that interact with the clusters (Fig.5.12) move parallel to the surface approaching the three adsorbates (**T**, **B** and **S**) by, on average 0.18, 0.20 and 0.23 Å, respectively. At variance to **S** which interacts only with bridging O atoms, **T** and **B** isomers interact also with one of the basal O atoms that is displaced by the interaction by 0.2 and 0.26 Å vertically out of the surface, respectively. In all three cases the nearby Ti(5c) atoms positioned below the three isomers move up from the surface. While for the adsorption of **T** and **S** isomers there are two cations which are displaced about 0.2 Å, in case of **B** only one Ti atom relaxes considerably, by 0.3 Å in the same direction. The neighboring basal O atoms positioned below the adsorbates at the distance ~ 2.9 Å (just one in cases of **T** and **B** and two in for **S** adsorption) are pushed into the surface by ~ 0.5 Å. The surface relaxations can be attributed to two main reasons: (i) chemical bonding between the three clusters and bridging O atoms and (ii) the electrostatic interaction between the Ti(5c) and basal O atoms that are in the high oxidation states and the charge from the clusters accumulated in the interfacial region.

Table 5.6: Calculated properties of **T**, **B** and **S** Ir₄ isomers adsorbed on stoichiometric rutile TiO₂(110) surface. Cluster binding energies E_b , total energy ΔE relative to that of **T** configuration, total magnetic moment M , z -component of the induced dipole moment p_z calculated using Eq.5.1, coordination number N , average distance R of the corresponding coordination shell for all shells up to the distance of 3.5 Å and all types of neighbors. Available experimental data are also presented.

	ΔE [eV]	E_b [eV]	M [μ_B]	p_z [D]	Ir-Ir		Ir-O		Ir-Ti	
					N	$R[\text{\AA}]$	N	$R[\text{\AA}]$	N	$R[\text{\AA}]$
T	0.00	5.58	0.00	2.37	3.0	2.47	0.75	2.02	1.0	2.65
							1.5	2.93	0.75	3.21
							0.75	3.29		
B	0.22	4.78	2.00	1.67	2.5	2.44	1.0	2.10	0.75	2.55
									1.25	3.21
S	-0.03	4.10	0.00	1.16	2.0	2.34	1.0	2.16	1.0	2.65
					1.0	3.30	2.0	2.92	1.0	3.32
Exp. ¹					3.3	2.68	0.9	2.05	0.7	2.75
							1.2	3.21		

¹ Values taken from Ref.[126]

Table 5.7: Deformation energies $E_d^1(\text{Ir}_4)$ and $E_d^2(\text{TiO}_2)$ of the three Ir₄ isomers (**T**, **B** and **S**) and TiO₂(110) surface are shown together with the electronic interaction energies $E_{int.}$. All values are in eV.

	$E_d^1(\text{Ir}_4)$	$E_d^2(\text{TiO}_2)$	$E_d^1 + E_d^2$	$E_{int.}$
T	0.11	3.49	3.60	9.18
B	0.29	3.88	4.17	8.95
S	0.17	3.76	3.93	8.03

Similarly to the analysis of the adsorption on defect-free MgO(100) surface, structural transformations between the three configurations are studied by performing the CINEB calculations (Sec.2.2.5). The minimal energy path between **T** and **S** structures is similar to that in the gas-phase¹⁰ and passes through **B** configuration. However, the energy barriers of 0.57 eV for the transformation from **T** to **B** and 0.91 eV from **B** to **S** isomer are much different from the corresponding barriers both in the gas-phase and on MgO(100) surface (Sections 3.4 and 5.3). At TiO₂(110) the differences can be attributed to the different number of bonds that need to be brake simultaneously in order to perform the transformations. It is necessary, for both transformations, to break simultaneously one Ir-Ir bond (as in the gas-phase) and one bond formed upon adsorption between one of the Ir atoms and one basal O atom (check Fig.5.12). The transition states lay, in both cases, in the configurations where both Ir-Ir and Ir-O bonds are broken and the new ones with bridging O atoms are not fully established yet. This is the reason for a much higher activation energies for structural transformation between the three isomers.

¹⁰Of course, when considered only in the Ir₄ configuration space.

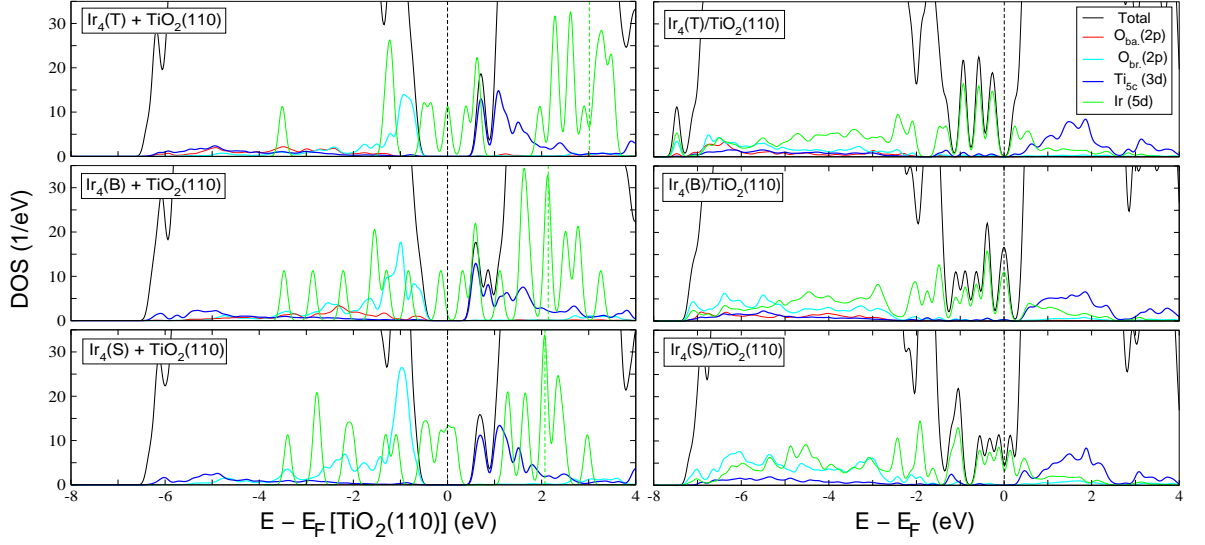


Figure 5.13: Left: DOS of the gas-phase **T** and **S** Ir₄ isomers (green curve) together with the DOS of rutile TiO₂(110) surface (black). DOSs are aligned on the same vacuum level. Both subsystems are "frozen" in their interacting atomic configurations. Projections on the 2p states of interacting surface O atoms (both bridge and basal) and on 3d orbitals of Ti_{5c} atoms neighboring to the adsorbates are shown. Right: DOS of the systems after the adsorption (black curve) together with the projections on the atomic orbitals of the interacting surface and cluster atoms. All DOS are for the nonmagnetic systems.

Even though, the barriers are much higher than in the gas-phase and on the MgO surface the rate constants are still large enough at the temperatures of several hundred degrees Celsius. Under the assumption that the prefactors in Eq.2.19 are $\sim 10^{12}$ the rate constants at 300° C (experimental conditions) lay in the interval from 10^2 Hz for the backward **B**←**S** transition, to $\sim 10^8$ for the transformation **T**←**B**. All half-lives are short enough compared to the time interval (3 h) of the treatment at 300° C that the equilibrium population of the three minima can be considered established. The equilibrium populations of the three local minima (**T**, **B** and **S**) can be easily estimated, under the assumption that the populations are described well by Boltzmann distribution (which is the case in the transition state theory, Sec.2.2.5), to 34.7, 0.3 and 65.0 %, respectively. Therefore, when adsorbed on TiO₂(110), most of the Ir₄ still adopt **S** geometry, but with the significant fraction of those in **T** configuration. Of course, this distribution can be largely affected by the changes in relative energies of the order of 0.01 eV. Since the accuracy of DFT methods (or at least of the model used in this work) is also of this order it only possible to conclude that at TiO₂ a significant fraction of the adsorbed Ir₄ species will adopt **T** geometry.

This result is in much better qualitative accord with experiment than for the adsorption on MgO(100) surface. The differences compared to the experimental results could also arise since Ir₄/TiO₂ clusters are produced using the Degussa P25 TiO₂ powder [126] which consists of 3/4 of anatase and 1/4 of rutile phases. Although rutile (110) surface that is used in calculations is similar to the most stable anatase (101) surface (they both have only Ti(5c) exposed to the vacuum) differences of the order ~ 0.1 eV in relative energies of different adsorption geometries are certainly possible.

Calculated Ir–Ir distances are also ~ 0.2 Å shorter than the measured ones and there are

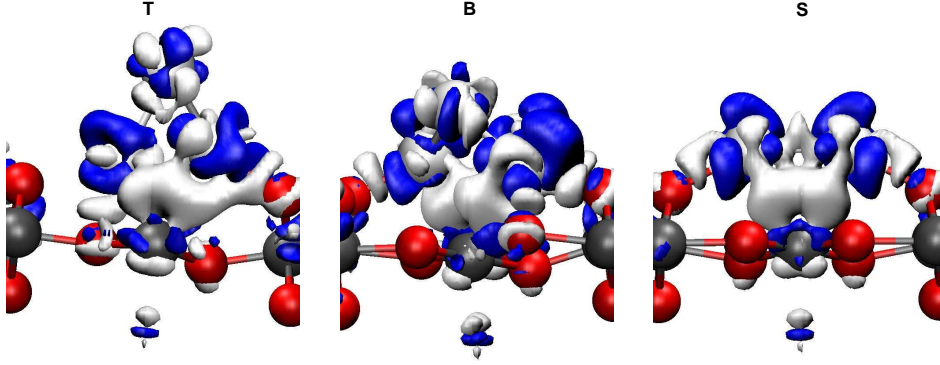


Figure 5.14: Isosurface plot of the density difference $\Delta\rho$ for **T**, **B** and **S** Ir_4 isomers when adsorbed on $\text{TiO}_2(110)$ surface. Bright isosurface indicates a charge gain, while blue one charge depletion. The isosurfaces are at $\pm 0.035 \text{ e}/\text{\AA}^3$. The Ir atoms are mostly covered by the isosurfaces. Only neighboring atoms of the surface topmost layer are shown.

some disagreements on the longer Ir–O coordinations. As already discussed in Sec.5.3 the discrepancies in the Ir–Ir distances may occur due to temperature effects while the longer Ir–O coordination could be different due to the fact that most of the adsorption occurs on different surface, anatase (101) instead of rutile (110).

As in previous sections analysis of adsorption of Ir_4 isomers to $\text{TiO}_2(110)$ surface is done by dividing the process in two contributions, deformations of both adsorbates and the support and energy gain due to the purely electronic interactions. These contributions are presented in Tab.5.7. It is evident that the different binding of **B** isomer compared to **T** is mainly due to bigger deformations 0.57 eV, while a smaller portion 0.23 eV comes from the electronic effects. On the other hand, only 0.33 eV of the difference in binding energy of **S** isomer comes from the bigger surface relaxations and much bigger part 1.15 eV is due to electronic effects. The electronic interaction energies can be further reduced to energies needed to change the magnetic moments of the three isomers and the electronic interactions of the Ir_4 clusters with fixed magnetic moments. The **T** isomer does not change its gas-phase magnetization ($0 \mu_B$) neither due to deformations nor adsorption. Reduction of the magnetic moment of **S** structure due to adsorption is $8 \mu_B$ and the energy needed for this change is large and amounts to 0.51 eV. Therefore, almost one half of the difference in $E_{\text{int.}}$ between **S** and **T** structures is due to the reduction of the **S** magnetization. On the other hand, the moment of **B** isomer changes upon the relaxation from the gas-phase 2 to $4 \mu_B$ for the deformed isomer and it changes back to $2 \mu_B$ upon adsorption. The energy needed for this $\Delta m = 2 \mu_B$ change is only 0.05 eV.

In Fig.5.13 details of the electronic structure of the three Ir_4 isomers and the support prior and after the adsorption are presented. The Fermi levels of the free clusters are positioned deep in the conduction band of the support. The three clusters with zero magnetization and the support are in their relaxed atomic configurations. Since the total energy of adsorbed **B** structure with zero magnetization lays only 0.05 eV above the $2 \mu_B$ ground state, the analysis is done on the non-magnetic system. Main features of the electronic interactions of the three isomers are similar. Spectral weight of the atomic orbitals located on the interacting O atoms is distributed mainly in the valence with very small, almost negligible, amount in the conduction band. As in the case of the adsorption on defect-free $\text{MgO}(100)$ the deformations

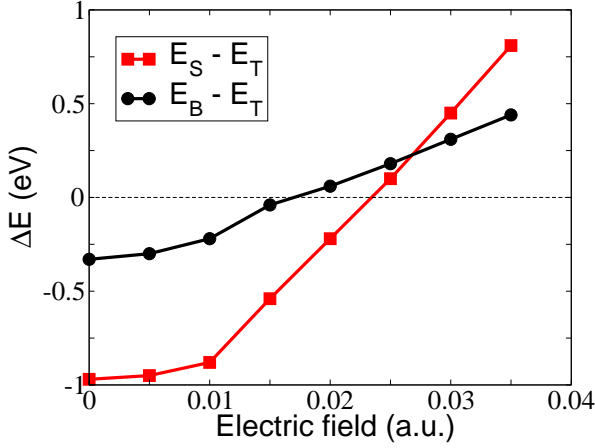


Figure 5.15: Dependence of the relative energies of **B** and **S**, calculated with respect to **T** isomer, on external electric field (in Rydberg a.u.). Clusters are in the same atomic configuration having the same magnetization as when adsorbed on $\text{TiO}_2(110)$ surface.

localizes these states close to the top of the valence band and the interaction pushes them to the lower energies. This effect is less pronounced on $\text{TiO}_2(110)$ surface due to the much bigger energy difference between the valence band maximum and the electronic states of the three isomers around the Fermi energy. In accord with experimental findings [10] there is no significant transfer of the spectral weight across the Fermi energy after the adsorption.

On the other hand, states from $\text{Ti}(5c)$ atoms, localized by the deformations at the bottom of the conduction band, are shifted after the adsorption to higher energies. Again, there is no transfer of their spectral weight to lower energies in the occupied parts of the three spectra. The distances between interacting Ir and basal Ti atoms are 2.55–2.65 Å. These values are too big for any appreciable overlap of their d -orbitals. Therefore, the interaction of Ir_4 with surface Ti atoms is mostly electrostatic. Electrons from the adsorbates, attracted by the positively charged surface Ti ions, approach closer to the surface destabilizing $3d$ orbitals of near titanium atoms. These polarization effects can be observed from the charge difference $\Delta\rho(x, y, z)$ shown in Fig.5.14. Density is mostly depleted from the basal Ir atoms and accumulated between them and the interacting O atoms (formation of covalent bonds) as well as in the interfacial region between the two clusters and the surface Ti ions. Consequently, Ti cations, also attracted by the electronic density accumulation, relax out of the surface while the O anions laying below the clusters are pushed by the electrostatic interaction deep into the surface. Since there is no significant charge transfer between two subsystems (cluster and the support) the induced dipole moments are mainly due to the polarization effects. They are oriented from the surface to the adsorbates in all three cases. Differences in the values of dipole moments result mainly from a different charge displacement along the vertical axis. These strong electrostatic interactions on the TiO_2 surface are a consequence of the anomaly in the effective (Born) charges present in the rutile TiO_2 . It is already known that the effective charges of the bulk rutile TiO_2 , depending on the nuclear displacement direction, are 5.20–7.70 electrons for Ti cations (check reference [129] p.57 and also the references therein).

Polarization of the three isomers is not only responsible for the surface relaxations and induction of the dipole moments, but is crucial for altering relative stability between the three isomers. This can be proved by placing the free clusters with the same magnetization and the configurations as when adsorbed on TiO_2 , in the external electrostatic field. In periodic-supercell calculations this can be done by adding a saw-like potential to the Kohn–Sham Hamiltonian, whose slope in the region of the cluster is determined by the value of the electric field (for the details check the manual of **QUANTUM-ESPRESSO** code [35]). Calculations

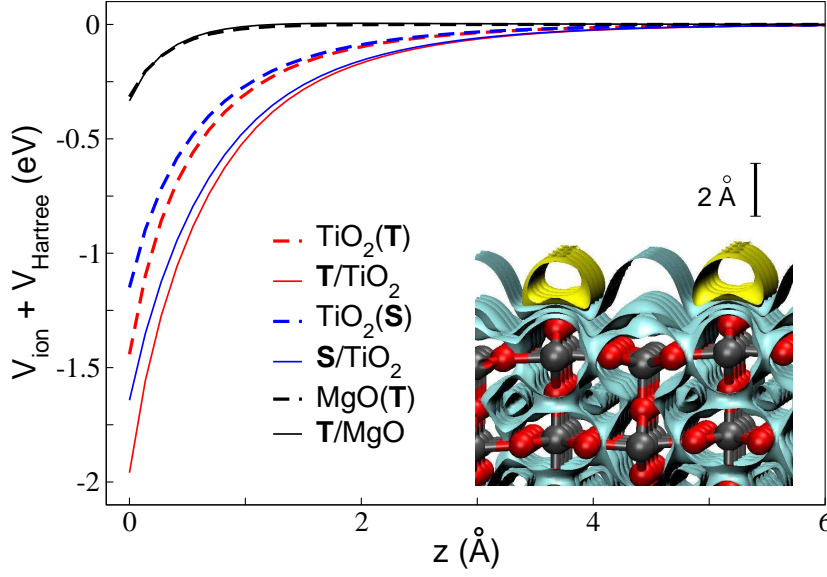


Figure 5.16: Electrostatic potentials of the TiO_2 surface averaged in the plane parallel to the surface (xOy plane) only in the region defined by the adsorption geometry of **T** and **S** isomers (see text for details). Potentials of both unrelaxed and the relaxed surfaces are shown. The $z = 0.0$ Å value is placed halfway between the support and the adsorbed clusters. The potential of $\text{MgO}(100)$ surface for the adsorption of **T** isomer is presented for comparison. The inset shows isosurfaces with the values -3.0, -1.2, -0.2 (cyan) and +0.2 eV (yellow) of the electrostatic potential of the clean $\text{TiO}_2(110)$ surface.

are performed for several electric fields and the dependence of the relative energies of **B** and **S** calculated with respect to **T** isomer is presented in Fig.5.15. The relative energies depend strongly on the applied field. They increase monotonically as magnitude of the field grows. For the value of the field of 0.015 a.u. (1 Rydberg a.u. = 51.44×10^{10} V/m) relative energy of **B** with respect to **T** configuration becomes -0.04 and that of **S** structure is -0.54 eV. When the support deformation energies are added to these values the relative energies of the three isomers are 0.23 and -0.15 eV for **B** and **S**, respectively. These values are very close to the relative energies from Tab.5.6. Further increase of the applied field leads to further increase of relative energies of both **B** and **S** structures. It is even possible, for a sufficiently high fields (above 0.03 a.u.), to reverse completely the gas-phase energy order of the three isomers.

Moreover, if the electrostatic potential of the support is averaged in the plane parallel to the surface, but only in the region of space occupied by the clusters¹¹ then the surface electric field in the normal direction can be estimated as the derivative of the averaged potential (see Fig.5.16). If an average slope of the potential is calculated from the $z = 0$ in Fig.5.16 to the point where the potential is 5 % of its $V(z = 0)$ value (~ 2.4 Å) the obtained electrostatic field is 0.013–0.015 a.u. (depends on the adsorbed isomer). Just for comparison, the calculated field in the vicinity of $\text{MgO}(100)$ surface is 0.006 a.u. and the potential drops to 5 % of its lowest value very fast at 0.97 Å which is approximately around the positions of the basal Ir atoms.

If the gas-phase Ir_4 clusters are allowed to relax both their atomic coordinates and magnetic moments the situation would not be the same. They would orient differently with

¹¹This region is defined as the region of space whose points are closer to the Ir atoms of the three clusters than to any other atom in the system.

respect to the applied field and **S** isomer would remain the most stable structure. Therefore, the effect of the surface on the isomer stability is twofold. Chemical bonds ensure the appropriate geometry of the three clusters and then the surface field makes the change in their relative energies. It is not unknown that external electric field may influence structures of $\text{Si}_n\text{C}_{5-n}$ clusters introducing additional relaxations [130] or assist in dissolution of metal clusters in metal island films [131]. However, this is the first report on the surface affecting relative energies of different configurations of adsorbed clusters through its electrostatic field.

Chapter 6

Influence of Adsorbates on the Relative Stability of Oxide Supported Ir₄ Clusters

Interactions of Ir₄ clusters with different types of atomic (H, C and O) and molecular species (CO) have already been studied in the gas-phase (Chap.4). Presence of the substrate may affect the electronic structure of the supported species and in that way influence their interactions with the environment. Equivalently, interactions with the environment may also induce changes in the electronic structure of the supported clusters and influence their interaction with the support.

Interactions of both MgO(100) and TiO₂(110) supported Ir₄ clusters with atomic (H, C and O) as well as molecular species (CO molecules) are the subject of this chapter. The result obtained for the gas-phase Ir₄ that one carbon adatom alters the relative stability of different isomers (Sec.4.1) motivated research in this direction. Moreover, the discrepancies with experimental results about the structure of the MgO supported Ir₄ (Sec.5.3) remain unexplained. On the other hand, for TiO₂(110) substrate it has been shown that strong electrostatic field present in the vicinity of the surface can, to a large extent, explain properties of the adsorbed pristine Ir₄ clusters (Sec.5.6). It is interesting to study how does this field, which influences considerably both relative stability and the electronic structure of Ir₄, affect their interactions with the environment.

6.1 Interaction of MgO(100) Supported Ir₄ Clusters With H, C or O atoms

Many different adsorption geometries of atomic H, C and O on the three Ir₄ isomers supported by MgO(100) have been inspected and the most stable configurations are displayed in Fig.6.1. Their properties are presented in Tab.6.1. Again, available experimental results [118, 119] for the MgO supported Ir₄ clusters are presented next to the calculated ones for comparison.

Effects of the interaction of the MgO supported Ir₄ with atomic H, C and O (Sec.4.1) are similar to those in the gas-phase. Upon interactions the relative stability of the three supported Ir₄X (X = H, C and O) structures remains close to that predicted for the gas-phase Ir₄X (Tab.4.1). Again, only the C adsorption affects considerably the relative stability, but

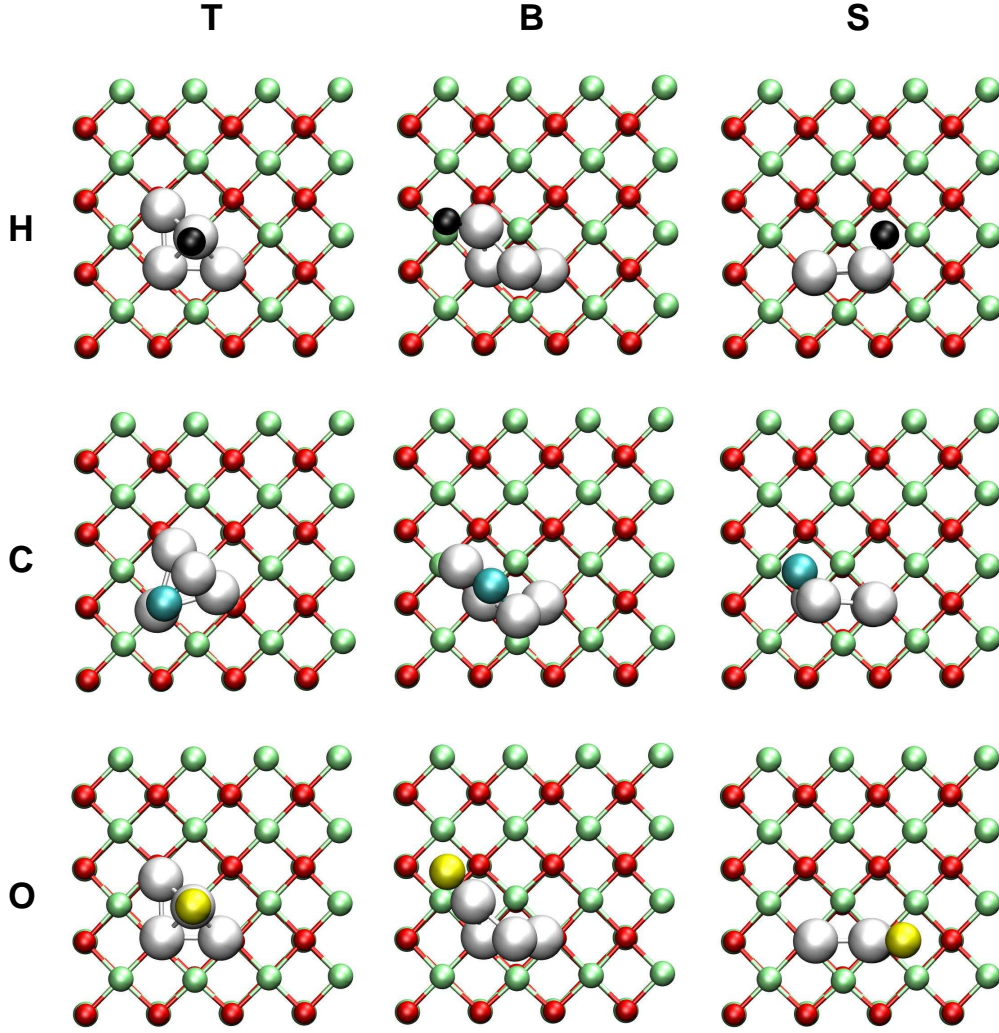


Figure 6.1: The most stable configurations of $\text{Ir}_4/\text{MgO}(100)$ clusters when interacting with atomic H, C and O. The same color scheme is used as in Fig.4.1 and Fig.5.5 except for the interaction with oxygen (the lower panel) where the O adatom is colored in yellow.

now with one important difference. While in the gas-phase **B** isomer with a single C adatom becomes the most stable structure, on $\text{MgO}(100)$ surface **T** structure, in accordance with experimental results [118, 119], is the configuration with the lowest total energy (reported in Ref.[69, 70]). Carbon binding energies remain very close to the gas-phase values pointing out that the surface has no effect on the interaction of Ir_4 with the carbon adatom. However, since the differences in carbon binding energies between the three isomers stay close to the gas-phase values, crucial effect in this change of stability in favor of **T** structure is the reduction in relative energies of the pristine clusters due to the adsorption on $\text{MgO}(100)$ surface. Namely, upon adsorption energy of pristine **B** relative to **T** isomer is reduced from the gas-phase -0.58 to only -0.14 eV. The same happens with the relative energy of **S** structure which goes from -1.51 to -1.06 eV. With these reductions differences in the carbon binding energies are large

Table 6.1: Calculated properties of **T**, **B** and **S** Ir₄X (X = H, C and O) clusters when adsorbed on MgO(100). E_b refers to the binding energy of the adsorbates $E_b = -E(\text{Ir}_4\text{X}/\text{MgO}) + E(\text{Ir}_4/\text{MgO}) + E(\text{X})$ and the total Ir₄X cluster binding energy given in parentheses. All other quantities are the same as in Tab.5.2.

		ΔE [eV]	E_b [eV]	M [μ_B]	p_z [D]	Ir-Ir		Ir-O		Ir-Mg		Ir-C	
						N	R[Å]	N	R[Å]	N	R[Å]	N	R[Å]
Ir ₄ H	T	0.00	3.21(3.94)	0.58	-5.62	2.5	2.42	0.75	2.14	0.75	2.74		
						0.5	3.46	1.5	3.56	0.75	2.97		
	B	-0.03	3.09(3.15)	1.06	-4.24	2.5	2.41	0.5	2.05	1.2	2.88		
						0.5	3.66			0.5	3.28		
	S	-0.90	3.06(3.29)	1.22	-4.05	2.0	2.32	0.5	2.06	1.0	2.88		
						1.0	3.28			1.0	3.17		
Ir ₄ C	T	0.00	8.16(3.57)	1.95	-3.86	2.5	2.52	0.75	2.21	0.5	2.59	0.5	1.79
						0.5	3.04			1.0	3.18	0.5	2.83
	B	0.15	7.86(3.08)	0.00	-4.00	2.0	2.44	0.5	2.07			0.5	1.78
						0.5	3.16						
	S	0.65	6.46(3.22)	2.54	-3.87	2.0	2.41	0.5	2.05			0.5	1.85
						1.0	3.40						
Ir ₄ O	T	0.00	6.00(3.36)	2.01	-7.54	2.5	2.44	0.75	2.14				
						0.5	3.46						
	B	-0.48	6.33(3.22)	0.44	-5.14	2.5	2.41	0.5	2.06	1.5	2.93		
										0.5	3.33		
	S	-0.97	5.91(3.08)	0.00	-6.29	2.0	2.32	0.5	2.09	1.0	2.90		
						1.0	3.28			1.0	3.21		
Exp.	Ref.[118]					2.6-3.1	2.62-2.73	0.6-1.1	2.07-2.16				
								2.5-3.0	2.59-2.73				
	Ref.[119]					2.9	2.62	1.1	2.05	0.6	2.45	0.5	1.91
								0.5	3.33				

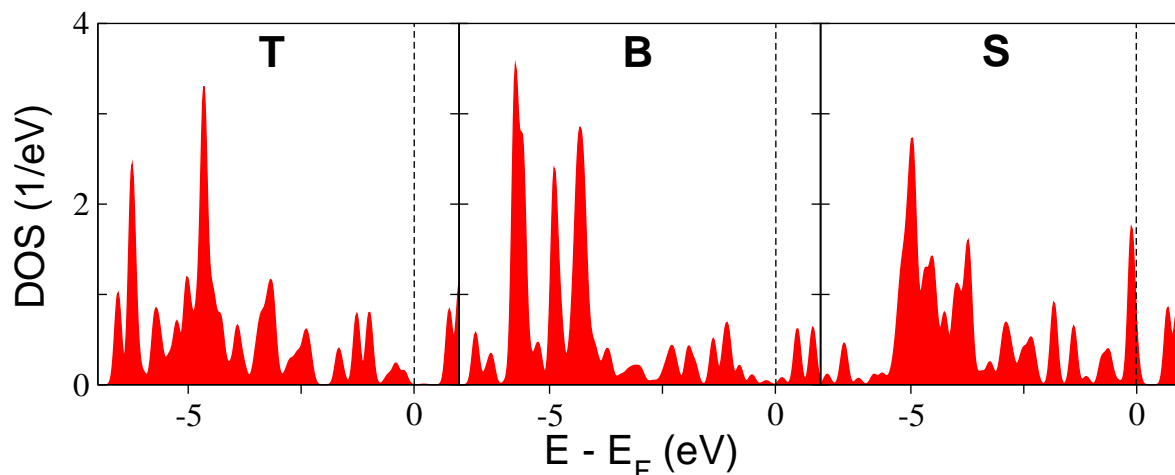


Figure 6.2: Spin majority projected DOS on the atomic $2p$ orbitals of the carbon adatom, adsorbed on the three MgO(100) supported Ir_4 isomers.

enough to make **T** the most stable $\text{Ir}_4\text{C}/\text{MgO}(100)$ structure and to push **S** isomer further apart from **T** than in the gas-phase.

The carbon adsorption geometries (Fig.6.1) are the same as those in the gas-phase (Fig.4.1). Carbon binds the most favorably to the bridge site between two Ir atoms and induces breaking of the corresponding Ir–Ir bond of both **T** and **B** isomers. Similarly to the gas-phase the interaction of the C adatom with **S** is weaker and the Ir–Ir bond bridged by carbon is not completely broken. Of course, not all Ir–Ir bridging sites are equivalent on the supported clusters and it is energetically the most favorable for C adatom to bind in such a way to minimize the interference between the two interactions, cluster–support and cluster–carbon.

The explanation for the stronger carbon binding on **T** and **B** isomers than on **S** remains the same as for the gas-phase species (Sec.4.1). In Fig.6.2 the projected DOS on $2p$ atomic orbitals of the C adatom is shown for all three isomers. The DOSs are very similar to those in the gas-phase (Fig.4.2); of course, with the differences produced by the interaction with the surface (mostly broadening of the peaks). For both **T** and **B** isomers more of the carbon spectral weight is shifted to lower energies than in the case of **S** structure. Electronic orbitals formed upon interaction with the carbon resemble those shown in Fig.4.2. The antibonding molecular orbital (MO) of both **T** and **B** isomers, responsible for the particularly strong interaction with C– $2p$ atomic orbitals (AO) in the gas-phase, remains above the Fermi energy for the pristine clusters on MgO(100) despite modifications in their electronic structure induced by the support. The interaction with the C– $2p$ orbitals pushes these electronic states to the bottom of the carbon spectra as for the gas-phase species. The other interaction channels for all three isomers also stay similar to those in the gas-phase.

The carbon adatom induces some modifications in the cluster–support interaction. The total cluster binding energies of **T** and **B** structures are by 0.26 and 0.27 eV lower than for the pristine clusters adsorbed on the MgO surface. Energy gain due to the adsorption of Ir_4C in **S** configuration (3.22 eV) remains much closer to the value for the pristine cluster (3.33 eV). This effect of somewhat weaker binding to the support for **T** and **B** structures with and without carbon is accompanied by the change in the induced dipole moment. In the case of **T**, structural distortions induced by the C adsorption weaken the Ir–O interaction

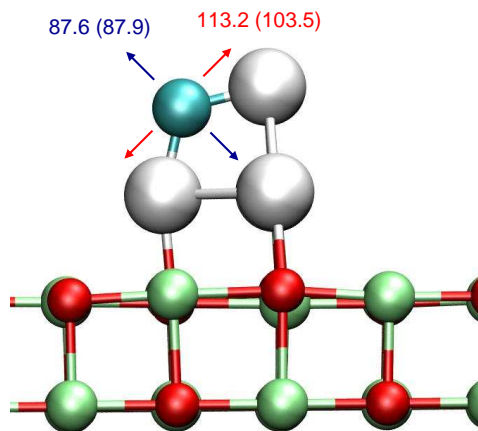


Figure 6.3: Motion of the carbon adatom on the supported **T** isomer along the two highest frequency, purely carbon vibrational modes. Numbers denote frequencies (in meV) of these modes for **T** isomer supported by MgO (in the gas-phase).

(see the average Ir–O distance). Hence, the overall interaction with the surface is somewhat weaker as well as the charge transfer and the dipole moment decreases. The dipole moment of **B** structure increases since the carbon adatom induces charge rearrangements (also not very strong) which consequently lead to the drop of the electrostatic interaction between the cluster and the support.

Interaction with the carbon adatom also induces modifications in the geometries of the three isomers. The first shell Ir–Ir coordination number remains the same upon carbon adsorption for both **T** and **S** structures while its value decreases to 2.0 for **B** due to the breaking of the Ir–Ir bond bridged by the carbon. The distance between these two Ir atoms increases to 3.16 Å, value very close to the gas-phase (3.19 Å), while the distance between the two wing-tip Ir atoms becomes 4.11 Å (not presented in Tab.6.1). Although the C adsorption also induces breaking of one Ir–Ir bond of **T** structure the coordination number remains the same since the two basal Ir atoms of the pristine cluster which are by 3.68 Å apart, approach closer to each other upon C adsorption (2.49 Å) reestablishing the broken Ir–Ir bond.

As for the MgO supported pristine Ir₄ the best agreement between calculated and measured structural data is for **T** structure which is now the most stable and hence, the most probable Ir₄C/MgO(100) configuration. The average first shell Ir–Ir distance of the supported **T** isomer with the C adatom is only by 0.1 Å (~4 %) lower than those reported from experiments (see Tab.6.1). Moreover, **T** structure is less distorted than without the carbon. Still, there are some differences in the first shell Ir–O coordination and distances, but the data for Ir–Mg as well as Ir–C shells agree reasonably well. The results for **B** and **S** structures do not correspond well to experiment.

Finally, the vibrational analysis is carried out for the **T** isomer with the carbon adatom both in the gas-phase and supported by MgO(100). Calculations are done in the frozen phonon approximation (see Sec.2.2.4) allowing only C, Ir and the surface atoms that are close to the cluster to move. Due to the large mass difference of the carbon and iridium atoms, purely carbon vibrational modes appear in both spectra¹. The two highest frequency modes,

¹Amplitudes of the C and Ir atoms along these modes differ by an order of magnitude.

appear to be of the carbon character both on MgO(100) and in the gas-phase. They are well separated from all the other modes in both spectra. For the MgO supported (gas-phase) **T** structure, the frequencies of these two carbon modes are 113.2 (103.5) and 87.6 (87.9) meV. Motion of the C adatom along these modes is the same for both environments. The highest frequency mode is longitudinal with respect to the line connecting the two bridged Ir atoms, while along the second mode the motion of C is transversal as depicted on Fig.6.3. All the other vibrations of the system involve large displacements of the Ir atoms and the frequencies approach the values for the pristine gas-phase cluster (10–40 meV). Since the highest frequency mode lays well above the vibrational frequencies of the clean MgO(100) surface (~ 88 meV ~ 709 cm $^{-1}$ [122]) it could serve for the experimental verification of the carbon presence².

At variance to the C adsorption both H and O adatoms do not influence considerably the energy ordering of the three Ir₄ isomers. In both cases **S** isomer remains the most stable form also when supported by MgO(100) surface. While the energy of **S** relative to **T** structure remains close to the values for the supported pristine clusters the relative energy of **B** isomer approaches close to zero for the H adsorption and to -0.5 eV after the interaction with the O adatom. Binding configurations are the same as in the gas-phase and they also do not correspond well to the experimental results (in addition to the different relative stability of Ir₄ isomers). The binding energies of the H adatom and Ir₄H cluster lay very close to the corresponding values in the gas-phase and for the adsorption of pristine clusters on the MgO, respectively. On the other hand, the oxygen binding energies are lower than in the gas-phase and the adsorption is accompanied by the charge rearrangements (both different transfer from the surface and different distribution of that charge) that are followed by the considerable increase in the induced dipole moments. These charge redistributions influence also the total cluster binding energies, especially in the case of **T** structure.

6.2 Interaction of MgO(100) Supported Ir₄ Clusters With CO Molecules

The lowest total energy configurations for the adsorption of one and two CO molecules on the three MgO(100) supported Ir₄ isomers are presented in Fig.6.4. The structural data and energetics are presented in Tab.6.2 and Tab.6.3. For the supported **T** isomer the study of the interaction with CO molecules was continued to the adsorption of up to five CO molecules. The work is motivated by the experimental procedure for producing supported Ir₄ clusters which involves decarbonylation of the supported Ir₄(CO)₁₂ molecules (Ref.[119] and references therein).

Similarly to the gas-phase, interaction with one CO molecule alters considerably the relative stability of the three isomers, but on the MgO the most stable isomer becomes **T**. However, it is only by 0.01 eV lower in energy than **S** and given the accuracy of the theoretical model (check Tab.5.1) these two structures can be treated as degenerate. On the other hand, **B** isomer interacting with one CO molecule becomes the least stable structure whose energy lays by 0.34 eV higher than that of **T**.

The CO binding configurations are different than in the gas-phase. On **T** structure the dissociative CO adsorption is still more favorable than adsorption in molecular form (by 0.51

²Everything said here is under the assumption that the adsorption of Ir₄ clusters whose vibrational frequencies are 10–30 meV, would not produce vibrations whose frequencies are higher than ~ 88 meV.

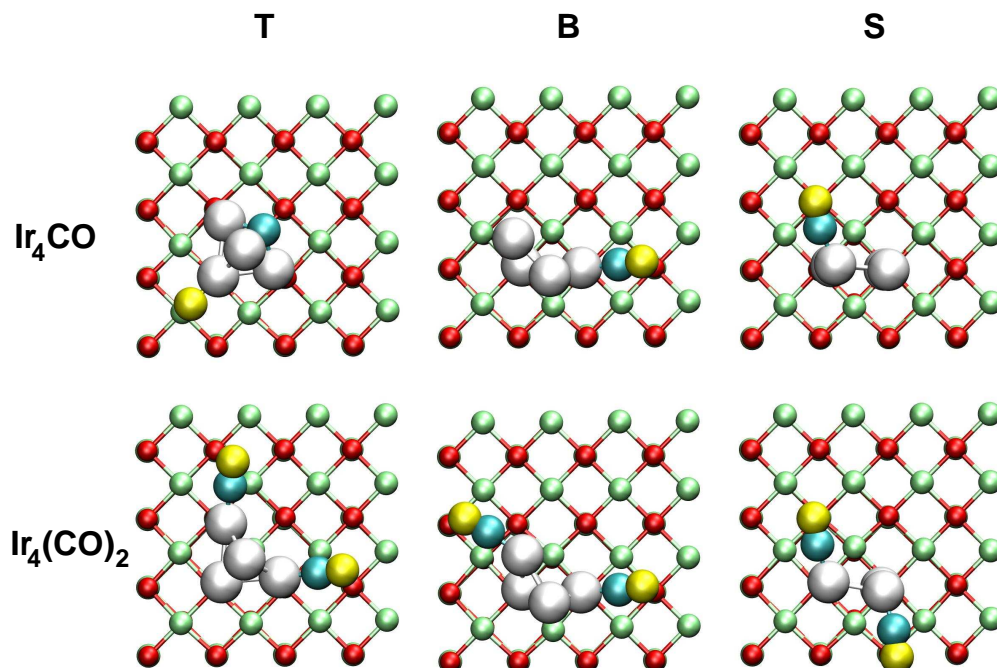


Figure 6.4: Configurations with the lowest total energies for the three MgO(100) supported Ir₄ isomers (**T**, **B** and **S**) interacting with one (upper panel) and two CO molecules (lower panel). The same color scheme as in Fig.6.3 is used.

eV) while to both **B** and **S** one CO binds preferentially as a molecule, by 0.76 and 0.87 eV stronger than if dissociated, respectively. The carbon atom binds upon dissociative CO adsorption to the three Ir atoms of **T** structure while the oxygen is at bridging site between the fourth iridium and the closest surface Mg atom (Fig.6.4). Binding of the C adatom at the three-fold site is also very favorable C adsorption geometry (without the oxygen) both in the gas-phase and on the MgO. It is by 0.19 and 0.13 eV higher in energy than the adsorption at the bridging site, respectively. The explanation for the strong carbon bonding to **T** isomer at the three-fold site is similar to that for the bridging configuration³. Adding one oxygen atom to the MgO supported cluster the configuration from Fig.6.4 becomes more stable, by 0.35 eV lower in energy than that with the carbon at the bridging site and oxygen interacting with one of the two other basal Ir atoms. Interaction of the oxygen atom with the surface cation is crucial for the increased stability of the geometry for dissociative CO adsorption on **T** structure from Fig.6.4.

Molecular CO binds to both **B** and **S** as a terminal with the carbon atom in contact with the cluster, similarly to the gas-phase. However, the sites and orientation of the CO ligand are different. It binds on **B** structure to a wing-tip Ir atom instead to a middle one, and on **S** isomer to one of the top Ir atoms, almost orthogonal to the plane defined by the cluster. This indicates that the binding of the three clusters to the substrate and interaction with the CO molecule are not two independent processes. The values of the CO binding energies confirm

³Strong interaction with the empty antibonding MOs of the cluster which are transformed by the interaction with the C adatom into the strongly bonding orbitals.

Table 6.2: Calculated properties of Ir₄CO in **T**, **B** and **S** configurations when adsorbed on MgO(100) surface (Fig.6.4 upper panel). E_b refers to the binding energy of the CO molecule $E_b = -E(\text{Ir}_4\text{CO}/\text{MgO}) + E(\text{Ir}_4/\text{MgO}) + E(\text{CO})$ and the total Ir₄CO cluster binding energy given in parentheses (calculated using the gas-phase cluster with the CO molecule in the same form). All other quantities are the same as in Tab.5.2.

		ΔE [eV]	E_b [eV]	M [μ_B]	p_z [D]	Ir-Ir		Ir-O		Ir-Mg		Ir-C	
						N	R[Å]	N	R[Å]	N	R[Å]	N	R[Å]
Ir ₄ CO	T	0.00	3.49(3.33)	0.00	-3.14	2.5	2.53	0.5	2.11	0.5	2.69	0.75	1.90
						0.5	3.03	1.0	3.48				
	B	0.35	3.00(3.17)	1.99	-3.89	2.5	2.44	0.5	2.07	2.0	3.03		
								0.5	3.49				
	S	0.01	2.42(3.11)	1.72	-4.79	2.0	2.35	0.5	2.05				
						1.0	3.32						
Exp.	Ref.[118]					2.6-3.1	2.62-2.73	0.6-1.1	2.07-2.16				
								2.5-3.0	2.59-2.73				
	Ref.[119]					2.9	2.62	1.1	2.05	0.6	2.45	0.5	1.91
								0.5	3.33				

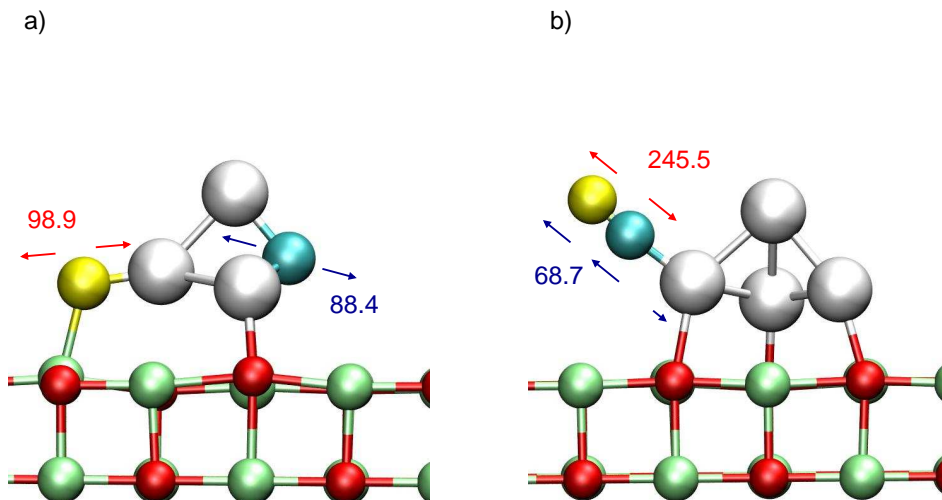


Figure 6.5: Motion of the C and O atoms on the MgO supported **T** isomer along the highest frequency vibrational mode upon (a) the dissociative CO adsorption and (b) the molecular CO adsorption. Numbers denote frequencies (in meV) of the corresponding modes.

this fact. They are all lower than in the gas-phase. This is also true for the total cluster binding energies.

The biggest structural modifications as well as modifications of the binding energies are induced for the CO adsorption on **T** isomer. The Ir atom that interacts with the oxygen coming from the CO molecule, relaxes out of the surface to the distance of 2.67 Å from the surface oxygen⁴ (check Fig.6.5). This reduces both total cluster binding energy to the surface as well as the charge transfer. The adsorption of O adatom is not any more independent of the C adsorption (as in the gas phase) since all Ir atoms interact either with the carbon adatom or with the surface O atoms. At variance to **T**, the CO and the total cluster binding energies of **B** and **S** structures remain much closer to the values for the CO adsorption in the gas-phase and adsorption of the pristine clusters on the MgO. Therefore, the crucial effect that enables the CO molecule to alter the relative stability of the three isomers is again (as for the C adsorption) the reduction of the pristine cluster relative energies due to the interaction with the support.

Calculated structural data for Ir₄CO/MgO(100) in **T** configuration with the dissociated CO molecule (Tab.6.2) agree with the experimental data as well as for **T** structure with only the C adatom (Tab.6.1). Calculated Ir-Ir coordinations and distances are almost the same while there are some differences in the other shells. However, those differences are not sufficient to determine which structure suits more to the measured one.

Since the carbon binding geometry differs from that without the coadsorbed oxygen, the carbon vibrational modes could have different frequencies. Moreover, the modes of the purely O character could also be expected. Both effects are confirmed by the vibrational analysis. The highest frequency mode of 98.9 meV = 797 cm⁻¹ is now the oxygen mode, while the following three modes are purely of the carbon character with frequencies 88.4 meV (713 cm⁻¹), 86.2 meV (695 cm⁻¹) and 66.6 meV (537 cm⁻¹). Lower values reflect weaker binding at the three-fold than the bridging site. Calculated carbon frequencies lay close and below

⁴This coordination shell is not presented in Tab.6.2 since its average coordination number is only 0.25.

the upper limit $88 \text{ meV} = 709 \text{ cm}^{-1}$ [122] of the $\text{MgO}(100)$ vibrational spectrum and it is certainly more difficult to distinguish them experimentally. However, the oxygen mode should be possible to detect since it lays about 90 cm^{-1} higher than those of the MgO surface. Motion of the C and O atoms along the two highest frequency modes is presented schematically in Fig.6.5.

Vibrations of the CO molecule when adsorbed on the MgO supported **T** cluster are also studied. The most favorable geometry for the molecular CO binding is shown in Fig.6.5 together with the motions of the C and O atoms along the two highest frequency modes. This configuration is by 0.51 eV higher in energy than that for the dissociative adsorption. The CO binding energy in this configuration is 2.98 eV . The CO stretching mode of $245.5 \text{ meV} = 1980 \text{ cm}^{-1}$ is the highest in frequency. The frequency of the second highest mode, that involves motion of the C and O atoms, lays well below at $68.7 \text{ meV} = 554 \text{ cm}^{-1}$. The C and O atoms move in-phase along this mode in the direction of desorbing from the cluster (see 6.5). The CO stretching mode is used in experiments for the verification of the presence of the carbonyl ligands during the preparation process [123]. Calculated CO stretching frequency agrees very well with the range of measured values $1884\text{--}2052 \text{ cm}^{-1}$ attributed to the same mode for the MgO supported $\text{Ir}_4(\text{CO})_{12}$ molecules [123].

6.2.1 CO Dissociation

Until this point the issue of the CO dissociation, which would change the relative stability of the three Ir_4 isomers in favor of **T** structure, has only been addressed in the gas-phase (Sec.4.3). It has been found that the barrier for the CO dissociation, although quite high, is the lowest on **T** isomer (2.67 eV). This is due to the peculiar situation where the transition state for the CO dissociation is the same for all three isomers. The reaction requires the smallest amount of energy on **T** isomer since the configuration with the molecular CO, is the highest in energy (closest to the transition state). However, main consequence is that on **T** structure the CO dissociation requires less energy (2.67 eV) than the CO desorption (3.16 eV).

The CO dissociation on the MgO supported Ir_4 is studied only on the supported **T** structure since only in this case the reaction would be spontaneous (exothermic). Since the dissociative CO adsorption on the other two structures (**B** and **S**) is much less favorable, one cannot expect that the large fractions of CO molecules on these two isomers would be dissociated in real situation. Moreover, in experiments the decarbonylation is performed on the iridium carbonyl cluster which has a tetrahedral metal frame.

Predicted minimal energy path (MEP) for the CO dissociation occurring on the MgO supported **T** structure is presented schematically in Fig.6.6. Calculated energy barrier for the process is 2.97 eV which is only by 0.01 eV lower than the molecular CO binding energy (see previous section). Hence, on the MgO supported structure it is as favorable to dissociate one CO molecule as to desorb it⁵. Still activation energy is quite high and would require (in the thermal equilibrium) very high temperatures to occur.

The crucial step for the dissociation is again, as in the gas-phase, the configuration in which the carbon atom resides at a bridging site. As shown in Fig.6.6 the geometry of the transition state is such that both C and O atoms are bridging the Ir–Ir bonds. As already

⁵Calculations of the MEP for the CO desorption yield no barrier for the reaction. The energies of the intermediate configurations increase monotonically to the energy of the configuration with the CO molecule far away from the cluster.

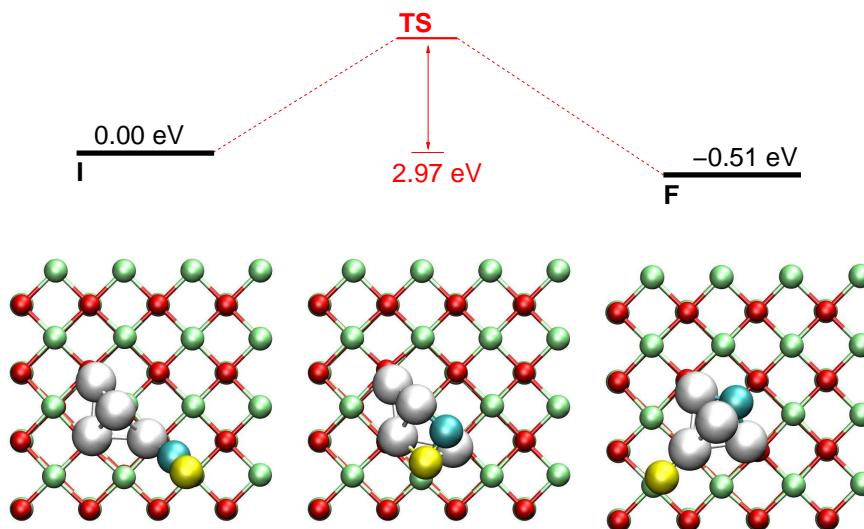


Figure 6.6: The atomic structures of the initial (**I**), transition (**TS**) and final (**F**) states for the CO dissociation on MgO(100) supported **T** structure. The corresponding energies relative to the **I** configuration are also indicated. Schematic plot of the energy levels and the CO dissociation pathway is also displayed.

explained for the gas-phase clusters this enables the $2p$ orbitals of the carbon atom to bind strongly to the cluster and weakens the CO bond. This effect is very strong since it lowers the energy needed for the CO dissociation from 10.97 eV for the free molecule (its atomization energy) to "only" 2.97 eV. However, this does not mean that Ir_4 clusters are good catalysts for this reaction (as for example Ru, Co or Fe [93])

A notion of the rate constants for the two reactions could be obtained by employing Eq.2.19. The vibrational frequencies of the molecular CO adsorbed on the MgO supported **T** structure (previous sections) could serve as the approximate prefactors. Since the CO stretching mode leads to the breaking of the CO molecule, the prefactor for the dissociation would then be of the order of 10^{14} Hz, while for the desorption (the other mode from Fig.6.5) it is 10^{13} , by an order of magnitude lower. Similar energy barriers for both dissociation and desorption imply that the fraction of dissociated CO molecules would be an order of magnitude larger than the fraction of those which desorb. However, since the activation energies for the two processes are very high the timescale for the two reaction are very long compared to the experimental 3h, and by far the biggest fraction of the CO molecules, in the conditions of the thermal equilibrium with the atmosphere surrounding the system, would remain chemisorbed in the molecular form at typical experimental conditions (300° C). The issues of the influence of the environment on the number of chemisorbed CO molecules is discussed in the next section.

6.2.2 Multiple CO adsorption

In the case of adsorption of two CO molecules on $\text{Ir}_4/\text{MgO}(100)$ clusters, **T** isomer becomes the most stable structure (Tab.6.3). It is by 0.66 and 0.49 eV lower in energy than **B** and **S**, respectively. Moreover, the CO dissociation is no longer favorable on any of the three isomers (check the most stable adsorption configurations in Fig.6.4). The formation of CO_2 on **T**

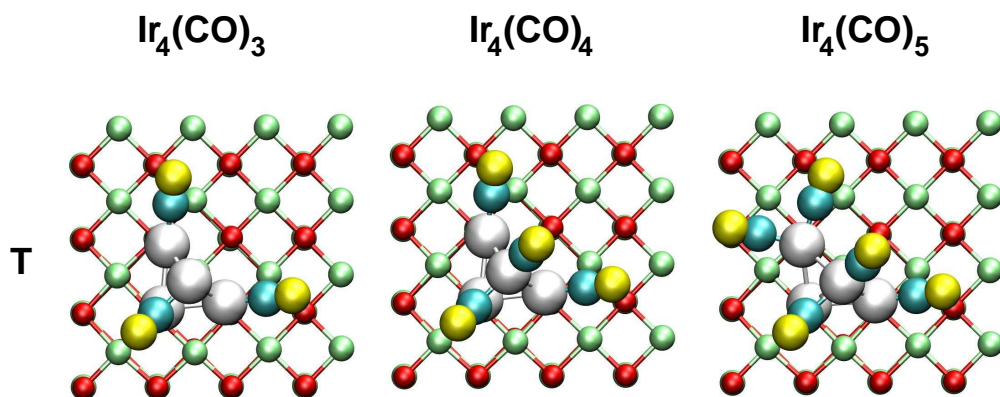


Figure 6.7: Configurations with the lowest total energies for the adsorption of three, four and five CO molecules on MgO(100) supported Ir₄ cluster in **T** geometry.

structure is also not a favorable process. Total energy of the system with two adsorbed CO molecules is by ~ 3.5 eV lower than the configuration with the bridging C adatom and the CO₂ molecule in the vacuum.

Total cluster binding energies are not altered much by the interaction with the two CO molecules (less than 10 % in all three cases). They are calculated using the gas-phase Ir₄ cluster with the same number of molecular CO attached to it, which is not necessarily the most favorable gas-phase Ir₄(CO)₂ geometry⁶. This done in order to show that whatever is the number of CO molecules attached to the cluster (Tab.6.3) it is always energetically more favorable to desorb one CO molecule than the whole cluster (compare the values for the binding energy of *n*th CO molecule and the total cluster binding energies).

If the number of the adsorbed CO molecules increases the binding energy of the *n*th CO molecule, calculated as $E_b = -E(\text{Ir}_4(\text{CO})_n) + E(\text{Ir}_4(\text{CO})_{n-1}) + E(\text{CO})$, decreases as it would normally be expected. However, the binding energy of the fifth CO molecule drops significantly compared to the value for the fourth (~ 1.0 eV). This is accompanied by a similar drop of the total cluster binding energy. The decrease in the total cluster binding energy is a consequence of the modifications of the cluster geometry induced by the fifth CO molecule. Namely, the fifth CO binds as a terminal to one of the basal Ir atoms already having one CO molecule attached to it which produces a drop in the CO binding energy. Moreover, it is energetically more favorable for the cluster to interact with the CO than with surface and even repulsive interaction with the surface oxygen atom is produced that pushes the Ir atom away from the surface. The resulting Ir₄ configuration is very similar to **B** geometry with two contact points to the surface.

Structural data for the supported **T** isomer with up to five CO molecules agree relatively good with the measured ones. The average first-shell Ir–Ir distance increases even to 2.58 Å which is very close to the experimental values (2.62–2.73 Å). Of course, the Ir–C and longer Ir–O coordination numbers increase, but the distances remain relatively independent on the coordination. Only the Ir–Mg coordination shells are affected considerably. Since there are two Ir–Mg shells, for the pristine **T** isomer, whose average distances are very close (~ 0.3 Å

⁶This is true in the case of the gas-phase **T** isomer where it is still more favorable to have one CO dissociated and the second one in the molecular form.

Table 6.3: Calculated properties of $\text{Ir}_4(\text{CO})_2$ in **T**, **B** and **S** configurations when adsorbed on $\text{MgO}(100)$ surface. For **T** configuration the data for $n = 3, 4, 5$ are also presented. E_b refers to the binding energies of the n th CO molecule $E_b = -E(\text{Ir}_4(\text{CO})_n) + E(\text{Ir}_4(\text{CO})_{n-1}) + E(\text{CO})$ and total $\text{Ir}_4(\text{CO})_n$ cluster binding energies (in parentheses). All other quantities are the same as in Tab.5.2.

		ΔE [eV]	E_b [eV]	M [μ_B]	p_z [D]	Ir-Ir		Ir-O		Ir-Mg		Ir-C	
						N	R[Å]	N	R[Å]	N	R[Å]	N	R[Å]
$\text{Ir}_4(\text{CO})_2$	T	0.00	3.20(4.11)	1.95	-4.90	2.5	2.50	0.75	2.14	1.25	2.87	0.5	1.81
						0.5	3.34	0.5	2.99			0.5	3.46
	B	0.66	2.90(3.26)	1.62	-4.84	2.5	2.47	0.5	2.06	2.0	3.04	0.5	1.82
								0.5	3.00				
	S	0.49	2.71(3.42)	0.00	-5.18	2.0	2.38	0.5	2.03			0.5	1.79
						1.0	3.37	0.5	2.96			0.5	3.31
$\text{Ir}_4(\text{CO})_3$	T		2.81(3.54)	0.00	-5.91	2.5	2.54	0.75	2.14			1.0	1.88
						0.5	3.31	1.0	2.99			1.0	3.40
$\text{Ir}_4(\text{CO})_4$	T		2.58(3.27)	0.00	-8.09	2.5	2.58	0.75	2.14	0.5	2.78	1.25	1.86
						0.5	3.07	1.25	3.00	2.0	3.08	1.0	3.43
$\text{Ir}_4(\text{CO})_5$	T		1.62(2.35)	0.00	-7.34	2.5	2.58	0.5	2.09			1.5	1.89
						0.5	3.83	1.75	3.02				
Exp.	Ref.[118]					2.6-3.1	2.62-2.73	0.6-1.1	2.07-2.16				
								2.5-3.0	2.59-2.73				
	Ref.[119]					2.9	2.62	1.1	2.05	0.6	2.45	0.5	1.91
								0.5	3.33				

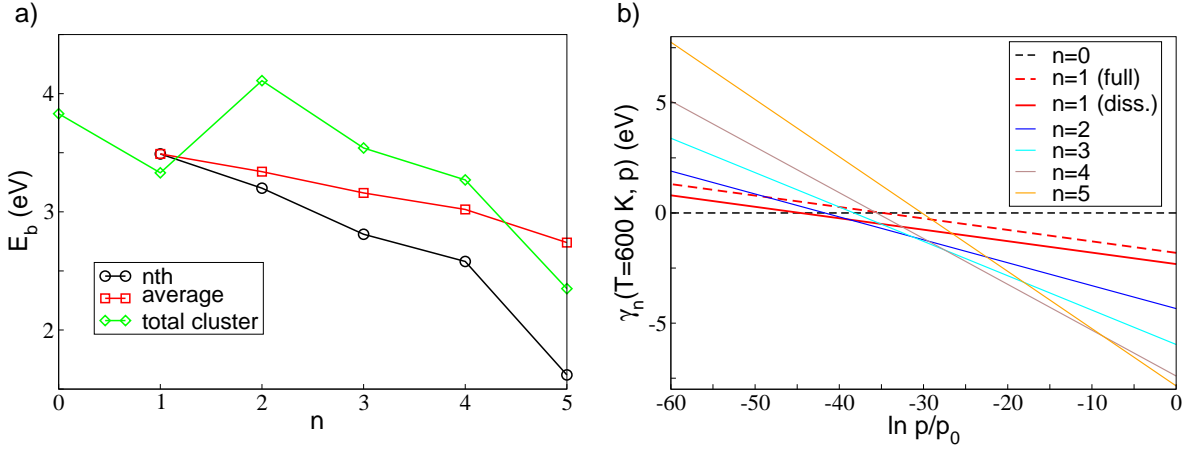


Figure 6.8: (a) Dependence of the binding energies of the n th CO molecule, average per CO molecule and the total $\text{Ir}_4(\text{CO})_n$ cluster binding energy on the number n of adsorbed CO molecules. (b) Dependence of the adsorption free energy $\gamma_n(T, p)$ on the pressure of the CO gas surrounding the MgO adsorbed Ir_4 clusters in **T** geometry at the temperature $T = 600$ K.

difference, Tab.5.2) small cluster relaxations induced by the CO adsorption, for three and five CO molecules, join these two shells making one broad Ir–Mg shell which is not presented in tables. In the cases when this does not happen the relaxations increase shorter Ir–Mg distance which gets further away from the measured values. However, whatever is the number of the CO molecules adsorbed on each of the supported Ir_4 clusters, it would produce an infrared signal in the range of the CO stretching mode⁷ which contradicts the experiments where the full decarbonylation is performed [118, 119]. Therefore, it follows from both theory and experiments that the atomic species, very likely one C adatom or coadsorbed atomic C and O, change the relative stability of the three isomers in favor of **T** structure.

From the data presented in Tab.6.2 and Tab.6.3 it is possible to estimate, using simple thermodynamical considerations, what kind of external parameters are required for the decarbonylation process to occur. Of course, this kind of analysis is restricted to the case of the thermal equilibrium. One could imagine that the MgO supported clusters are surrounded by the CO atmosphere that is described by the temperature T and pressure p . By following the route of Reuter and Scheffler [132] one can define the adsorption free energy per cluster

$$\gamma_n(T, p) = n \times [-E_b^{(n)} - \Delta\mu_{\text{CO}}(T, p)], \quad (6.1)$$

where n is the number of adsorbed CO molecules, $E_b^{(n)}$ is the average CO binding energy per molecule that depends on n (see Fig.6.8(a)) and $\Delta\mu_{\text{CO}}(T, p)$ is the chemical potential of the CO molecules in the gas-phase at temperature T and pressure p . It is important to underline that all configurational and vibrational entropy effects for the adsorbed CO molecules have been neglected⁸. The dependence of $\Delta\mu_{\text{CO}}(T, p)$ on p at different temperatures

⁷The CO stretching frequency is very robust and although the its shift is used to identify whether the CO binds as a terminal or in a bridging configuration [15], the frequency remains close to 2000 cm^{-1} and is easily detectable.

⁸The vibrational degrees of freedom could be neglected to a good approximation since the energies related to this type of motion (order of meV) are much smaller than the CO binding energies. On the other hand the CO configurational entropy is neglected due to practical reasons since it would require obtaining all possible CO

can be calculated using the chemical potential $\Delta\tilde{\mu}_{\text{CO}}(T, p^0)$ at the standard pressure ($p^0 = 1$ atm)

$$\Delta\mu_{\text{CO}}(T, p) = \Delta\tilde{\mu}_{\text{CO}}(T, p^0) + k_B T \ln \frac{p}{p^0}, \quad (6.2)$$

that on the other hand, can be calculated using the tabulated values for the CO formation enthalpy $H(T, p^0)$ at standard pressure and entropy $S(T)$ [87]

$$\Delta\tilde{\mu}_{\text{CO}}(T, p^0) = H(T, p^0) - H(T = 0, p^0) - S(T)T. \quad (6.3)$$

The value $\Delta\tilde{\mu}_{\text{CO}} = -1.17$ eV at $T = 600$ K is obtained. Temperature of 600 K is close to the experimental temperature of 300° C [118, 119].

Dependence of $\gamma_n(T, p)$ on pressure is plotted in Fig.6.8(b) for up to five CO molecules adsorbed on the MgO supported Ir_4 in **T** geometry. The $\gamma_1(T, p)$ for both dissociated CO molecule and adsorbed in the molecular form are shown. The most favorable number of adsorbed CO molecules at a given pressure is determined by the lowest γ_n value. It could have been anticipated that due to high CO binding energies it is not very favorable to desorb CO molecules. The data show that at pressures close to p_0 it is the most favorable to have five CO molecules adsorbed on the clusters⁹. The desorption starts at very low pressures about $\exp(-10)p_0$ and the full decarbonylation requires pressures which are practically zero. This indicates that in experiments the crucial are the nonequilibrium conditions under which the decarbonylation of the deposited Ir_4 is performed. Namely, it is done [118, 119] in the atmosphere of the flowing He gas which removes all the desorbed CO molecules. In these conditions at the point where there is only one CO molecule per cluster it is certainly possible also to dissociate the CO ligands.

6.3 Interaction of $\text{TiO}_2(100)$ Supported Ir_4 Clusters With a C Atom or a Single CO molecule

Interaction of $\text{TiO}_2(110)$ supported Ir_4 clusters only with a C adatom and a single CO molecule has been studied. The adsorption geometries with the lowest total energies are displayed in Fig.6.9 and the corresponding calculated data presented in Tab.6.4.

Upon adsorption of a single C adatom, the relative stability of the three isomers changes in favor of **T** structure. It becomes by 0.66 and 0.43 eV more stable than **B** and **S**, respectively. However, the binding energies of the C adsorbate and binding energies of the total Ir_4C cluster become considerably different than those for the adsorption of the C adatom to the gas-phase clusters as well as those for the adsorption of the pristine clusters to the surface. Binding of the C adatom on the $\text{TiO}_2(110)$ supported **T** and **B** isomers is as much as 0.81 and 1.00 eV weaker than in the gas-phase, respectively. Moreover, the total cluster binding energies of both structures become by 1.00 (**T**) and 1.22 (**B**) lower as well. On the other hand, binding of the C adatom to **S** structure is by 0.55 eV stronger than in the gas-phase and the binding energy of the total cluster also increases by 0.36 eV.

It has been shown in Sec.5.6 that the pristine Ir_4 clusters to a good extent keep their gas-phase geometries. Therefore, the origin of the changes in the interactions with adsorbates

adsorption configurations. However, its contribution would be of the order of $k_B T$ which at the temperatures of interest is also small comparing to the CO binding energies.

⁹Or even six! The adsorption of more than five CO molecules has not been studied yet.

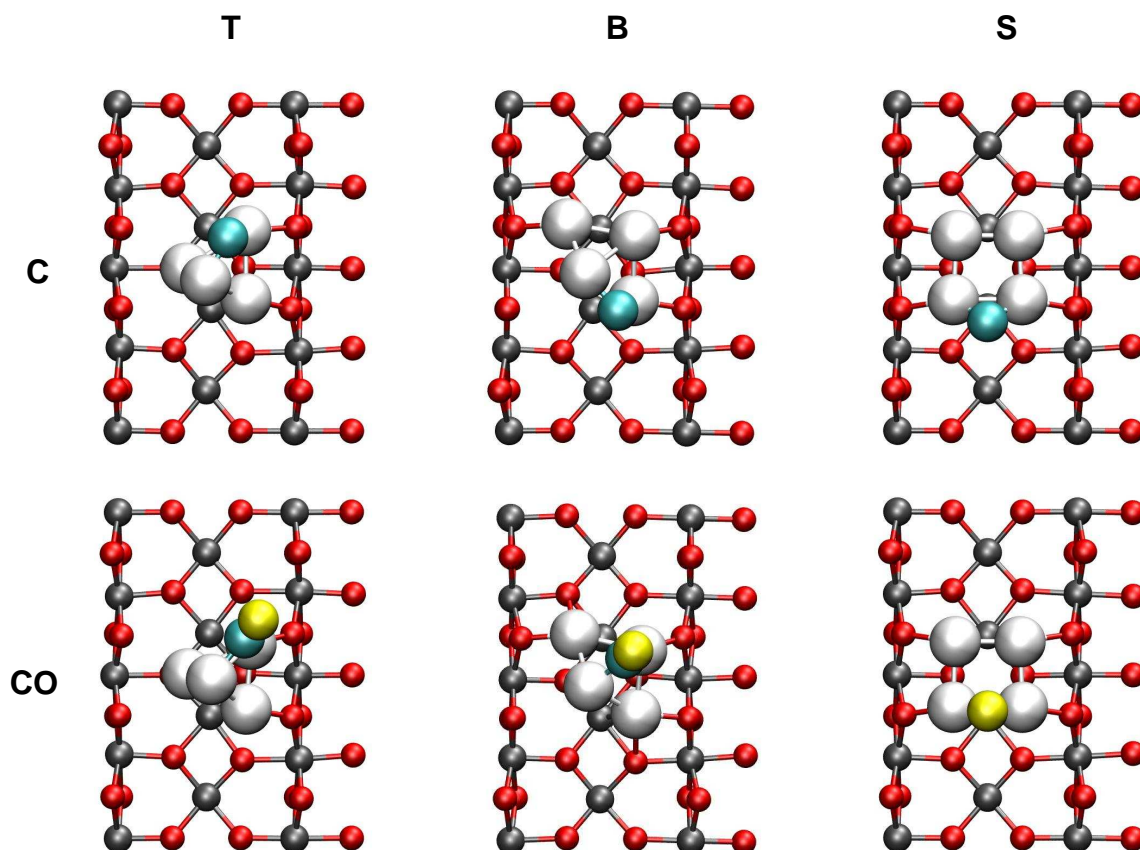


Figure 6.9: Adsorption configurations with the lowest total energies of a single C adatom and CO molecule on the three $\text{TiO}_2(110)$ supported Ir_4 isomers.

lays in the differences in their electronic structures induced by the support. It is also shown in the same section that in the vicinity of $\text{TiO}(110)$ there is a strong electrostatic field which polarizes the adsorbed clusters. The polarization affects the gas-phase relative stability of the three isomers and certainly affects their electronic structures. In fact, symmetry breaking accompanied by the surface field leads to mixing of the molecular orbitals of the three clusters which on the other hand influences their interaction with the carbon adatom.

This effect is particularly strong for **T** and **B** isomers. Carbon adatom binds in the same bridging configuration to all three structures which indicates that the bonding mechanism itself remains similar to that in the gas-phase (and on the MgO surface). However, the strongly interacting antibonding orbital of both **T** and **B** structures (see Sec.4.1) is now involved in linear combinations with other MOs of the two clusters and becomes partially filled. Moreover, the linear combinations in which this orbital participates located above the Fermi energy are shifted to higher energies. Therefore, the energy gain due to the interaction of the $\text{C-}2p$ orbitals with this MO of the two isomers (which is now broadened over the electronic spectrum) is lower than in the gas-phase. In the case of **B** structure this interaction channel is even not energetically favorable. This is the reason why the Ir–Ir bond of **B** isomer bridged by the carbon is not broken and the C binding energy approaches that of **S** structure. The Ir–Ir bond of **B** isomer bridged by the carbon atom is elongated to the distance of 2.65 Å

Table 6.4: Calculated properties of Ir₄C and Ir₄CO molecules in **T**, **B** and **S** configurations adsorbed on stoichiometric rutile TiO₂(110) surface. E_b refers to the binding energy of either C adatom or the CO molecule and the total cluster binding energy (in parentheses). All other quantities are the same as in Tab.5.6.

		ΔE [eV]	E _b [eV]	M [μ_B]	p_z [D]	Ir-Ir		Ir-O		Ir-Ti		Ir-C	
						N	R[Å]	N	R[Å]	N	R[Å]	N	R[Å]
Ir ₄ C	T	0.00	7.43(4.58)	0.00	2.21	2.5	2.51	0.75	2.04	1.0	2.67	0.5	1.82
						0.5	3.10	1.25	2.93	1.0	3.27	0.5	2.78
	B	0.66	7.00(3.56)	0.00	0.84	2.5	2.53	0.75	2.06	0.5	2.68	0.5	1.82
						0.5	3.70	0.75	2.47				
	S	0.43	6.97(4.46)	0.00	0.47	2.0	2.36	1.0	2.20	1.0	2.69	0.5	1.96
						1.0	3.34	2.0	2.96	1.0	3.35		
Ir ₄ CO	T	0.00	2.36(4.77)	0.00	1.19	3.0	2.53	0.75	2.00	0.5	2.60	0.5	1.94
								2.0	2.95	0.5	2.93	0.5	3.38
	B	0.11	2.49(3.70)	0.00		2.5	2.50	1.25	2.15	0.5	2.50	0.5	1.96
						0.5	3.69						
	S	-0.28	2.60(4.01)	0.00	-0.22	2.0	2.42	1.0	2.09	1.0	2.63	0.5	1.96
						1.0	3.42	2.5	2.89	1.0	3.30	0.5	3.18
Exp.	Ref.[126]					3.3	2.68	0.9	2.05	0.7	2.75		
								1.2	3.21				

which is much less than for the C adsorption in the gas-phase (3.19 Å). The C adsorption on **T** structure does induce breaking of the bridged Ir–Ir bond (3.10 Å), but the energy gain due to the interaction is considerably lower than in the gas-phase.

Binding energy of the C adatom to **S** increases compared to the gas-phase value. The reason for this lays mainly in the energy cost for hybridization of the MOs of the cluster. Namely, it has been discussed in Sec.4.1 that the MOs of **S** structure, that interact strongly with the C-2*p* states, are formed by the hybridization of the several both empty and filled MOs of the pristine cluster. At variance to the gas-phase, on the TiO₂ surface the modifications of the cluster's electronic structure induced by the support in fact, facilitate the C binding since the necessary hybridization requires less energy (it is already there).

The total cluster binding energies are also affected by the adsorption of carbon. The decrease in their values for **T** and **B** isomers is mainly due to the much weaker interaction between the bridged Ir atoms and the surface oxygen. In the case of **T** structure the interaction is with one of the bridging O atoms, while for **B** isomer it is with one basal surface O atom¹⁰ (see Fig.5.12). Somewhat bigger total cluster binding energy of **S** isomer with the C adatom than for the pristine cluster mostly come from different surface relaxations. Chemical bonding of the cluster with the bridging O atoms is not affected since the orbitals involved in the C adsorption are oriented orthogonal to the Ir–O(br.) bonds. Different surface relaxations are due to different "polarizability" of the Ir₄C cluster¹¹. Less charge is accumulated in the interfacial region which induces smaller displacements of both Ti(5c) and O(ba) atoms located below the cluster. The differences in the response to the surface field of **B** and **S** isomers upon C adsorption are reflected in the smaller values of the induced dipole moment than for the pristine clusters.

When compared with experimental results (Tab.5.6) the calculated structural data for the three isomers with the C adatom do not agree as well as the structural parameters of the pristine clusters. Although the Ir–Ir distances of the most stable **T** geometry increase upon the C adsorption the average first shell Ir–Ir coordination number decreases from 3.0 for the pristine cluster (Tab.5.6) to 2.5. As already discussed for the pristine clusters (Sec.5.6) the experiments are performed using the TiO₂ powders with the bigger fraction of the anatase phase and therefore, direct comparisons of the other coordination shells is not appropriate thing to do.

The most stable adsorption geometries of a single CO molecule on the three TiO₂ supported Ir₄ isomers are also displayed in Fig.6.9 and their properties presented in Tab.6.4. On the TiO₂ surface none of the three isomers favors the CO dissociation. The molecular CO adsorption is by 1.11, 1.17 and 1.16 eV more favorable than the dissociative adsorption on **T**, **B** and **S** structure, respectively. Moreover, the most stable Ir₄CO structure is **S** that is by 0.28 and 0.39 eV lower in energy than the other two (**T** and **B**, respectively). This is due to considerably lower CO binding energies on both **T** and **B** isomers than in the gas-phase. These changes as well as the changes in the CO adsorption configurations are due to changes in the electronic structures of the three isomers that are already discussed. Namely, to all three structures the CO molecule binds in a bridging not terminal configurations. However, the adsorption of a single CO molecule does not favor the CO dissociation as found for **T**

¹⁰Notice the lower first shell Ir–O coordination for **B** isomer (Tab.6.4) than for the adsorbed pristine cluster (Tab.5.6)

¹¹Strictly speaking the polarizability is defined as the linear response to the applied field. Here, I use this term to describe the response (not necessarily linear) of the three clusters to the surface electrostatic field which is too strong for any linear response treatment of the properties of the three isomers.

structure on MgO(100) and the C adatoms are not likely to be present on any of the three structures.

6.4 Influence of the Environment on the Properties of Ir₄ Clusters

After properties of Ir₄ clusters are being examined in three different environments, the gas-phase and supported by two different substrates MgO(100) and TiO₂(110), it is possible to conclude that the influence of the support is two-fold. Firstly, if the properties of the

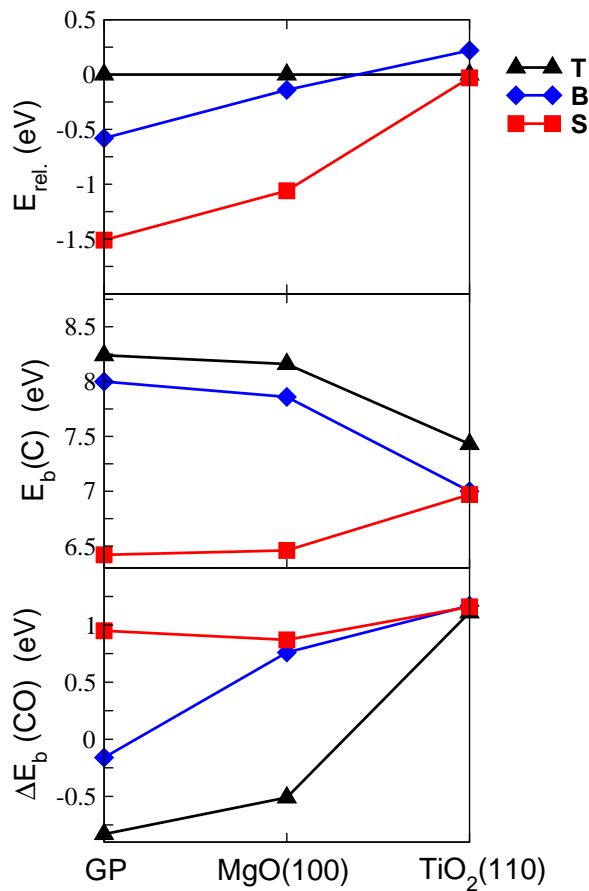


Figure 6.10: Dependence of the properties of the three Ir₄ isomers (**T**, **B** and **S**) on the environment (GP refers to the gas-phase). Their energies relative to **T** configuration $E_{rel.}$, the binding energies of the C adatom $E_b(C)$ and the difference of the CO binding energies for the dissociative and molecular CO adsorption $\Delta E_b(CO)$ (negative values mean that the dissociative adsorption is more favorable).

certain cluster geometry are followed, depending on the surface the electronic structure of the supported cluster can be more or less affected due to the electronic interactions with the surface atoms. These modifications of the electronic structure of the adsorbates are reflected in the change of their interactions with atomic or molecular species. This can be seen in Fig.6.10. Binding energies of the C adatom as well as the preference towards the CO dissociative adsorption depend strongly on the environment. At variance to the TiO₂ surface the influence of the clean MgO substrate on the properties of the supported Ir₄ clusters is

not that strong. The binding energies of C adatoms as well as the adsorbed CO molecules on the TiO_2 supported Ir_4 clusters are considerably different than in the gas-phase and on the MgO as well. Moreover, the preference for the CO dissociation reaction accounted in the gas-phase is different for the supported Ir_4 .

The second and, what has been proved in this thesis, equally important type of influence of the support on the adsorbed species is the ability to change the relative energies of the different isomers and to influence the geometry of the clusters not only through the relaxation effects. As shown in this thesis for the defected $\text{MgO}(100)$ surface as well as for the defect-free TiO_2 surface the relative stability of different isomers can be considerably altered upon adsorption. In the gas-phase **T** isomer is as much as 1.5 eV less stable than **S** structure and normally it would be considered as irrelevant in any further investigation. However, it might become relevant depending on the chemical environment. Since the electronic structure of small clusters strongly depend on their atomic configuration this is another way how the substrate may influence electronic structure of the supported species.

Similarly to the effects of the support, the interaction with atomic or molecular species could also affect the relative energies of different isomers. It is shown in this thesis that a single C adatom (neither H nor C) changes the energy ordering of the three supported Ir_4 isomers in favor of **T** isomer bringing theoretical results in a better accordance with the experimental ones for the $\text{MgO}(100)$ supported Ir_4 . The origin of the carbon lays in the CO ligands which are present on the clusters during the preparation procedure. The CO dissociation is as favorable as the competing process CO desorption on the MgO supported **T** isomer.

Therefore, this thesis can be concluded with the statement that the properties of small transition metal clusters, Ir_4 in particular, greatly depend on the surrounding conditions. Understanding the relations between atomic and electronic structure of different isomers for a given cluster size, and their chemical environment, enables the control of their properties which is the ultimate goal for the applications.

Chapter 7

Conclusions

A theoretical study of the properties of Ir_4 clusters both in the gas-phase and when adsorbed on two commonly used oxide substrates $\text{MgO}(100)$ and $\text{TiO}_2(110)$, has been carried out. Theoretical tools based on density functional theory (DFT) within the generalized gradient approximation (GGA) and ultrasoft pseudopotentials have been used. Theoretical models are extensively tested and their applicability to studied problems verified.

Special emphasis is put on the relative stability of different Ir_4 isomers. The importance of this issue is, according to the opinion of the author of these lines, underestimated. The lowest total energy configurations are of course, the most relevant since they are most probably realized in experiments. However, which geometry will be the most stable one in a given situation depends both on the gas-phase relative stability and experimental conditions.

Properties of the gas-phase structures laying higher in energy are presented in the scientific publications mainly as a proof that the search for a global minimum is conducted carefully. Only in the cases of discrepancy with experiments (as for Ir_4) or where several nearly degenerate configurations are predicted, properties of the low energy structures are discussed in more details. It is shown in this thesis that the configurations which lay very high in energy¹ and which would normally be treated as completely irrelevant may become relevant due to the interactions with the environment.

At the beginning, gas-phase Ir_n ($n = 1, \dots, 8$) clusters have been studied. Resulting energy orderings of different isomers for a fixed n are in a relatively good accordance with other theoretical results treating gas-phase Ir clusters. However, variations in calculated relative energies between different isomers and, in some cases different ordering of the low energy structures can be found in the literature (see discussion in Chap.3). Agreement between different studies is much better when the geometries of the most stable configurations are compared.

In this thesis it is shown that the discrepancies in stability of different isomers are mainly due to different level of hybridization of atomic orbitals yielded by different theoretical models (Chap.3). The Ir_4 clusters are used for studying bonding mechanism in iridium clusters and it has been found that the relative stability of different isomers depends strongly on the level of $5d$ - $6s$ hybridization. This is also confirmed for other transition metal tetramers. The differences in published results are due to the fact that the level of hybridization is very sensitive on the approximations used in computations². However, predicted energy ordering

¹Compared to the thermal energies at room temperature (~ 25 meV).

²More precisely mostly on the exchange and correlation functional used in computations.

for the three relevant Ir₄ isomers is proved to be robust.

The gas-phase Ir₄ isomer with the lowest total energy is the square (**S**) structure that is as much as 0.93 and 1.51 eV more stable than the butterfly (**B**) and tetrahedron (**T**), respectively. This result is in contradiction with experimental findings which indicate that the oxide supported Ir₄ clusters adopt tetrahedral configuration.

Upon adsorption on the MgO(100) surface the **S** isomer remains the most stable Ir₄ structure, well separated in energy from the other two (Chap.5). Moreover, the tetrahedron is heavily distorted by the interaction with the surface oxygen. Presence of point defects (neutral and charged O vacancies) affects the energy ordering making tetrahedron and square very close in energy, but structural distortion of the tetrahedron are even bigger and the predicted data do not correspond to experiments. Diffusion of the **S** cluster on MgO(100) surface has also been studied. Two diffusion mechanisms are found the cluster "walk" and diffusion through structural transformations to **B** and **T** structures. It is estimated, based on the magnitudes of the calculated energy barriers and typical vibrational frequencies of the **S** structure, that temperatures of about 400° C could trigger the diffusion. This result agrees well with experimental findings.

On TiO₂(110) the **T** and **S** structures become degenerate and **B** becomes the least stable isomer (Chap.5). The structural distortions of the three isomers are small which is in accord with the experimental data. It is shown that the TiO₂ surface influences relative stability of the three isomers through a particularly strong electrostatic field acting on the adsorbates. This field is probably caused by a large anomaly in effective charges which is known to exist for bulk rutile TiO₂³.

In addition to the oxide substrates interactions with H, C and O atoms as well as with CO molecules have been studied (Chap.4 and Chap.6). In all environments adsorption of a single C atom strongly influences the stability of the three isomers. Upon C adsorption, **B** becomes the most stable gas-phase isomer while on both MgO(100) and TiO₂(110) surfaces **T** is the most probable structure. Due to the big mass difference between carbon and iridium atoms, purely carbon vibrational modes appear in the spectra. Calculated carbon frequencies on **T** structure in the gas-phase (the MgO supported) are 103.5 and 87.6 meV (113.2 and 87.6 meV). These characteristic carbon frequencies offer a possibility for the experimental verification of the carbon presence. Adsorption of a single H or O atom does not produce the same effect as the C adsorption regardless of the environment.

Interaction with CO molecules is also important, given the experimental procedure for producing supported Ir₄ clusters out of Ir₄(CO)₁₂ carbonyl molecules. The dissociative CO adsorption is more favorable than the molecular adsorption on the gas-phase **T** and **B** isomers. On MgO(100) the dissociative CO adsorption is energetically more favorable only on **T** structure while on TiO₂(110) molecular CO binds stronger to all three isomers. Barrier for CO dissociation on **T** cluster supported by MgO(100), although quite high (2.97 eV), indicates that this reaction is as probable as the competing process the CO desorption (requiring 2.98 eV). Since the decarbonylation of Ir₄(CO)₁₂ is conducted in the nonequilibrium conditions (flowing He gas) the CO ligands could dissociate leaving carbon adatoms on Ir₄ clusters.

All these results indicate that chemical environment influences significantly both atomic and electronic structure of the supported Ir₄ clusters. Therefore, properties of the clusters

³In the bulk rutile TiO₂ the effective charges on Ti and O ions are considerably different from their formal +4 and -2 values. They lay, depending on the direction, in the range 5.20–7.70 and -1.35– -4.82 electrons, respectively [129].

cannot be treated independently on their surrounding. Knowledge of the relations between clusters and their environment is the key factor in engineering better catalysts based on oxide-supported small metallic particles.

There are also several issues that remain open. The first is related to the theoretical modeling of transition metal clusters. Although DFT is the method of choice it remains open which approximation to DFT (or which XC functional) describes the best properties of transition metals clusters. In these kind of investigations one usually faces a lack of experimental data for well characterized clusters in the gas-phase or deposited on well characterized substrates. In these cases, the results obtained with more accurate CI calculations are typically used as the benchmarks for DFT models. However, due to very high demands for computational power these results are available only for a number of systems typically very small in size (usually only for dimers).

Second, it is not yet clear what are the catalytically active, Ir_4 based species found in experiments. Again, well characterized samples are needed. This is necessary in order to be able to reach better understanding of the role of Ir_4 in chemical reactions. Without unified interpretation of the results coming both from experiments performed in controlled conditions and the theory, any theoretical modeling of processes such as chemical reactions on supported transition metal clusters remains mostly in the realm of the imagination of a theoretician.

Furthermore, none of the results, neither experimental nor theoretical, treating Ir_6 clusters have been presented here. In experiments [119] deposited Ir_6 clusters are prepared also using the $\text{Ir}_4(\text{CO})_{12}$ as a precursor. Additional chemical treatments are then used, and from the EXAFS data it may be concluded that the resulting supported species are octahedral Ir_6 . Theory predicts trigonal prism as the most stable Ir_6 structure (Chap.4). The same result is obtained for the MgO supported species. Moreover, none of the studied adsorbates affects the stability of Ir_6 isomers in the same way like for Ir_4 .

Finally, the issue of the electrostatic field of the $\text{TiO}_2(110)$ surface needs to be further investigated as well as its influence on adsorbates. While it can be assumed that this field originates from the large anomaly in effective charges of bulk rutile TiO_2 there are no indications in the literature what are the effective charges of atoms at the surface.

Appendix A

Extended X-Ray Absorption Fine Structure (EXAFS) Spectroscopy

Extended X-Ray absorption fine structure (EXAFS) refers to the oscillatory behavior of the X-ray absorption as a function of photon energy beyond an absorption edge. This definition of EXAFS, taken from reference [133] describes the best what is EXAFS. The fine structure in the absorption coefficient μ is shown in Fig.A.1. It typically displays oscillatory behavior as a function of the incident photon energy. This effect is absent for an isolated atom and depends exclusively on the chemical environment, in particular on the number and type of neighbors as well as interatomic distances. This effect is widely used as an experimental tool for studying atomic structure of various systems (solids, molecules, liquids,...). The EXAFS spectroscopy is a very sophisticated tool and its development is greatly due to the availability of the synchrotron radiation which improved substantially the quality of EXAFS data. It is nowadays established as a powerful technique for structural studies. EXAFS is very useful for systems where single crystal X-ray diffraction is not applicable.

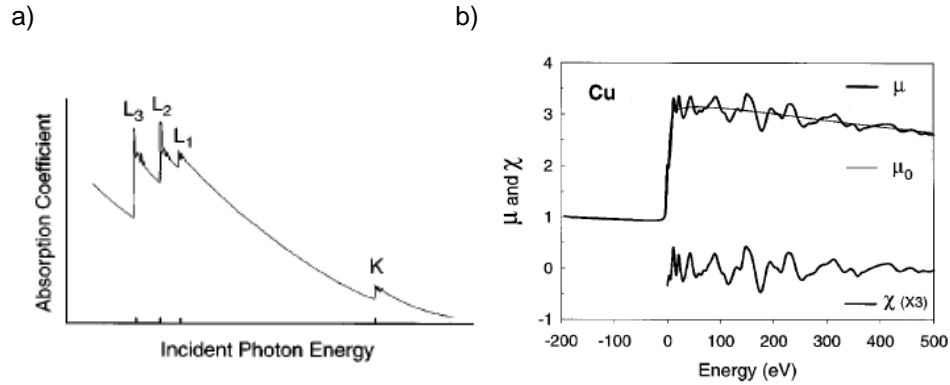


Figure A.1: (a) Schematic figure of a typical X-ray absorption spectrum. (b) EXAFS above the Cu K-edge. Both absorption coefficient μ and normalized oscillatory part χ (Eq.A.2) are shown. The values of χ are multiplied by 3. Both figures (a) and (b) are taken from Ref.[134].

The fine structure in the X-ray absorption spectra may extend up to 1000 eV above the edge and may have an amplitude in range of 1–20 % of the edge jump [133]. The explanation for this effect lays in the interference of the outgoing photoelectron wave with

the wave backscattered from the neighbouring atoms. In fact, if the absorbing atom has a neighbouring atom the outgoing photoelectron wave will be backscattered by the neighbouring atom. The final state is then the sum of the outgoing and all the backscattered waves from each neighbouring atom.

For an isolated atom a photoelectron emitted due to the X-ray absorption will travel as a spherical wave with the wave vector

$$k = \sqrt{\frac{2m}{\hbar^2}(E - E_0)}, \quad (\text{A.1})$$

where E is the photon energy and E_0 is the absorption edge energy. The EXAFS is usually described in terms of oscillatory part χ of the absorption coefficient μ normalized to the averaged absorption μ_0

$$\chi(E) = \frac{\mu(E) - \mu_0(E)}{\mu_0(E)}. \quad (\text{A.2})$$

Standard way is to express χ as a function of the wave vector using Eq.A.1 and to write it as a sum

$$\chi = \sum_j N_j S_j(k) F_j(k) e^{-2\sigma_j^2 k^2} e^{-2r_j/\lambda_j(k)} \frac{\sin(2kr_j + \phi_{ij}(k))}{kr_j^2}, \quad (\text{A.3})$$

where N_j is the number of neighboring atoms of the j th type at the distance r_j with the backscattering amplitude $F_j(k)$. Thermal and static disorders are described by the Debye-Waller factor σ_j , while the term $e^{-2r_j/\lambda_j(k)}$ is due to inelastic losses in the scattering process with the mean free path λ_j . $S_i(k)$ is the amplitude reduction factor due to many-body effects at the central atom and $\phi_{ij}(k)$ is the total phase shift experienced by the photoelectron which depends on both absorber and the backscatterer. Since $\phi_{ij}(k)$ depends on k it also influences the frequency of the sinusoidal function.

In practice the results of EXAFS spectroscopy depend on the feasibility of resolving the measured spectra into individual waves that correspond to different type of neighbors of the absorbing atom. This is typically done by two methods, curve-fitting or Fourier transform technique. The first method is based on a best fitting of the data with a modeled sum of individual waves. The other method uses Fourier transformation of the data into a real space where the k -space wave behavior is localized into separated peaks. Positions of those peaks contain the information about the distances between the absorber and the neighbors while the sizes of the peaks are related to the numbers of and types of the neighboring atoms.

Appendix B

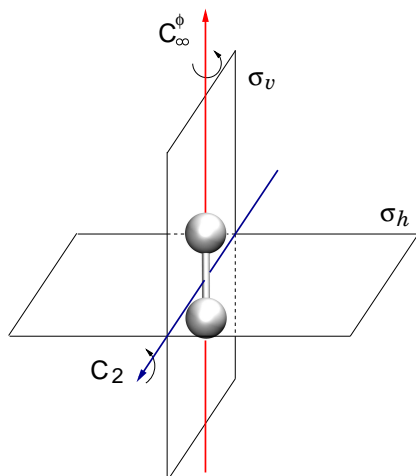
Character Tables of $D_{\infty h}$, C_{2v} , D_{4h} and T_d Point Groups

Character tables of $D_{\infty h}$, C_{2v} , D_{4h} and T_d groups which are important for this study are presented here. Labeling of their irreducible representations is done according to Ref.[135]. Each table is preceded by a figure where the group transformations are presented pictorially on a ball and stick models representing Ir_4 clusters.

In addition to the characters of the irreducible representations the characters of the representations in the subspaces that are spanned over the atomic orbitals are shown. These representations are formed by grouping the atomic orbitals sitting on each atom in the irreducible representations of the small group¹ of a given atom. Orbitals belonging to the same irreducible representations of the small groups of equivalent atoms are also equivalent and form an invariant (but reducible) subspace. When these subspaces are reduced their basis vectors form the symmetry adapted basis set which is convenient for expanding molecular orbitals. Furthermore, it provides a natural way for the analysis of possible hybridizations. Reduction of these invariant subspaces to the irreducible representations of the corresponding group is also presented next to characters of the corresponding (reducible) representations.

In each figure a coordinate frame is assumed. Since all groups except T_d are axial groups the principal axis is always set to be the z -axis while x and y lay in the mirror planes. The atomic orbitals of a tetrahedron are labeled according to the local coordinate frames. Each atom has its own frame with the z axis pointing from the atom to the center of the tetrahedron. The x and y are chosen in such a way to be connected with other local x and y by a group transformations that connect the corresponding atoms.

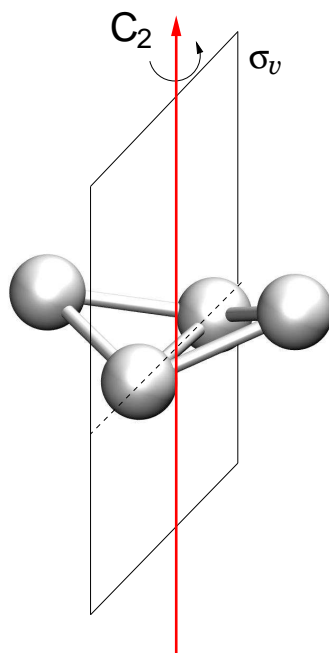
¹The subgroup of the symmetry group that leaves the given atom invariant.



$D_{\infty h}$	E	$2C_{\infty}^{\phi}$	$C_{\infty}^{\phi} \sigma_v$	i	$2S_{\infty}^{\phi}$	$C_{\infty}^{\phi} C_2$	
A_{1g}	1	1	1	1	1	1	
A_{2g}	1	1	-1	1	1	-1	
$E_{mg} (m=1,2,\dots)$	2	$2\cos(m\phi)$	0	2	$2(-1)^m \cos(m\phi)$	0	
A_{1u}	1	1	1	-1	-1	-1	
A_{2u}	1	1	-1	-1	-1	1	
$E_{mu} (m=1,2,\dots)$	2	$2\cos(m\phi)$	0	-2	$-2(-1)^m \cos(m\phi)$	0	
s	2	2	2	0	0	0	$\Rightarrow A_{1g} + A_{1u}$
d_{z^2}	2	2	2	0	0	0	$\Rightarrow A_{1g} + A_{1u}$
$d_{x^2-y^2}, d_{xy}$	4	$4\cos(2\phi)$	0	0	0	0	$\Rightarrow E_{2u} + E_{2g}$
d_{xz}, d_{yz}	4	$4\cos(\phi)$	0	0	0	0	$\Rightarrow E_{1u} + E_{1g}$
p_z	2	2	2	0	0	0	$\Rightarrow A_{1g} + A_{1u}$
p_x, p_y	4	$4\cos(\phi)$	0	0	0	0	$\Rightarrow E_{1u} + E_{1g}$

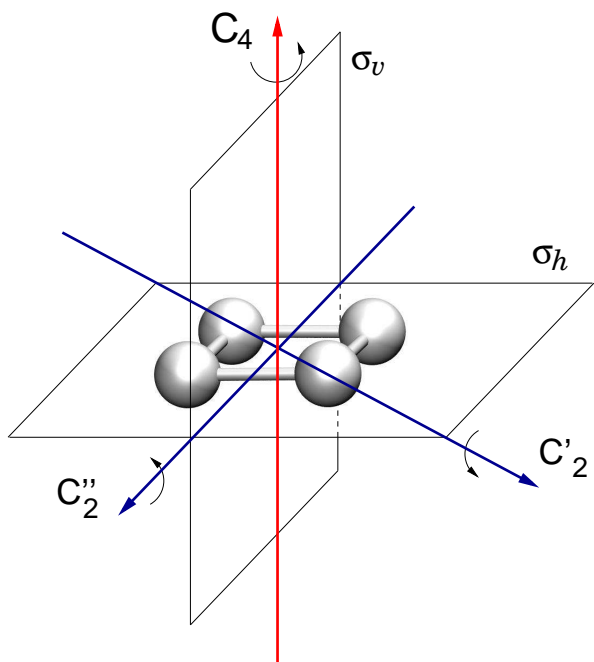
Upon reducing symmetry from $D_{\infty h}$ to D_{4h} :

$$\begin{aligned}
 A_{1g} &\Rightarrow A_{1g} \\
 A_{1u} &\Rightarrow A_{2u} \\
 E_{1g} &\Rightarrow E_g \\
 E_{1u} &\Rightarrow E_u \\
 E_{2g} &\Rightarrow B_{1g} + B_{2g} \\
 E_{2u} &\Rightarrow B_{1u} + B_{2u}
 \end{aligned}$$

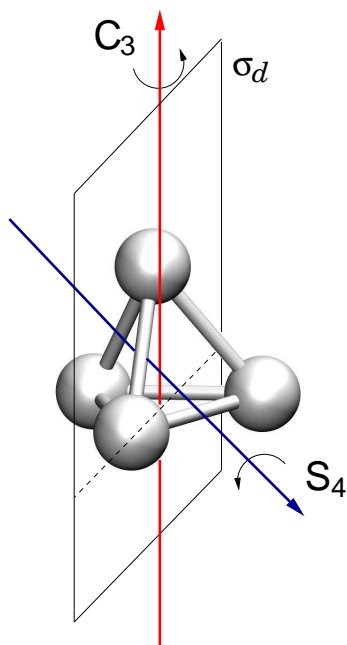


Superscripts 1 and 2 of the symbols of atomic orbitals refer to the two types of nonequivalent (by symmetry) atoms in the butterfly structure, the wingtip and body atoms.

C_{2v}	E	C_2	σ_v	$\sigma_{v'}$	
A_1	1	1	1	1	
B_1	1	-1	1	-1	
B_2	1	-1	-1	1	
A_2	1	1	-1	-1	
$s^{1/2}$	2	0	2/0	0/2	$\Rightarrow A_1+B_{1/2}$
$d_z^{1/2}$	2	0	2/0	0/2	$\Rightarrow A_1+B_{1/2}$
$d_{x^2-y^2}^{1/2}$	2	0	2/0	0/2	$\Rightarrow A_1+B_{1/2}$
$d_{xy}^{1/2}$	2	0	-2/0	0/-2	$\Rightarrow A_2+B_{2/1}$
$d_{xz}^{1/2}$	2	0	2/0	0/2	$\Rightarrow A_1+B_{1/2}$
$d_{yz}^{1/2}$	2	0	-2/0	0/-2	$\Rightarrow A_2+B_{2/1}$
$p_z^{1/2}$	2	0	2/0	0/2	$\Rightarrow A_1+B_{1/2}$
$p_x^{1/2}$	2	0	2/0	0/2	$\Rightarrow A_1+B_{1/2}$
$p_y^{1/2}$	2	0	-2/0	0/-2	$\Rightarrow A_2+B_{2/1}$



D_{4h}	E	$2C_4$	C_2	$2C'_2$	$2C''_2$	i	$2S_4$	σ_h	$2\sigma_v$	$2\sigma_d$	
A_{1g}	1	1	1	1	1	1	1	1	1	1	
A_{2g}	1	1	1	-1	-1	1	1	1	-1	-1	
B_{1g}	1	-1	1	1	-1	1	-1	1	1	-1	
B_{2g}	1	-1	1	-1	1	1	-1	1	-1	1	
E_g	2	0	-2	0	0	2	0	-2	0	0	
A_{1u}	1	1	1	1	1	-1	-1	-1	-1	-1	
A_{2u}	1	1	1	-1	-1	-1	-1	-1	1	1	
B_{1u}	1	-1	1	1	-1	-1	1	-1	-1	1	
B_{2u}	1	-1	1	-1	1	-1	1	-1	1	-1	
E_u	2	0	-2	0	0	-2	0	2	0	0	
s	4	0	0	2	0	0	0	4	2	0	$\Rightarrow A_{1g}+B_{1g}+E_u$
d_{z^2}	4	0	0	2	0	0	0	4	2	0	$\Rightarrow A_{1g}+B_{1g}+E_u$
d_{xy}	4	0	0	2	0	0	0	4	2	0	$\Rightarrow A_{1g}+B_{1g}+E_u$
$d_{x^2-y^2}$	4	0	0	-2	0	0	0	4	-2	0	$\Rightarrow A_{2g}+B_{2g}+E_u$
d_{xz}, d_{yz}	8	0	0	0	0	0	0	-8	0	0	$\Rightarrow A_{1u}+A_{2u}+B_{1u}+$ $+B_{2u}+E_g$
p_z	4	0	0	2	0	0	0	4	2	0	$\Rightarrow A_{1g}+B_{1g}+E_u$
p_x, p_y	8	0	0	0	0	0	0	8	0	0	$\Rightarrow A_{1g}+A_{2g}+B_{1g}+$ $+B_{2g}+E_u$



T_d	E	$8C_3$	$3C_2$	$6S_4$	$6\sigma_d$	
A_1	1	1	1	1	1	
A_2	1	1	1	-1	-1	
E	2	-1	2	0	0	
T_1	3	0	-1	1	-1	
T_2	3	0	-1	-1	1	
s	4	1	0	0	2	$\Rightarrow A_1 + T_2$
d_{z^2}	4	1	0	0	2	$\Rightarrow A_1 + T_2$
$d_{xy}, d_{x^2-y^2}$	8	-1	0	0	0	$\Rightarrow E + T_1 + T_2$
d_{xz}, d_{yz}	8	-1	0	0	0	$\Rightarrow E + T_1 + T_2$
p_z	4	1	0	0	2	$\Rightarrow A_1 + T_2$
p_x, p_y	8	-1	0	0	0	$\Rightarrow E + T_1 + T_2$

Bibliography

- [1] D. M. P. Mingos and D. J. Wales, *Introduction to Cluster Chemistry*, Prentice-Hall, Englewood Cliffs, New Jersey, 1990.
- [2] R. E. Leuchtner, A. C. Harms, and A. W. Castleman Jr., J. Chem. Phys. **91**, 2753 (1989).
- [3] A. W. Castleman Jr., and S. N. Khanna, J. Phys. Chem. C **113**, 2664 (2009).
- [4] B. Hvolbaek, T. V. W. Janssens, B. S. Clausen, H. Falsig, C. H. Christensen, and J. K. Nørskov, Nano Today **2**, no. 4, 14 (2007).
- [5] <http://www.webelements.com/>
- [6] <http://www.taxfreegold.co.uk/preciousmetalpricesindx.html>
- [7] D. C. Seets, M. C. Wheeler, and C. B. Mullins, Chem. Phys. Lett. **266**, 431 (1997).
- [8] D. F. Johnson, and W. H. Weinberg, Science, **261**, 76 (1993).
- [9] J. H. Jones, Platinum Metals Rev. **44**, 94 (2000).
- [10] M. Aizawa, S. Lee, and S. Anderson, Surf. Sci. **542**, 253 (2003).
- [11] A. Berkó, F. Solymosi, Surf. Sci. **411**, L900 (1998).
- [12] A. M. Argo, J. F. Odzak, F. S. Lai, and B. C. Gates, Nature **415**, 623 (2002).
- [13] B. Huber, P. Koskinen, H. Häkkinen, and M. Moseler, Nature Materials **5**, 44 (2006).
- [14] R. H. Crabtree, *The Organometallic Chemistry of the Transition Metals*, 4th edition, Wiley-Interscience, New Jersey, 2005.
- [15] P. J. Dyson, and J. S. McIndoe, *Transition Metal Carbonyl Cluster Chemistry*, Gordon and Breach Science Publishers, Amsterdam 2000.
- [16] M. R. Churchill, and J. P. Hutchinson, Inorganic Chemistry **17**, 3528 (1978).
- [17] P. Hohenberg, and W. Kohn, Phys. Rev. **136**, B864 (1964).
- [18] W. Kohn, Rev. Mod. Phys **71**, 1253 (1998).
- [19] R. M. Martin, *Electronic structure, basic theory and practical methods*, Cambridge university press, Cambridge (2004).
- [20] W. Kohn, and L. J. Sham, Phys. Rev. **140**, A1133 (1965).

- [21] J. P. Perdew, J. A. Chevary, S. H. Vosko, K. A. Jackson, M. R. Pederson, D. J. Singh, and C. Fiolhais, Phys. Rev. B **46**, 6671 (1992).
- [22] J. P. Perdew, K. Burke, and M. Ernzerhof, Physical Review Letters **77**, 3865 (1996).
- [23] A. D. Becke, Phys. Rev. A **38**, 3098 (1988).
- [24] C. Lee, W. Yang, and R. G. Parr, Phys. Rev. B **37**, 785 (1988).
- [25] J. P. Perdew, M. Ernzerhof, and K. Burke, J. Chem. Phys. **105**, 9982 (1996).
- [26] J. Hafner, J. Comput. Chem. **29**, 2044 (2008).
- [27] N. W. Ashcroft, and N. D. Mermin, *Solid State Physics*, Holt–Saunders, Philadelphia (1976).
- [28] A. Baldereschi, Phys. Rev. B **7**, 5212 (1973).
- [29] D. J. Chadi, and M. L. Cohen, Phys. Rev. B **8**, 5747 (1973).
- [30] H. J. Monkhorst, and J. D. Pack, Phys. Rev. B **13**, 5188 (1976).
- [31] M. C. Payne, M. P. Teter, D. C. Allan, T. A. Arias, and J. D. Joannopoulos, Rev. Mod. Phys. **64**, 1045 (1992).
- [32] P. P. Ewald, Ann. Phys. (Leipzig) **64**, 253 (1921).
- [33] M. T. Yin, and M. L. Cohen, Phys. Rev. B **26**, 5668 (1982).
- [34] B. Hammer, L. B. Hansen, and J. K. Nørskov, Phys. Rev. B **59**, 7413 (1999); S. R. Bahn and K. W. Jacobsen, Comput. Sci. Eng. **4**, 56 (2002).
- [35] QUANTUM-ESPRESSO is a community project for high-quality quantum-simulation software, based on density-functional theory, and coordinated by Paolo Giannozzi. See <http://www.quantum-espresso.org>
- [36] J. Neugebauer, and M. Scheffler, Phys. Rev. B **46**, 16067 (1992).
- [37] M. Born, and J. R. Oppenheimer, Ann. Phys. (Leipzig) **84**, 457 (1927).
- [38] S. Baroni, S. de Gironcoli, A. Dal Corso, and P. Gianozzi, Rev. Mod. Phys. **73**, 515 (2001).
- [39] K. J. Laidler, and M. C. King, J. Phys. Chem **87**, 2657 (1983).
- [40] H. Jónsson, G. Mills, and K. W. Jacobsen, in *Classical and Quantum Dynamics in Condensed Phase Simulations*, edited by B. J. Berne, G. Ciccoli, and D. F. Coker, World Scientific, Singapore (1998).
- [41] G. Henkelman, B. P. Uberuaga, and H. Jónsson, J. Chem. Phys. **113**, 9901 (2000).
- [42] S. G. Louie, S. Froyen, and M. L. Cohen, Phys. Rev. B **26**, 1738 (1982).
- [43] L. Kleinman, and D. M. Bylander, Phys. Rev. Lett. **48**, 1425 (1982).

- [44] D. Vanderbilt, Phys. Rev. B **41**, 7892 (1990).
- [45] K. Laasonen, A. Pasquarello, R. Car, C. Lee, and D. Vanderbilt, Phys. Rev. B **47**, 10142 (1992).
- [46] N. Troullier, and J. L. Martin, Phys. Rev. B **43**, 1993 (1991).
- [47] <http://www.fhi-berlin.mpg.de/th/fhi98md/fhi98PP/>
- [48] <http://www.physics.rutgers.edu/dhv/uspp/>
- [49] C.-L. Fu, and K.-M. Ho, Phys. Rev. B **28**, 5480 (1983).
- [50] H. Sa'adi, and B. Hamad, J. Phys. Chem. Sol. **69**, 2457 (2008).
- [51] S. Grussendorf, N. Chetty, and H. Dreyse, J. Phys.:Condens. Matter **15**, 4127 (2003).
- [52] Y. Cerenius, and L. Dubrovinsky, J. Alloys Compounds **306**, 26 (2000).
- [53] C. Kittel, *Introduction to Solid State Physics* 6th edn, Wiley, New York (1986).
- [54] J. A. Alonso, Chem. Rev. **100**, 637 (2000).
- [55] Per-Olov Löwdin, J. Chem. Phys. **18**, 365 (1950).
- [56] M. D. Morse, Chem. Rev. **86**, 1049-1109 (1988).
- [57] J. R. Lombardi, and B. Davis, Chem. Rev. **86**, 1049-1109 (1988).
- [58] A. R. Miadema, K. A. J. Gingerich, J. Phys. B: At. Mol. Phys. **12**, 2081 (1979).
- [59] Z. J. Wu, Chem. Phys. Lett. **383**, 251 (2004).
- [60] Z. J. Wu, B. Han, Z. W. Dai, and P. C. Jin, Chem. Phys. Lett. **403**, 367 (2005).
- [61] J. Du, X. Sun, and H. Wang, Int. J. Quantum Chem. **108**, 1505 (2008).
- [62] S. Castillo, V. Bertin, E. Solano-Reyes, H. Luna-García, A. Cruz, and E. Poulain, Int. J. Quantum Chem. **70**, 1029 (1998).
- [63] D. Dai, M. Z. Liao, and K. Balasubramanian, Chem. Phys. Lett. **249**, 141 (1996).
- [64] T. Pawluk, Y. Hirata, and L. Wang, J. Phys. Chem. B **109**, 20817 (2005).
- [65] W. Zhang, L. Xiao, Y. Hirata, T. Pawluk, and L. Wang, Chem. Phys. Lett. **383**, 67 (2004).
- [66] J.-N. Feng, X.-R. Huang, and Z.-S. Li, Chem. Phys. Lett. **276**, 334 (1997).
- [67] A. Szabo, and N. S. Ostlund, *Modern Quantum Chemistry*, Mineola, New York: Dover Publishing (1996).
- [68] E. A. Ivanova Shor, V. A. Nasluzov, A. M. Shor, G. N. Vayssilov, and N. Röscg, J. Phys. Chem. C **111**, 12340 (2007).
- [69] V. Stevanović, Ž. Šljivančanin, and A. Baldereschi, Phys. Rev. Lett. **99**, 165501 (2007).

- [70] V. Stevanović, Ž. Šljivančanin, and A. Baldereschi, *Role of adsorbed H, C, O and CO on the Atomic Structure of Free and MgO(100) Supported Ir₄ Clusters*, submitted.
- [71] C. Bussai, S. Krüger, G. N. Vayssilov, and N. Rösch, *Phys. Chem. Chem. Phys.* **7**, 2656 (2005).
- [72] S. Krüger, C. Bussai, A. Genest, and N. Rösch, *Phys. Chem. Chem. Phys.* **8**, 3391 (2006).
- [73] E. A. Ivanova Shor, V. A. Nasluzov, A. M. Shor, G. N. Vayssilov, and N. Rösch, *J. Phys. Chem. C* **111**, 12340 (2007).
- [74] R. F. W. Bader, *Atoms in Molecules - A Quantum Theory*, Oxford University Press, Oxford, 1990.
- [75] *Phys. Rev. B* **51**, 4014 (1994).
- [76] H. Grönbeck, and W. Andreoni, *Chem. Phys.* **262**, 1 (2000).
- [77] A. Fortunelli, *J. Mol. Struct: Theochem* **493**, 233 (1999).
- [78] W. Zhang, Q. Ge, and L. Wang, *J. Chem. Phys.* **118**, 5793 (2003).
- [79] G. Qiu, M. Wang, G. Wang, X. Diao, D. Zhao, Z. Du, and Y. Li, *J. Mol. Struct: Theochem* **861**, 131 (2008).
- [80] D. S. Mainardi, and P. B. Balbuena, *J. Phys. Chem. A* **107**, 10370 (2003).
- [81] L. Wang, and Q. Ge, *Chem. Phys. Lett.* **366**, 368 (2002).
- [82] W. Zhang, H. Zhao, and L. Wang, *J. Phys. Chem. B* **108**, 2140 (2004).
- [83] L.-L. Wang, and D. D. Johnson, *J. Phys. Chem. B* **109**, 23113 (2005).
- [84] C. Jamorski, A. Martinez, M. Castro, and D. R. Salahub, *Phys. Rev. B* **55**, 10905 (1997).
- [85] A. Sebetci, *Chem. Phys.* **354**, 196 (2008).
- [86] W. P. Krekelberg, J. Greeley, and M. Mavrikakis, *J. Phys. Chem. B* **108**, 987 (2004).
- [87] M. W. Chase, *NIST-JANAF Thermochemical Tables*, 4th. ed., American Chemical Society, Washington DC, 1998, Monograph 9.
- [88] <http://www.physics.nist.gov/PhysRefData/MolSpec/Diatomic/Html/Tables/CO.html>
- [89] G. Blyholder, *J. Phys. Chem* **68**, 2772 (1964).
- [90] B. Hammer, Y. Morikawa, and J. K. Norskov, *Phys. Rev. Lett* **76**, 2141 (1995).
- [91] T. C. Bromfield, D. C. Ferré, and J. W. Niemantsverdriet, *Chem. Phys. Chem.* **6**, 254 (2005).
- [92] M. Mavrikakis, M. Bäumer, H.-J. Freund, and J. K. Norskov, *Catal. Lett.* **81**, 153 (2002).
- [93] X.-Q. Gong, R. Raval, and P. Hu, *Surf. Sci.* **562**, 247 (2004).

- [94] D. D. Koelling, and B. N. Harmon, J. Phys. C: Solid State Phys. **10**, 3107 (1977).
- [95] Z. P. Chang, and G. R. Barsch, J. Geophys. Res. **74**, 3291 (1969).
- [96] Z. P. Chang, and E. K. Graham, J. Phys. Chem. Sol. **38**, 1355 (1977).
- [97] A. S. Rao, and R. T. Keamey, Phys. Stat. Sol. **95**, 243 (1979).
- [98] U. Schönberger, and F. Aryasetiawan, Phys. Rev. B **52**, 8788 (1995).
- [99] P. Broqvist, H. Grönbeck, and I. Panas, Surf. Sci. **554**, 262 (2004).
- [100] N. V. Skorodumova, K. Hermansson, and B. Johansson, Phys. Rev. B **72**, 125414 (2005).
- [101] M. Stengel, *First-Principles Molecular Study of Metal-Supported Nanosystems*, doctoral thesis, EPFL, Lausanne (2004).
- [102] A. M. Ferrari, and G. Pacchioni, J. Phys. Chem. **99**, 17010 (1995).
- [103] L. M. Molina , and B. Hammer, J. Chem. Phys. **123**, 161104 (2005)
- [104] J. K. Burdett, T. Hughbanks, G. J. Miller, J. W. Richardson Jr., and J. V. Smith, J. Am. Chem. Soc. **109**, 3639 (1987).
- [105] L. Gerward, and J. S. Olsen, J. Appl. Crystallogr. **30**, 259 (1997).
- [106] U. Diebold, Surf. Sci. Rep. **48**, 53 (2003).
- [107] S.-D. Mo, and W. Y. Ching, Phys. Rev. B **51**, 13023 (1995).
- [108] C. Di Valentin, G. Pacchioni, and A. Selloni, Phys. Rev. Lett **97**, 166803 (2006).
- [109] K. J. Hameeuw, G. Cantele, D. Ninno, F. Trani, and G. Iadonisi, J. Chem. Phys. **124**, 024708 (2006).
- [110] D. Vogtenhuber, R. Podloucky, A. Neckel, S. G. Steinmann, and A. J. Freeman, Phys. Rev. B **49**, 2099 (1994).
- [111] A. T. Paxton, and L. Thiên-Nga, Phys. Rev. B **57**, 1579 (1998).
- [112] Ž. Šljivančanin, and A. Pasquarello, Phys. Rev. Lett **90**, 247202 (2003).
- [113] V. Musolino, A. Seloni, and R. Car, J. Chem. Phys. **108**, 5044 (1998).
- [114] H. Grönbeck, and P. Broqvist, J. Chem. Phys. **119**, 3896 (2003).
- [115] H. Grönbeck, and P. Broqvist, J. Phys. Chem. B **107**, 12239 (2003).
- [116] Y. Wang, E. Florez, F. Mondragon, and T. N. Truong, Surf. Sci. **600**, 1703 (2006).
- [117] K. M. Neyman, C. Inntam, V. A. Nasluzov, R. Kosarev, and N. Rosch, Appl. Phys. A **78**, 823 (2004).
- [118] S. E. Deutsch, G. Mestli, H. Knzinger, and B. C. Gates, J. Phys. Chem. B **101**, 1374 (1997).

- [119] A. M. Argo, J. F. Odzak, J. F. Goellner, F. S. Lai, F.-S. Xiao, and B. C. Gates, J. Phys. Chem. B **110**, 1775 (2006).
- [120] G. Barcaro, A. Fortunelli, F. Nita, and R. Ferrando, Phys. Rev. Lett. **95**, 246103 (2005).
- [121] L. Xu, G. Henkelman, C. T. Campbell, and H. Jónsson, Phys. Rev. Lett. **95**, 146103 (2005).
- [122] C. Oshima, T. Aizawa, R. Souda, and Y. Ishizawa, Solid. State. Commun. **73**, 731 (1990).
- [123] O. S. Alexeev, Do-W. Kim, and B. C. Gates, J. Mol. Cat. A: Chemical **162**, 67 (2000).
- [124] J. C. Fierro-Gonzales, S. Kuba, Y. Hao, and B. C. Gates, J. Phys. Chem. B **110**, 13326 (2006).
- [125] K. M. Neyman, C. Inntam, A. V. Matveev, V. A. Nasluzov, and N. Rösch J. Am. Chem. Soc. **127**, 11652 2005
- [126] J. F. Goellner, J. Guzman, and B. C. Gates, J. Phys. Chem. B **106**, 1229 (2002).
- [127] L. Thiên-Nga, and A. T. Paxton, Phys. Rev. B **58**, 13233 (1998).
- [128] H. Iddir, S. Öăüt, N. D. Browning, and M. M. Disko, Phys. Rev. B **72**, 081407(R) (2005).
- [129] G. Cangiani, *Ab-initio Study of the Properties of TiO₂ Rutile and Anatase Polytypes*, doctoral thesis, EPFL, Lausanne (2002).
- [130] K. Watanabe, M. Shindo¹, K. Tada¹, and K. Kobayashi, Jpn. J. Appl. Phys. **38**, 5270-5273 (1999).
- [131] J. Sancho-Parramon, V. Janicki, J. Arbiol, H. Zorc, and F. Peiro, Appl. Phys. Lett. **92**, 163108 (2008).
- [132] K. Reuter, and M. Scheffler, Phys. Rev. B **65**, 035406 (2001).
- [133] B. K. Teo, *EXAFS: Basic Principles and Data Analysis* Springer-Verlag, Berlin, 1986.
- [134] J. J. Rehr, and R. C. Albers, Rev. Mod. Phys. **72**, 621 (2000).
- [135] Cotton, F. A. *Chemical Applications of Group Theory*, 3rd ed., Wiley, New York 1990.

Acknowledgments

Firstly, I would like to thank Prof. Alfonso Baldereschi for giving me the opportunity to work and study as a member of his group. I am very grateful for the discussions we had during the last four years. Generosity in shearing with me his broad knowledge and experience, I greatly appreciate.

Second, and as important person for my scientific life at EPFL, without whom this thesis certainly would not see the daylight is Dr. Željko Šljivančanin. I would like to thank Dr. Šljivančanin for introducing the "world" of computational solid state physics and density functional theory to me. For his patience during numerous discussions we had in the first two years of my work at EPFL.

I also thank Prof. Wanda Andreoni, Prof. Alessandro De Vita and Dr. Željko Šljivančanin for accepting to be members of the jury of this thesis.

I am very grateful to the members of the IRRMA institute for the great working atmosphere. In particular, I greatly acknowledge Dr. Peter Broqvist and Dr. Audrius Alkauskas for very helpful discussions as well as Dr. Nicola Dorsaz for his friendship and help. I am also very grateful to Mrs. Noemi Porta, secretary of the IRRMA institute, for all the support she provided in overcoming numerous difficulties a person has in a foreign country.

I also use this occasion to thank Prof. László Forró for the opportunity to collaborate with him personally, and with the members of his group. For a theoretician, collaboration with experimental physicists is a valuable experience. I also thank Prof. Davor Pavuna for his advices.

Finally, I would like to thank to the most important person in my life, my wife Jasmina for all her love and support. Without her this thesis would not exist.

Curriculum Vitae

Name and surname	Vladan Stevanović
Date of birth	October 28th, 1975
Place of birth	Bor, Serbia
Marital status	Married

- 2005–2009 Doctoral Assistant at the *Institut Romand de Recherche Numérique en Physique des Matériaux* (IRRMA), EPFL.
Supervisor: Prof. Alfonso Baldereschi
- 2007–2009 Supervision (with Prof. A. Baldereschi) of a master student Jean–René Moret during both practical work and the master project.
- 2007 Collaboration with the experimental group of Prof. Laszlo Forró at EPFL on the properties of BaVSe₃ under pressure (PRB **78**, 235111, 2008)
- 2004–2005 Collaboration, as a research assistant, with the group for mathematical physics and quantum mechanics headed by Prof. Milan Damnjanović at the Faculty of Physics, University of Belgrade (J. Phys.: Condens. Matter **18**, 1939, 2006; Phys. Stat. Sol. (b) **243**, 1750, 2006)
- 2004 Degree in theoretical physics from the Faculty of Physics, University of Belgrade, Serbia
Supervisor: Prof. Milan Damnjanović